THÈSE DE DOCTORAT
DE L'UNIVERSITÉ LILLE

LABORATOIRE DE MÉCANIQUE DE LILLE (UMR CNRS 8107)

Présentée par

Xiang Zhang

pour obtenir le grade de

DOCTEUR DE L'UNIVERSITÉ LILLE

Domaine

GÉNIE CIVIL

Sujet de la thèse

Numerical simulation of gas migration properties in highly impermeable materials

Soutenue le 04 Novembre 2016 devant le jury composé de :

D. GREGOIRE	Université de Pau et des Pays de l'Adour	*Rapporteur*
F. COLLIN	Université de Liège	*Rapporteur*
J. TALANDIER	ANDRA	*Examinateur*
A. ALEXANDRA	Université technique de Rhénanie-Westphalie	*Examinateur*
J.F. SHAO	Université de Lille	*Examinateur*
G. DUVEAU	Université de Lille	*Encadrant de thèse*
J.B. COLLIAT	Université de Lille	*Directeur de thèse*

LML-L'UNIVERSITÉ DE LILLE

Abstract

The feasibility study of long-term radioactive waste storage in COx argillite has been performed by considering various damage and failure scenarios. This study aims at the numerical investigation of gas (mainly produced by corrosion of metallic parts) migration properties through the low-permeable formation. Traditional methods, based on macroscopic approaches or homogeneous transport properties, are inappropriate to analyse this issue at the meso/microscopic scale. In this study, realistic porous space morphologies are constructed through union of excursions of Random Fields considering different experimental pore size distributions. Afterwards, purely geometric analysis of pore space is conducted by morpho-mathematical operations for the purpose of the extraction of preferential gas transport pathways and the prediction of the gas entry pressure, the gas breakthrough pressure and the following imbibition process.

Résumé

L'étude de la faisabilité du stockage des déchets radioactifs à long terme pour les argilites du Callovo-Oxfordien (COx) a été réalisée en tenant compte des différents scénarios d'endommagement et de rupture. Cette thèse porte sur l'étude numérique des propriétés de transfert de gaz (principalement produit par la corrosion des parties métalliques) à travers cette formation peu perméable. Les méthodes traditionnelles, basées sur les approches macroscopiques où les propriétés de transpert sont considérées comme homogènes, ne sont plus adaptées à l'étude des chemins préférentiels de transfert. Dans cette étude, des modèles morphologiques de l'espace poreux à l'échelle microscopique sont construits par l'union des excursions de champ aléatoire en utilisant les distributions des tailles de pore mesurées expérimentalement. Ensuite, des analyses purement géométriques sur l'espace poreux sont réalisées par les opérations morpho-mathématiques afin d'extraire les chemins préférentielles de transpert et de prédire la pression d'entrée de gaz, la pression de percée de gaz et le processus d'imbibition.

Acknowledgement

I would like firstly to express my most sincere gratitude to my main supervisor Professor Jean-Baptiste Colliat for his precious guidances, patiences, confidences and courages during three years of my research and it is a great honour for me to be one of his students.

I am deeply grateful to Mr. Gilles Duveau, my secondary supervisor, for his helps, for his support, motivation and enthusiasm throughout the duration of my research. I would like specially to thank Dr. Mahban Hosseini for her very useful advice.

Great thanks also give to my friends in Lille and my colleagues in LML for the help and support during my stay in France. I greatly value their friendship and I deeply appreciate their kindness in exchange of knowledge, skills and for all the fun we have had in the last three years.

Finally, I have to give a great appreciation to my parents for their unconditional support and encouragement during my academic career.

Table Of Contents

List Of Figures

Notations

Φ_t	Total porosity [%]	V_p	Pore volume [m^3]
V_s	Solid volume [m^3]	d	Pore diameter [m]
γ	Surface tension [N.m^{-1}]	θ	Wetting angle
M_w	Molar mass of water [Kg.mol^{-1}]	R	Perfect gas constant [J.K^{-1}.mol^{-1}]
ρ_w	Density of water [Kg.m^{-3}]	S_p	Pore surface [m^2]
RH	Relative humidity [%]	T	Temperature [K]
P_g	Applied gas pressure [Pa]	r	Pore radius [m]
$\mathcal{P}$	Gas migration pathways	r_{eff}	Effective pore radius [m]
$T_c, T^{\ominus}$	Reference temperature [K]	P_b	Gas breakthrough pressure [Pa]
P_e	Gas entry pressure [Pa]	P_{eff}	Effective stress [Pa]
P_{conf}	Confining pressure [Pa]	P_{pore}	Pore pressure [Pa]
K	Bulk modulus [MPa]	K_s	Intrinsic bulk modulus [MPa]
χ	Effective stress coefficient	e	Volumetric strain [%]
H	Effective modulus [MPa]	W/C	Water cement radio
P_s	Gas shut-off pressure [Pa]	X_g	Gas mole concentration [mol.m^{-3}]
K_{Hg}	Henry's law constant [mol.m^{-3}.Pa^{-1}]	$\Delta_{\text{soln}}H$	Enthalpy of solution [J.mol^{-1}]
C	Concentration [mol.m^{-3}]	J	Diffusion flux [mol.m^{-2}.s^{-1}]
D	Diffusion coefficient [m^2.s^{-1}]	N_a	Avogadro's number [mol^{-1}]
η	Dynamic viscosity [Pa.s]	n	Mole numbers of particle [mol]

$C(x,y)$	Covariance function	$\mu(x)$	Mean function
$f(x)$	Density function	σ^2	Variance
L_c	Correlation length [m]	E_s	Excursion set
t	Threshold of excursion	D	Hitting set
$\mathcal{L}$	Characteristic values of morphology	M_i	Binary image
E	Structuring element	$\ominus$	Erosion
$\oplus$	Dilation	$\circ$	Morphological opening
X	Mask	Y	Marker
$\delta_X(Y)$	Geodesic dilation	$R_X(Y)$	Geodesic reconstruction
V_{dr}	Drained pores	V_{dif}	Diffusion part
V_{fil}	Filling part	t_0	Starting time of filling [s]
t_f	Filling time [s]	S_i	Surface of entrance of filling part [m^2]
V_f	Filling volume [m^3]	L	Gas migration distance in samples [m]

Chapter 1

General Introduction

Low-permeable argillite is a potential candidate host rock in repository formation of radioactive waste disposal. In France, Callovo-Oxfordian argillites are in large quantities in departments of Haute-Marne and Meuse [Fouché et al., 2004]. ANDRA (French National Radioactive Waste Management Agency) built a deeply seated underground research laboratory on the site of Bure to investigate the properties of host rocks and to study the feasibility of long-lived radioactive waste storage in Cox argillite.

In order to assess the performance and safety, different damage and failure processes are proposed and investigated. Particularly, for a long period, due to ground water seepage, humid corrosion of metallic parts, coupled to radioactive waste decay and radiolysis of water may produce a significant amount of hydrogen gas [Horseman et al., 1999][Davy et al., 2009]. If the migration of generated gas is restricted, then after a long period of accumulation, increasing gas pressure may exceed the fracture threshold and damage the compacted clay rock. In [Marschall et al., 2005], gas transport through low-permeable medium principally follows four modes: advective and diffusive transport of dissolved gas in porewater which is restricted by the low hydraulic conductivity; two phase flow under the influence of capillary resistances [Bear, 2013]; Pathway dilation which corresponds to gas-driven micro-cracks and increase of pore space; Single gas flow in macroscopic fracture. For COx argillite, the micro-crack threshold is about 9 MPa and the fracture threshold is about 12 MPa [Andra, 2005]. Considering these different and complex cases, the investigation of gas transport is of high relevance in the assessment of repository performance.

The gas breakthrough pressure is defined as the gas pressure needed in order to create continuous flow paths of gas phase across the pore system [Hildenbrand et al., 2002b]. In [Andra, 2009a], principal results show a gas entry pressure less than 3 MPa without massive gas invasion using a drainage pathway scheme when a gas breakthrough pressure in a range of 4 MPa to 5 MPa was determined using an imbibition scheme. In [Davy et al., 2009], gas migrations properties have been identified for a bentonite-argillite mock-up with a bentonite plug inside an argillite host rock. Gas critical pressure which is referred to as the appearance of gas bubbles at the downstream side is defined as 3.4 MPa - 5.3 MPa. In [Duveau et al., 2011], gas breakthrough pressure is obtained as 1.26 MPa - 3 MPa by measuring gas appearance at the downstream side. However, in that study, low gas breakthrough pressure is probably related to the generation of micro-cracks during the sample preparation process. Thus the true capillary induced breakthrough pressure should be higher. In [Le et al., 2008][Lima et al., 2012][Jacops et al., 2013][Jacops et al., 2015], gas injection tests are performed with the Boom clay (with higher porosity and larger pore size range in comparison with COx argillite) and show that the gas entry pressure (stands for the breakthrough pressure in this study) is estimated about 5 MPa.

Moreover, after the breakthrough, accompanying with gas leakage, gas pressure at the generation source may decrease thus leads to a water re-imbibition process. In [Hildenbrand et al., 2002b][Hildenbrand et al., 2002a][Hildenbrand et al., 2004], this process has been described as successive close of drained pathways until gas permeability drops to zero. Some gas-filled pores may be isolated by imbibing water phase and would stay in desaturated state, resulting in a residual gas saturation. The corresponding gas pressure to the shut-off of the last interconnected pathways may be lower than breakthrough pressure.

Numerical simulation of gas movement has been proposed following different scenarios. For instance, multi-scale porous network analysis indicates that the interconnected gas pathways appear with gas pressure about 6 MPa [Xu et al., 1997] which is slightly higher than the experimental value. Besides, finite element model coupled to mechanical strains and stresses within Biot's effective stress theory under isothermal conditions has also been discussed [Gerard et al., 2008]. In some studies, a pre-existing fracture is embedded in a continuum finite element model in order to simulate the localised gas preferential pathways. A hydro-mechanical coupling between the fracture aperture, permeability and the retention properties along the fracture is included in the model [Gerard et al., 2014]. However, in view of the randomly formed pore space, homogeneous macroscopic approaches based on an uniform distribution of permeability and porosity are not capable to adequately describe the gas migration process. In other words, at the microscopic scale, the permeability of a representative element of volume can not be regarded as an average.

In this work, the first aim is to establish several realistic 3D morphological models of pore space in COx argillite with respect to the different experimental pore size distributions. The numerical implementation of excursion set theory on continuous random field provides binary field and still has a good control of geometric and topological properties. More importantly, this method is no longer restricted by defined objects thus pore structure is generated with random shapes. This idea has been applied for the pore space reconstruction of concrete [Roubin et al., 2015] or cement paste [Hosseini, 2015]. Based on the generated model, using morpho-mathematical operations (erosion, dilation, morphological opening, geodesic reconstruction), image filtering and purely geometric analysis are conducted in order to describe the gas invasion process, predict the gas entry pressure, the gas breakthrough pressure and verify whether the capillary induced breakthrough is possible in COx argillite with gas pressure lower than the fracture threshold. Moreover, the simulation of the water-imbibition process is also involved.

Chapter 2 presents a general review from literature on the gas generation sources during the long term repository. Several basic properties of COx argillite are introduced. In particular, since the interconnected pore space provides the fluid transport pathways, its geometrical and topological properties are then of high relevance for the investigation and simulation of gas migration process. The pore size distribution in COx argillite is relatively difficult to obtain due to the nanometer magnitude of pore sizes. Several indirect methods such as mercury intrusion, water adsorption and desorption and nuclear magnetic resonance are presented. The corresponding experimental pore size distribution curves are illustrated. Following this, four modes of gas migration in low permeable rock are proposed based on micro-structural conceptualization. At the end, some experimental protocols for the investigation of gas breakthrough pressure are reviewed.

In Chapter 3, the main topic concerns about the generation of porous space morphology. The excursion set on Gaussian Random Fields is capable to transform a continuous field to a binary one and then it is suitable to represent pores and matrix in porous medium. For a single excursion, pore size varies in a limited range around the correlation length. In view of this, the union of excursion is applied to enlarge the pore size range then to provide accurate morphological model of pore space. Subsequently, geometric and topological information of model are obtained by using morpho-mathematical operations.

Chapter 4 is devoted to a numerical study of the gas entry and gas breakthrough pressure in the generated models. The emphasis is put on the proposed numerical technique based on a combination of morpho-mathematical operations such as the morphological opening and the geodesic reconstruction. Considering that the creation of gas migration pathways is principally controlled by the difference between the applied gas pressure and the capillary force, the aim of this chapter is to verify if the gas breakthrough is possible in low-permeable medium at gas pressures much lower than fracture threshold. Simulation works are performed on models generated from different pore size distributions in order to draw conclusion about which model provides results in good accordance with experimental values. Ultimately, some other potential host rocks for the storage of radioactive waste such as the Opalinus clay and the Boom clay are also investigated.

In Chapter 5, the numerical investigation is extended to the water imbibition process after the gas breakthrough. The physical definition and the associated phenomena are reviewed. Then appropriate morpho-mathematical operations are applied in order to simulate the gas shut-off pressure and the residual gas saturation.

Chapter 6 is dedicated to study the gas migration mechanism with low gas pressure. Since some phenomenological observations indicate that gas leakage may happen through dissolved molecules under low pressure condition, the proposed migration scenario needs comprise a potential drainage mechanism. Following this, a basic calculation principle is suggested based on several assumptions and simplifications. Subsequently, the determined dissolved gas breakthrough time is evaluated considering different sample sizes or different temperatures.

Chapter 2

Characteristics of COx argillite

Contents

1 Introduction

Radioactive wastes, depending on their origins, could be more or less dangerous to humans, or be more or less persistent in nature. The classification of radioactive waste is based on the radioactivity period contained in the waste and the type of radiation and radioactivity levels. They are classified into four different categories: wastes with very low activity; type A: with low activity and a short radioactivity period; type B: with low or medium level, which contains a significant amount of long-lived radioactive elements, mainly produced during the reprocessing of nuclear fuels and routine operation or maintenance in reprocessing facilities and nuclear power plants [Su, 2005]; type C: exothermic, with high activity and long life, mainly comes from reprocessing of spent nuclear fuel. In France, highly active and long-lived wastes represent less than 5% of the total radioactive wastes but contains 99% of the total radioactivity and are mainly produced by nuclear power industries [Carle and Patarin, 2003].

ANDRA (French National Radioactive Waste Management Agency) has been charged to design repository for radioactive waste storage which will be reversible for a period of at least a hundred years. The site and the artificial barriers of repository must ensure the long-termed and sufficient insulation ability for the purpose of human and environment protection.

On the one hand, the disposal performance should be ensured, on the other hand, available technologies and economic factors are indispensable to be taken in consideration. The assessment of security is mainly from three parts: the glass waste storage package; the repository which contains the packages; the geological barrier (natural rock) of the site. Basic characteristics of barriers should contain: capacity for produced heat dissipation; reduction of generate mechanical stress intensity; chemical behaviour with regard to the corrosion of containers and radionuclide which would be accentuated by the increasing temperature.

Currently, there are three main types of preferential host rocks in the world: argillites, saline formations and granites. In France, following over a decade of studies by ANDRA, the acquired data show that the seismically stable geological layer of argillite which dates back from the Callovo-Oxfordian (COx) age and locates in both Haute Marne and Meuse, on the site of Bure, has favourable characteristics (high compactness and low permeability) for the storage of highly active and long-lived radioactive wastes. More importantly, argillite are subjected to solicitations of different origin: stress variation due to cavity excavation, change of water saturation degree (drying and re-saturation), variation of temperature and chemical reaction processes. In particular, during the long-term repository, gas phase (H_2) may probably generate which is mainly due to the corrosion of metallic structures. This thesis principally aims at the investigation of gas migration properties through the repository formation for the purpose of performance assessment and safety evaluation.

This chapter provides a review on the physical, mechanical and porous space characteristics of COx argillite. Subsequently, attention is drawn to the principal sources of generated gas and several basic gas migration mechanisms. It also includes a presentation of some experimental studies related to the gas breakthrough pressure.

2 Properties of COx argillite

2.1 Physical and mechanical characteristics of COx argillite

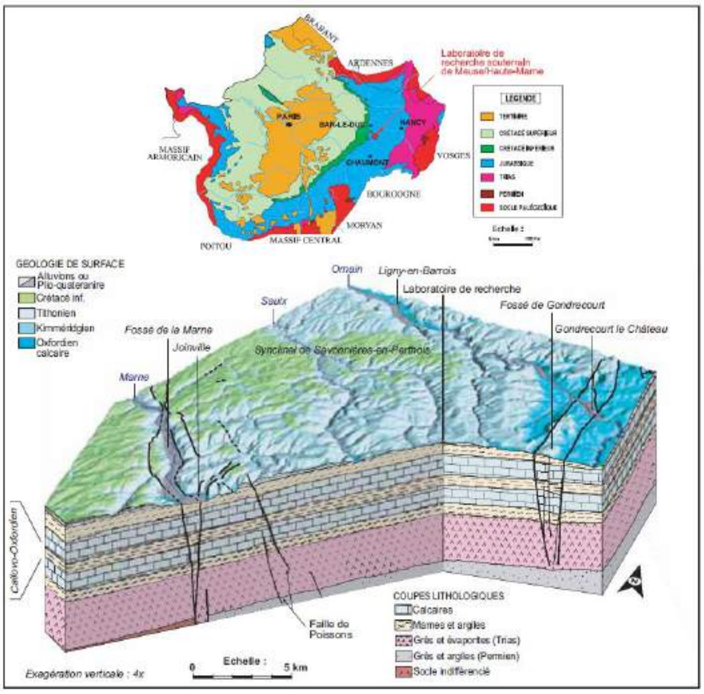

Figure 2.1: Block diagram of the geological formations of Meuse / Haute-Marne [Andra, 2005].

The COx argillite layer is aged about 150 million years in the Paris basin. At the site of Bure, it is between 420 and 550 meters deep [Andra, 2005]. The block diagram of the geological formations of Meuse / Haute-Marne is shown in Figure 2.1. The layer is located far from large geological faults thus ensures a relatively stable state. Moreover, it is regular and homogeneous over a large area. Due to the dip-slip faults towards the north-west,

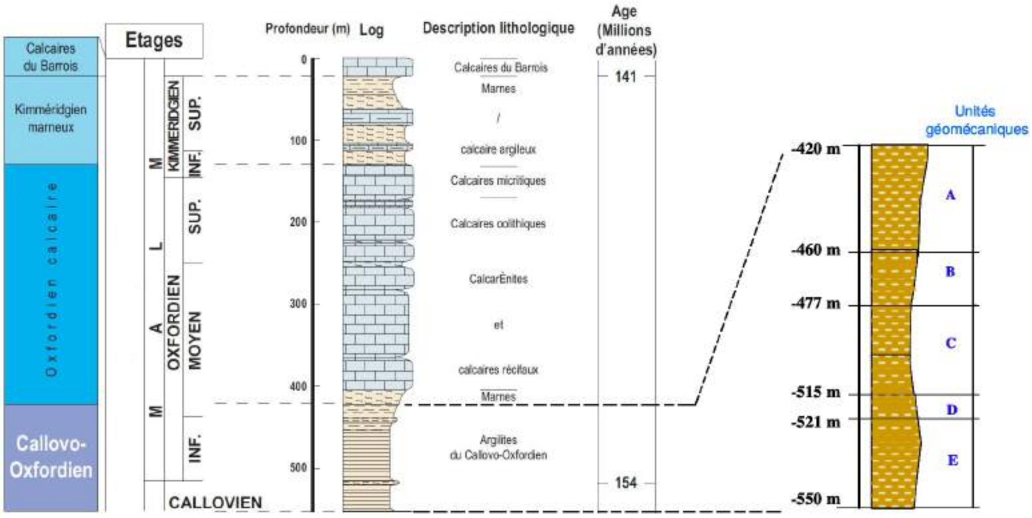

Figure 2.2: Geological sections and definition of geomechanical units of COx argillite [Andra, 2005][Yang, 2008].

Table 2.1: Common physical and mechanical characteristics of unit C of COx argillite [Su, 2005].

Parameters	Unit	Value
Apparent density	$kN.m^{-3}$	2400
Total porosity	%	18
Uniaxial compressive strength	MPa	21
Young's modulus	MPa	4500
Thermal conductivity	$W.m^{-1}.°C^{-1}$	$1.3\ (\perp),\ 1.9\ (\parallel)$
Specific heat capacity	$J.°C^{-1}.Kg^{-1}$	1100
Hydraulic conductivity	$m.s^{-1}$	5.10^{-13} to 5.10^{-14}

the depth gradually increases to more than 600 m with a distance about 15 km towards the north. Meanwhile, the thickness of the formation varies from 130 m to 160 m from the south to the north-west. This material belongs to an intermediate class between soils and rocks and a relatively simple geological domain. Argillites are more resistant than soils and possess similar physical and mechanical properties to rocks [Coll, 2005], they are compact and very low permeable to fluids. These characteristics are extremely important for a potential host rock in the context of radioactive waste storage.

At the mesoscopic scale, the COx argillite is mainly composed of clay minerals, carbonate, quartz grains. The mineralogical compositions vary with the depth and show a significant influence on pore size [Robinet, 2008][Robinet et al., 2012b]. According to the geomechanical studies by ANDRA, the argillite layer can be divided into 5 homogeneous geomechanical units (noted from A to E) (see Figure 2.2). Among them, the middle unit C in which an underground laboratory is constructed, is considered to possess the maximum clay content, which results in higher deformability and higher homogeneity of the mechanical properties. These common physical and mechanical characteristics are presented in Table 2.1.

2.2 Pore space characteristics of COx argillite

Interconnected pores are presented in porous medium which would contribute to fluid permeability. Hence, the transfer properties are determined by some physical properties such as porosity, pore size distribution, or specific surface area [Yang and Aplin, 1998]. The generally used total porosity Φ_t is the ratio between the pore volume V_p and the total volume V_t. The total volume consists of the volume of the solid phase V_s and the volume of the pores V_p. The total porosity is defined as:

$$\Phi_t = \frac{V_p}{V_p + V_s} \tag{2.1}$$

To quantify the porosity it is thus necessary to measure two values among the three volumes: pore volume V_p, total volume V_t and solid phase volume V_s for a sample. When measured on centimetric samples, the macroscopic porosity ϕ of COx argillites ranges between 14 - 22% [Yven et al., 2007].

Pore size distribution has a major influence on fluid movement properties in porous media. In comparison with other porous materials, due to the nanometer magnitude of pores, the characterization of pore size distribution in argillite is relatively difficult. In the COx formation, pore size distribution has been studied using various indirect methods including mercury intrusion porosimetry (MIP), water adsorption and desorption (WA/WD) and nuclear magnetic resonance (NMR).

Mercury porosimetry allows indirect identification of the distribution of pores. Indeed, mercury penetrates from the boundaries of a sample then fills the empty connected pores by applying a continuous increasing mercury pressure. Based on the assumption of cylindrical pores and Laplace law, the relationship between the pore diameter d and the applied pressure P_g is given as:

$$d = \frac{4\gamma\cos\theta}{P_g} \tag{2.2}$$

where γ stands for the surface tension and θ represents the wetting angle. For each pressure stage, the injected volume of mercury quantifies the accessible pore volume associated with the current capillary pressure. The total injected volume estimates the void volume of material. With a pressure between 3 KPa and 400 MPa, the investigated pore diameters range between 400 µm and 3 nm. Whereas, shortcomings exist, for instance, the mercury injection can not take place in non-connected pores; accessible pore form is assumed as cylinder; high injection pressure which is about 400 MPa may change the volume of solid phase and create a new porosity following micro or macro cracks.

The isotherm adsorption of water vapour or inert gas (nitrogen or argon) is used to measure the amount of adsorbed gas. With this method, pore size distribution can be defined with pores larger than 2 nm. Since the initial states of sample could be defined as totally dried or partially dried, adsorption and desorption methods are feasible for these two cases. Boulin [Boulin, 2008] obtains an isothermal adsorption from a dried sample at 70 °C. Andra [Andra, 2009b] performs on the one hand an isothermal desorption and on the other hand an adsorption using a sample partially saturated with water (80%). Pore size is determined by assuming cylindrical form and by using Kelvin-Laplce law to link the relative humidity and pore size:

$$d = -\frac{4\gamma \cdot M_w}{R \cdot T \cdot \rho_w \cdot ln(RH)} \tag{2.3}$$

Where M_w is the molar mass of water, R the perfect gas constant, T the temperature and ρ_w the density of water.

The method of nuclear magnetic resonance measures the response of the protons spins of non-structural parts (only those of water) during the application of induced magnetic fields. The analysis of transverse relaxation time which characterizes the time needed for protons to return to equilibrium state following the magnetic disturbance can be used to estimate the distribution of pore diameters. According to [Lowden et al., 1998], the relaxation time T_2 mainly depends on the surface relaxation ρ and the ratio between the surface S_p and the pore volume V_p. For a cylindrical pore, it equals to the reciprocal of pore diameter, then leads to:

$$\frac{1}{T_2} = \rho \cdot \frac{S_p}{V_p} = \frac{\rho}{d} \tag{2.4}$$

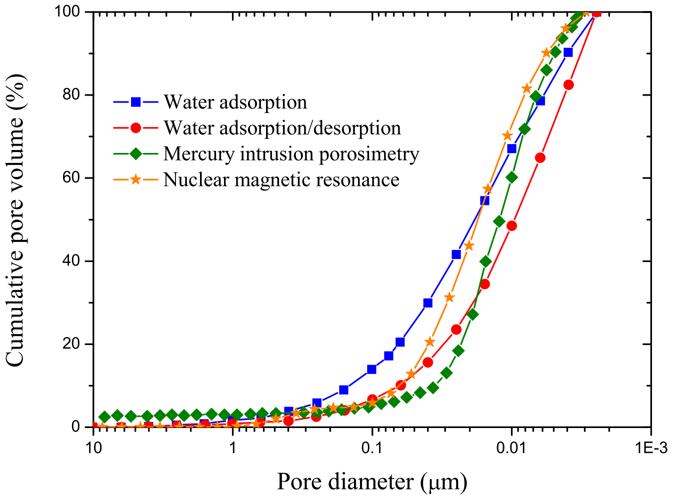

(a) Cumulative pore volume and distribution.

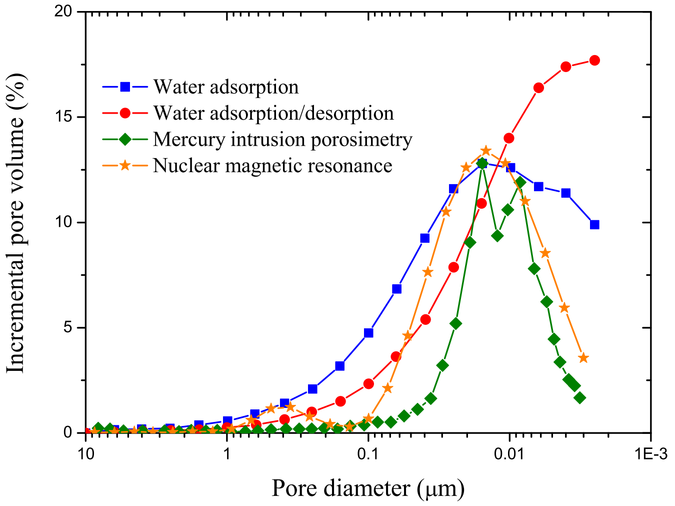

(b) Incremental pore volume and distribution.

Figure 2.3: Pore size distribution in COx argillites obtained by different methods, comparison with same total porosity in [Robinet et al., 2012b].

Mercury intrusion porosimetry, water adsorption and desorption and nuclear magnetic resonance tests show same value ranges of pore size distribution in 1 nm - 500 nm and similar evolutions [Andra, 2009b][Boulin, 2008][Robinet et al., 2012b], see Figure 2.3. Due to sample preparation and measuring technique, differences among experimental distributions are explicable. In particular, MIP method is more sensitive to "pore throat" (smaller than 30 nm) thus leads to high fraction of this range. In MIP, boundaries of sample are subjected to increasing pressure for mercury invasion. During this process, large pores locate behind small pores (ink-bottle pores) require higher pressure for access than the pressure for direct invasion. Thus, large pores are accumulated to smaller ones and their volume may be underestimated [Xu et al., 1997]. To the same purpose, WA method shows a relatively higher fraction of large pores (100 nm - 500 nm) and NMR indicates a higher proportion in medium size range (30 nm - 100 nm). In addition, geometric and topological properties such as pore shape, connectivity, tortuosity have been investigated by direct imaging techniques. In [Robinet et al., 2012a], X-Ray micro-tomography reconstructs a 3D porous network model with minimum pore size about 700 nm which is insufficient to show connected porosity. Some other methods, for instance, FIB/SEM (Focused Ion Beam/Scanning Electron Microscopy) and TEM (Transmission Electron Microscopy) are capable to provide relatively higher resolution images. In [Song et al., 2015], 3D geometry of the pore network in the mesoscopic clay matrix of COx argillite is studied by FIB/SEM and TEM imaging and used to to predict fluid permeability at the scale of the clay matrix, and compare it to macroscopic measurements. Advantages of direct imaging techniques are remarkable since accurate pore space model is directly obtained from sample. Nonetheless, expensive cost and substantial experiment duration need to be taken into account. Besides, results obtained from imaging techniques may show divergences due to sample preparation and measuring operations. Up to this point, in the following study, the strategy is to maintain the capacity of imaging techniques in characterization of topological properties, and meanwhile provide a realistic porous space morphology with which image analysis could be conducted to predict the fluid migration. In chapter 3, based on experimental data, 3D pore space models are generated using excursion set theory on Random Fields.

3 Gas production and migration in repository formation

3.1 Gas production in long-term repository

During the process of construction of radioactive waste repository and the following long-term storage after sealing. Gas phase may probably generate and contact with the host rock formation, according to various conditions. The main sources of gas involve:

- The corrosion of metallic parts which mainly generates hydrogen; For instance, the anaerobic corrosion of steel following chemical reaction of: $3Fe + 4H_2O \rightarrow Fe_3O_4 + 4H_2$.

- The degassing process in the clay formation, mainly due to the release of gas dissolved in the interstitial fluid in response to changes in temperature and pressure. For instance, dissolved CO_2 or CH_4 which is produced by chemical reactions of certain minerals.

- Gas produced by bacterial or microbial activities in favourable conditions such as sufficient nutrients.
- Gas produced by oxidation reactions of certain minerals (such pyrite).
- Radioactive waste decay.
- Water radiolysis by nuclear radiation.

Among these diverse sources, due to the low fluid conductivity of rock formation, the corrosion of metallic parts may last a long period of time and induce continuous production of hydrogen. Therefore, comparing with the limited amount of dissolved gas into the interstitial fluid, the continuously produced hydrogen will accumulate and a gas phase will form [Horseman and Volckaert, 1996]. The gradually increasing gas pressure will consequently induce a movement of the interstitial fluid. If no process ensures a discharge of the gas from the storage, the value of gas pressure can be very high and then lead to a fracturing of the formation. Furthermore, due to the chemical nature of hydrogen, a sudden degassing would be harmful to the environment and would be accompanied by a leak of radioactive waste. Considering these, it is then imperative to avoid such harmful consequences. Hence, the investigation of gas transport is of high relevance in the assessment of repository performance.

3.2 Gas migration in formation

During the long-term repository, following the corrosion of metallic materials, the production of gas, mostly hydrogen, will continue for a very long period, higher than 100000 years. The gas pressure will increase in the confined space of storage and it could be very high, which represents a critical pressure for structure. It is necessary to study the transfer of gas under pressure in pores of the host formation and even in the damaged area. Generally speaking, Gas transport through low-permeable rock formation is not only controlled by rock mass properties (intrinsic permeability, porosity, etc.), but also govern by hydro-mechanical state of the rock (water saturation degree, porewater pressure, stress state). Based on micro-structural conceptualization of the low-permeable rock mass, 4 modes of gas transport are concluded in [Marschall et al., 2005]. They are:

- Advective and diffusive transport of dissolved gas in porewater.
- Capillary induced two-phase flow.
- Gas flow according to the generation of micro-cracks.
- Gas migration with hydro or gas fracturing.

In [Marschall et al., 2005], the investigated material is Opalinus argillite. The subdivision of these basic transport mechanism is illustrated in Figure 2.4 based on phenomenological considerations. These different transport processes are discussed in the following sections.

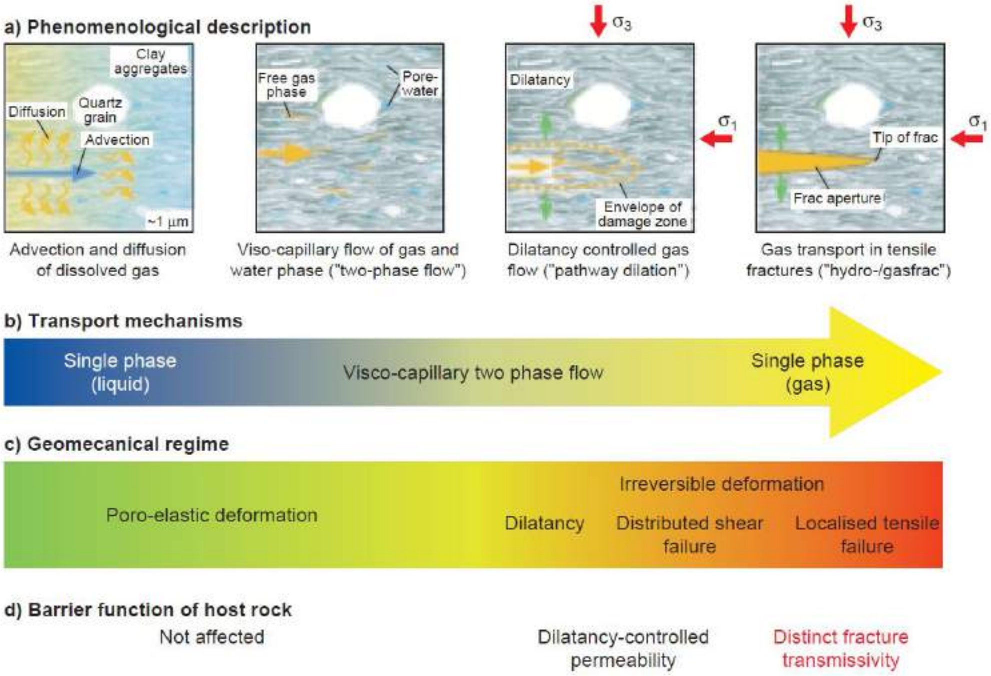

Figure 2.4: Classification and analysis of gas transport processes in Opalinus Clay: a). phenomenological description; b). transport mechanisms; c). geomechanical regime; d). effect of gas transport on the barrier function of the host rock. [Marschall et al., 2005].

3.2.1 Diffusive transport of dissolved gas

When gas phase under complementary pressure is in direct contact with a saturated porous medium, the transfer of gas into the porous medium can occur following two different modes: in dissolved phase in interstitial fluid and in gas phase in pores. Dissolution of the gas in interstitial fluid is limited by the solubility of gas in fluid. Henry's law describes the solubility of gas in porewater and evaluates the maximum amount of gas dissolved according to the applied gas pressure.

Gas migration in the interstitial fluid is generally governed by two phenomena:

- Advective groundwater flow.
- Diffusion of dissolved gas in porewater.

Advective groundwater flow results from a hydraulic head gradient. It is described by Darcy's law. In very low permeability porous media such as argillites, the effect of advection is restricted. Thus the gas dissolved in interstitial fluid migrates mainly by molecular diffusion due to concentration gradients, which is described by Fick's law. This type of transport occurs even at low gas pressures according to pressure-dependent dissolution of gas in porewater. The main parameters affecting the transport behaviour of dissolved gas are Henry's coefficient, the diffusion coefficient in water, the tortuosity, the accessible porosity and the hydraulic conductivity.

3.2.2 Visco-capillary two-phase flow

Assuming that the volume of porous space does not increase proportionally to the generated flow before the fracture threshold, when the gas migration velocity in rock formation following the dissolution kinetics is much lower than gas production velocity following the corrosion of steel, gas pressure increases then leads to the flow of the gas phase in the pore network, by pushing the interstitial fluid. At the gas-water interface, the pressure difference is related with the pore size by Young-Laplace's law. In other words, this difference controls the stability of gas - water interface and determines the gas invasion in porous medium. If the pressure difference between the gas and the interstitial fluid overcomes the capillary pressure, gas will remove the interstitial water in a portion of the porosity. Since the capillary resistances are relatively high in small pores, gas preferentially migrates into the larger interconnected pores. Thus the capillary two-phase flow occurs.

In traditional methods, assuming a uniform distribution of gas flow through the REV (Representative Elementary Volume), the two-phase flow mechanism can be described by using Darcy's law and mass conservation law. Moreover, once the gas invasion begins, the gas mobility is controlled mostly by the intrinsic permeability of the formation, the permeability-saturation relationship (relative permeability), and the relationship between the capillary pressure and the water saturation (suction or water retention curve). The functional dependency between the pore space saturation and the relative permeability or the capillary pressure are commonly described with parametric models. For instance, Van Genuchten-Mualem and Van Genuchten-Burdine (VGM and VGB) model; Brooks-Corey-Burdine (BCB) model; Brustsaert-Burdine (BRB) model; Gardner-Mualem (GDM) model [Chen et al., 1999].

3.2.3 Dilatancy-controlled gas flow

Another possible gas migration mechanism is related to the penetration of gas into the texture and structure of the mineral phases. The corresponding pathway dilation is important for argillaceous media with low tensile strength [Horseman et al., 1996]. This transfer is dependent of the contact forces between the mineral phases. If the long-term gas pressures with a magnitude greater than the minimum principal stress acting on the rock mass, the gas pressure locally increases to overcome the contact forces then it dilates the porosity and gas phase may then penetrate into a local porosity. At the microscopic scale, this process corresponds to the increase of pore space and the generation of local micro-cracks. Moreover, in this process, gas migration can be also seen as capillary two-phase flow. Whereas, transport properties of the solid phase could not be seen as invariant due to rock deformation. If the gas pressure further decreases, the initially created micro-porosity shrinks and water may ultimately fill the entire porosity which is associated to the swelling of clay minerals with micro-cracks. For COx argillite, the micro-crack threshold is about 9 MPa [Andra, 2005].

3.2.4 Gas transport along macroscopic tensile fractures

If the gas pressure continues increasing, it is possible to exceed the sum of the minimum principal stress and the macroscopic tensile fracture threshold of material then create fracture with orientation perpendicular to the minor strain direction. The macroscopic fracture is initiated quasi-instantaneously. During this gas movement which is related to mechanical mechanism, two-phase flow is no longer an appropriate mode. Indeed, since water can not move in front of the gas penetration flow, gas flow in macroscopic fracture is then defined as a single-phase flow process. For COx argillite, the fracture threshold is about 12 MPa [Andra, 2005].

4 Gas breakthrough experiments

In [Hildenbrand et al., 2002b], gas breakthrough migration process includes the creation and propagation of preferential pathways through porous network. Gas entry is defined as the beginning of gas invasion into the porous material, gas breakthrough is reached when gas passes from one side to the other of the porous network and meanwhile a continuous flow forms. Experimentally, the essential idea of gas breakthrough experiment is to accurately detect gas presence on the downstream side of a sample under hydrostatic stress with similar in-situ values.

Considering this, several experimental hypothesis are proposed and applied. For measurement approach of the breakthrough pressure, it is common to use the step-by-step approach which is conducted by stepwise pressure increase by gas (non-wetting phase) at inlet [Ibrahim et al., 1970][Ito et al., 2011]. For instance, in [Duveau et al., 2011], the basic idea is to impose a slowly increasing gas pressure on the upstream side of sample until measuring gas leakage on the downstream side. At the outset, two porous, stainless steel disks are placed on each side the sample in a triaxial cell, see Figure 2.5, for the purpose of fluid injection and leakage and meanwhile avoid argillite leakage through the fluid pipes. Afterwards, sample will be subjected to a confining pressure with similar value with in-situ levels. Following this, water injection is performed to obtain a fully saturated porous space. This state is achieved when water permeability values fall below (10^{-19} to 10^{-21} m^2). This saturation process lasts for several weeks. After these preparing work, increasing argon gas pressure at very low rate is applied on the upstream side until the gas leakage at the downstream side. Moreover, the measuring of gas presence at the downstream side is conducted with a pressure transducer and a argon gas detector. It should be noted that, for this experiment, it exists two shortcomings: 1, as soon as gas pressure is applied on the sample upstream side, fluid pressure increases systematically on the downstream side, whatever the upstream gas pressure value (as low as 0.2 MPa). This is probably due to water drainage process with applied gas on the upstream side. Thus, the gas entry pressure is not available to be detected in this test; 2, this method of gas detection does not ensure the mechanism of gas breakthrough process, whether by diffusion of dissolved gas or by capillary two-phase flow. Results show that gas breakthrough pressure ranges between 1.26 MPa and 3 MPa, depending on the sample considered and on its height. It should be noted that micro cracks generated during the sample preparation process may reduce the estimated values. The influence of confining pressure is not evident. Moreover, in that work, a clear influence from bedding plane has been observed. Gas breakthrough pressure along the bedding planes is much lower than perpendicular to it.

Another interesting breakthrough experiment is performed in [Hildenbrand et al., 2002b][Hildenbrand et al., 2002a][Hildenbrand et al., 2004] with a different protocol. In these works, the initial preparing work is the same. Sample is firstly subjected to constant single-phase flow to ensure the complete water-saturation of the conducting pore system. Since the traditional idea of continuously increasing the gas pressure until breakthrough occurred would have resulted in prohibitively long durations of experiments. Moreover, a high increasing rate of pressure may easily leads to overestimation of breakthrough pressure. Considering this, the new idea is to impose instantaneously a high gas-pressure which exceeds the expected gas breakthrough pressure at the upstream side thus the high pressure gradient leads to a quick gas invasion process. The measured gas flux is related to the pressure changes in both upstream side and downstream side and the corresponding

Figure 2.5: Gas breakthrough experiment with increasing upstream gas pressure [Duveau et al., 2011].

gas phase permeability. The two experimental modes (a). constant pressure at the upstream side and (b). fixed upstream gas volume are illustrated in Figure 2.6. For these two modes, gas breakthrough occurs and lasts for several days after the start of experiment. Downstream pressure increases after a certain lag time and approaches the upstream pressure. Ultimately, a constant residual pressure difference may be reached and gas flow stops. More importantly, after that the effective gas permeability increases and reaches its maximum value, drainage stops and the pressure difference decreases thus leads to an imbibition process. Gas conducting flow pathways would be progressively reduced until that the effective permeability drops to zero. The constant residual pressure difference at the last stage is called as the minimum capillary displacement pressure and used to describe the gas breakthrough characteristic and estimate the capillary sealing efficiency. Results show that the minimum capillary displacement pressure ranges between 0.06 to 6.7 MPa for the considered materials (Tertiary mudstone and Boom clay).

Comparing with the easily overestimated gas breakthrough pressure from drainage process, the experimentally measured residual pressure difference may be lower than the true value if re-imbibition is impeded. A detailed explication of issue is made in chapter 5. Some experiments for COx argillite are conducted by different partners of Andra [Andra, 2009a]. Principal results show a gas entry pressure less than 3 MPa without massive gas invasion using a drainage pathway scheme when a gas breakthrough pressure in a range

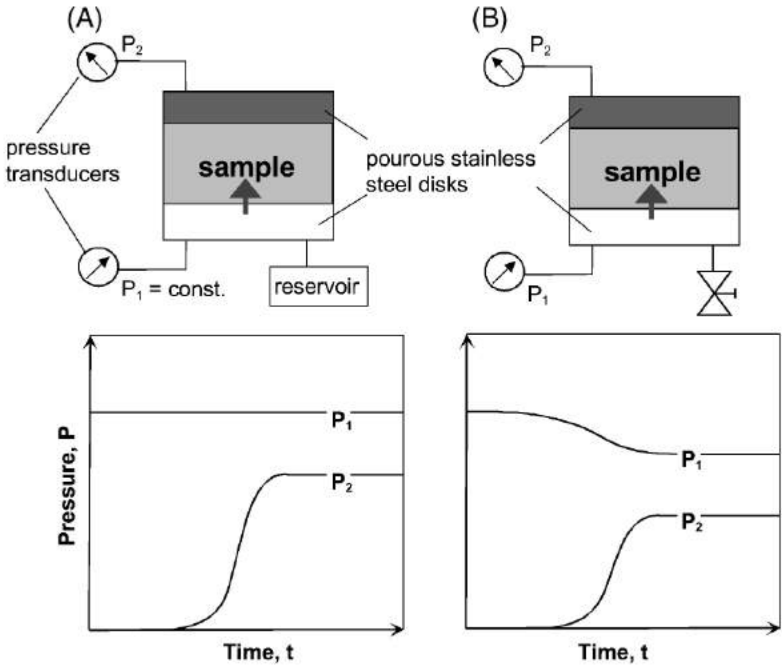

Figure 2.6: Two experimental modes used in [Hildenbrand et al., 2002b][Hildenbrand et al., 2002a][Hildenbrand et al., 2004], (A), constant pressure at upstream side; (B), fixed upstream gas volume.

of 4 MPa to 5 MPa was determined using an imbibition scheme.

Furthermore, in [Gallé, 2000], a model for gas migration at the Fo-Ca clay/metal overpack interface, which predicts an order of magnitude similar to gas breakthrough pressure. In [Davy et al., 2009], the experimental investigation of gas migration properties takes place in a mock-up which consists a bentonite plug inside an argillite host rock sample. The principal process consists (1), placement of an unsaturated bentonite plug inside an argillite sample (see Figure 2.7), (2), swelling of bentonite through water flow, (3), application gas pressure. For a fully water-saturated bentonite of initial 1.6 g.cm^{-3} dry density, the expected swelling pressure is 7 MPa. When such bentonite is subjected to 5 MPa interstitial water pressure, which corresponds in-situ value of 500 m depth, gas migration is expected at a pressure slightly above 12 MPa [Horseman et al., 1999]. After sufficient swelling, bentonite-argillite mock-ups have an average water permeability of 2.10^{-21} m^2, on the order of that of bulk argillite. Hence, after sufficient swelling, bentonite provides a highly impermeable seal, equivalent to that of the argillite host rock. The critical pressure corresponds that a sudden bubble gas release is observed through an outlet transparent tube. Gas flow is already detectable below this pressure [Pusch and Forsberg, 1983]. Results show that the critical pressure for bentonite-argillite mock-ups ranges between 3.4 MPa - 5.3 MPa thus enhances the idea that gas breakthrough is possible in mudrocks at gas pressures much lower than confining pressure or fracture threshold.

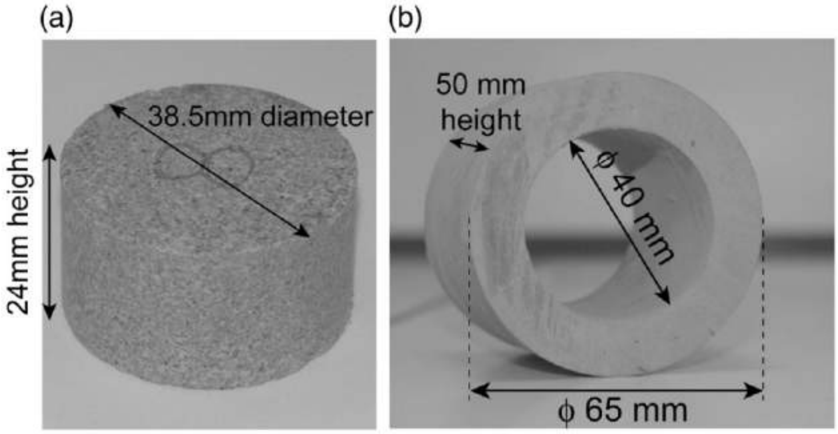

Figure 2.7: Photograph of (a): a pre-compacted bentonite plug; (b): an argillite tube after coring and top and bottom surface grinding [Davy et al., 2009].

5 Conclusions

In the context of radioactive waste storage in deep geological formation, the repository system consists of the waste packages, engineered barriers and the geological barriers. The geological barrier ensures the long-term performance and security. In France, following the studies of ANDRA, the Callovo-Oxfordian argillite layer with relatively homogeneous quality, high compactness and low permeability is chosen as a privileged candidate material for host rock.

Interconnected pores are presented in porous medium which would contribute to fluid permeability. Due to the nanometric magnitude of pore size, the investigation of porous space characteristics in argillite is relatively difficult. Some indirect methods such as mercury injection, water adsorption and desorption, nuclear magnetic resonance show same value ranges of pore size distribution in 1 nm - 500 nm and similar evolutions.

Due to the corrosion of metallic parts in the structure, the gas production will last for a very long period. Apart from a small proportion of gas which will dissolve in the interstitial fluid according to Henry's law and diffuse in saturated porous space following Fick's law, the generated gas will accumulate thus lead to a continuous increase in its pressure. When the gas pressure is sufficient to overcome the capillary resistance, gas phase can penetrate into the porous medium by moving the interstitial water. Gas migration is also possible by coupling with the mechanical behaviour such as pathway dilation with gas pressure larger than the contact forces between the mineral phases. This process corresponds to the generation of micro-cracks. Ultimately, if gas pressure excesses the macroscopic fracture threshold, fracture then appears with orientation perpendicular to the minor strain direction. Consequently, the investigation of gas transport is of high relevance in the assessment of repository performance.

Gas breakthrough pressure is defined as the least applied gas pressure with which gas phase passes from one side to the other of the porous network and meanwhile a continuous flow forms. Some existing gas breakthrough experiments investigate the gas breakthrough pressure principally following two scenarios: during the drainage process or during the imbibition process. Results show that gas breakthrough is possible in argillite at gas pressures much lower than confining pressure or fracture threshold.

In the following chapter, focus will be drawn to the creation of a realistic pore space morphological model using excursion set theory.

Chapter 3

Morphological reconstruction of porous space

Contents

1 Introduction

In this chapter, focus is made on the generation of realistic morphological models of porous network for the following prediction of gas migration properties. The method based on the excursion set of Gaussian Random Field that provides complex randomly shaped morphologies will be presented. Some common numerical approaches for the representation of heterogeneity are based on simple objects with defined geometrical shapes. For instance, in [Bezrukov et al., 2002], random packings of spheres with arbitrary diameter distribution are generated from different algorithms which determine the isotropic packings density. In the study of [Bezrukov and Stoyan, 2006], random packings of ellipsoids of revolution are generated. In regards with the simulation of two phases (pores and matrix) in porous medium, porous space is usually considered to be composed of particularly shaped pores such as cylinders with calibration parameters in [Ranaivomanana et al., 2011] or spherical elements connected by cylindrical channels in [Varloteaux et al., 2013] for the simulation of cement-based materials. These methodologies, due to the use of simple and assumed geometrical definitions, provide non-realistic morphology of the medium and may influence the accuracy of gas movement description.

Moreover, some direct imaging techniques such as X-Ray micro-tomography, FIB/SEM and TEM provide 3D geometrical information about the pore network. In [Robinet, 2008] and [Robinet et al., 2012b], based on X-Ray micro-tomography experiment data, pore space is reproduced with voxel size about 700 nm. However, for clay rocks such as COx argillite, the resolution level is insufficient to comprise the majority of pores between 3 nm - 700 nm thus no connected porosity is detected and gas migration prediction is infeasible in this case, see Figure 3.1. Higher resolution images could be obtained with FIB/SEM methods which are down to 10 - 20 nm voxel size or with TEM/STEM techniques which are down to 1 nm pixel size. In [Song et al., 2015], 3D geometry of the pore network in the mesoscopic clay matrix of COx claystone is obtained by FIB/SEM and TEM imaging. An example is illustrated in Figure 3.2. Advantages of direct imaging techniques are remarkable since realistic porous space models are directly obtained from real samples. However, some shortcomings such as expensive cost and substantial experiment duration need be taken into account. Furthermore, some divergences may exist in results due to sample preparation and measuring operations.

As introduced in the first place, excursion set can construct randomly shaped porous space. Simply speaking, it depends on a thresholding process and Random Field basic characteristics (mean, variance, correlation length), transforms a continuous Random Field to a multiphasic model with stochastic spatial space. Since the geometrical and the

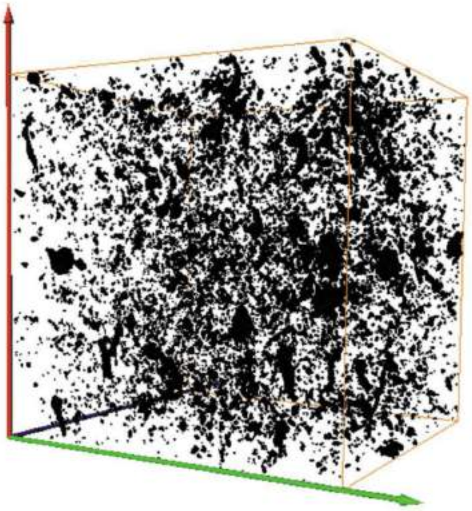

Figure 3.1: 3D pore space model of a sample of COx claystone obtained by micro-CT, from [Robinet, 2008] and [Robinet et al., 2012b].

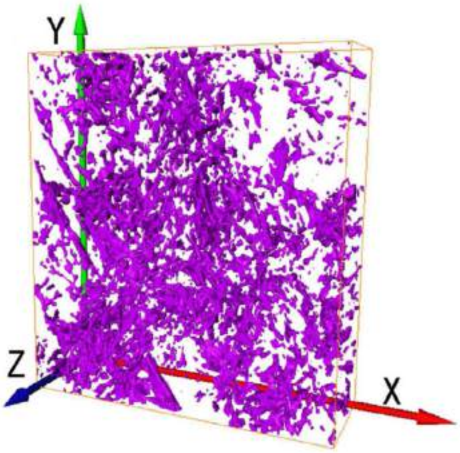

Figure 3.2: 3D pore space model of a sample of COx claystone obtained by FIB/SEM, from [Song et al., 2015].

topological properties are under statistical control, the generated morphological model can not only represent the heterogeneity, but also respect the experimental pore volume increments. Over the few past years, the excursion set theory of Random Fields has been widely applied to precisely describe the geometric information and the topological characteristics about the spatial structure of sample, such as concrete in [Roubin et al., 2015] and cement paste in [Hosseini, 2015]. In this chapter, numerical realizations of porous network in COx argillites are obtained through this method.

Subsequently, the analysis of topological and geometrical properties of the generated model is performed by using morpho-mathematical operations such as morphological opening and geodesic reconstruction. Mathematical morphology was from the collaborative work of Georges Matheron and Jean Serra [Matheron, 1975][Serra, 1982][Serra, 1988]. It is a theory and technique for the analysis and processing of geometrical structures, based on set theory, lattice theory, topology, and random functions. It is most commonly applied to digital images, but it can be employed as well on graphs, surface meshes, solids, and many other spatial structures. Some topological and geometrical characteristics such as size, shape, convexity, connectivity, and geodesic distance are capable to be measured using mathematical morphology. It is also the foundation of morphological image processing, which consists of a set of operators that transform images according to the above characterizations. The basic morphological operators are erosion, dilation, opening and closing. In this chapter, numerical implementation of these basic operations is applied to calculate open porosity and pore size distribution in the generated model for the purpose of model verification and further application in the gas migration prediction.

2 Generation of morphological model

2.1 Random Field and Gaussian distribution

Simply speaking, a Random Field is defined as a stochastic process which takes values in a Euclidean space, and defined over a parameter space of dimensionality at least one. For a two-dimensional domain $K \subset \mathbb{R}^2$, a Random Field $\{RF(x) : x \in K\}$ is a set of real-valued random variables on a probability space $(\Omega, \mathcal{F}, \mathcal{P})$. For each $x \in K$, $RF(x) : \Omega \to \mathbb{R}$ is a random variable. The covariance function is defined by using mean function $\mu(x) = E[RF(x)]$, for $x, y \in K$:

$$C(x,y) = \mathrm{Cov}(RF(x), RF(y)) = E\Big[\Big(RF(x) - \mu(x)\Big)\Big(RF(y) - \mu(y)\Big)\Big] \tag{3.1}$$

For stationary random fields, $\mu(x)$ is a constant and the covariance depends on $x - y$. For the purpose of simplification, only strictly stationary Random Fields are considered. Moreover, $C(x,y)$ can be expressed in terms of a single variable $h = \parallel x - y \parallel$.

The statistical distribution of a Random Field follows its density probability function. Among the various types of distribution, the Gaussian, due to its smooth properties, is the most widely used type. The bell shaped density function of Gaussian distribution is given as:

$$f(x) = \frac{1}{\sigma\sqrt{2\pi}} e^{-(x-\mu)^2/2\sigma^2} \tag{3.2}$$

A Gaussian Random Field is a second-order field with the vector of random variables follows the multivariate Gaussian distribution for any x_1,..., $x_N \in K$. Since multivariate Gaussian distributions are determined by means and covariances, Gaussian random fields could be directly defined by their mean and covariance functions. Especially, for a zero mean Gaussian field, the covariance function can be easily defined by two parameters as:

$$C(h) = \sigma^2 \exp\left(-\frac{h^2}{L_c^2}\right) \tag{3.3}$$

in which σ^2 stands for the variance and L_c represents the correlation length. More importantly, correlation length possesses the major influence to the resulting morphology since it determines the length scale. With $L_c \to 0$, then $C(h) \to 0$ leads to decorrelated Random Fields. In contrast, with $L_c \to \infty$, then $C(h) \to \sigma^2$ provides constant Random Fields with variance σ^2. An illustration of influence of correlation length is shown in Figure 3.3. Considering the application for morphological representation of porous network, after the excursion of a Gaussian Random Field of single correlation length, pore sizes would distribute in a limit range with average value of the defined correlation length. A detailed introduction of this issue is made in the following sections.

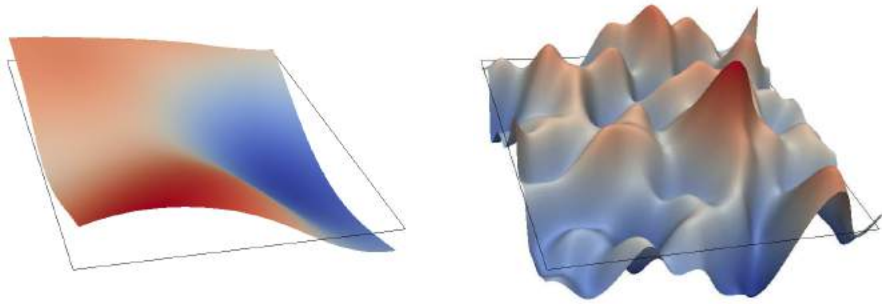

(a) Large correlation length (the domain size).

(b) Small correlation length (one-tenth of the domain size).

Figure 3.3: Illustration of the influence of correlation length in Gaussian Random Field [Roubin, 2013][Roubin et al., 2015].

2.2 Excursion set theory

According to [Adler, 2008], for a random function $f(x)$ of Random Field defined over a parameter space K which is a bounded region of N-dimensional Euclidean space $\mathbb{R}^N$,

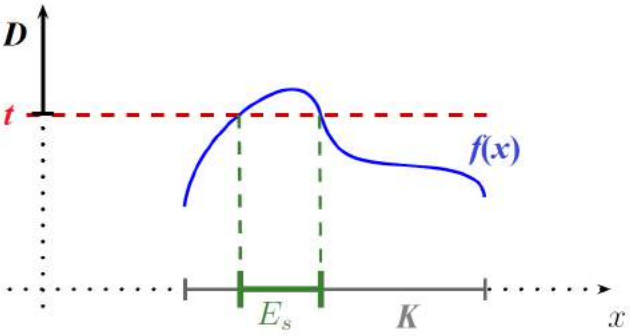

Figure 3.4: Excursion set theory in one-dimensional case, $D = [t, \infty[$ stands for the hitting set [Roubin, 2013][Roubin et al., 2015].

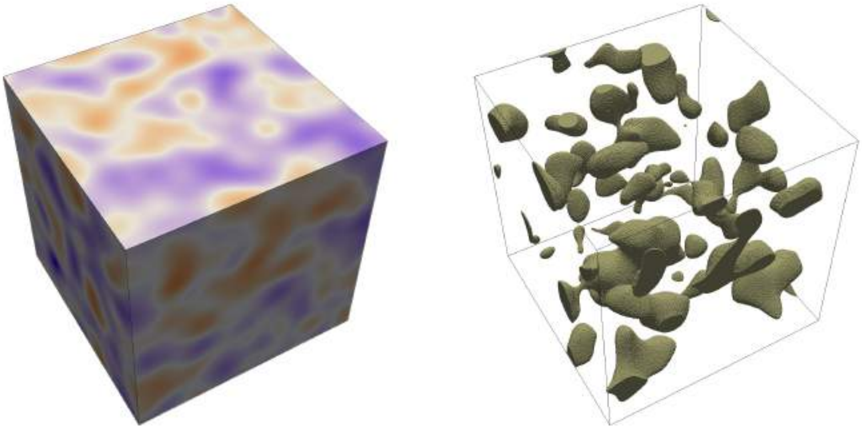

(a) Example of Gaussian Random Field. (b) Transformation to binary field.

Figure 3.5: Illustration of excursion set on a Gaussian Random Field.

thus $K \subset \mathbb{R}^N$. If D is a subset of R, then the excursion set E_s of $f(x)$ in D and over K is defined by:

$$E_s \triangleq \{x \in K \mid f(x) \in D\} \tag{3.4}$$

In general, the subset D is called as the hitting set and can be defined by a threshold t as [t,∞[. Then the excursion set represents those points in parameter space K at which $f(x)$ takes value above t and is written as:

$$E_s \triangleq \{x \in K \mid f(x) \geqslant t\} \tag{3.5}$$

An example of excursion set theory applied for one-dimensional case is shown in Figure 3.4. The application of excursion set for a Gaussian Random Field is shown in Figure 3.5, after the thresholding process, a continuous field is transformed to a discretized binary field.

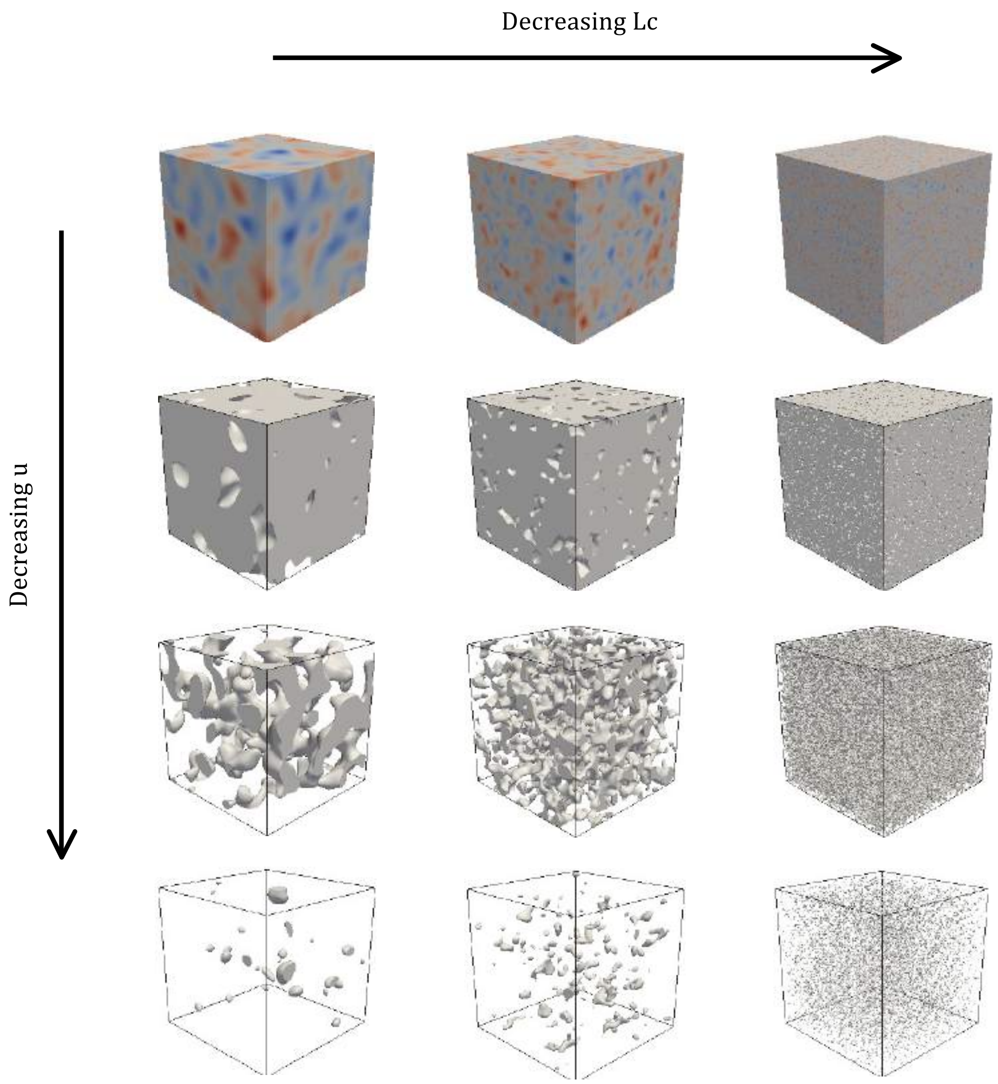

Figure 3.6: Various sorts of morphology through the variation of threshold and correlation length (u stands for the threshold) [Hosseini, 2015].

The chosen threshold t plays a key role in the resulting morphological aspects since it governs the volume fraction. Assuming that the E_s stands for the pore phase in porous medium and other parts represent the matrix. For low t, the corresponding E_s takes over the major region of space thus leads to high porosity morphology. This type of excursion corresponds to meat-ball like topology and can be used to represent disconnected media such as aggregates within a matrix [Roubin et al., 2015]. In contrast, high t leads to relatively lower porosity. The excursion is made of cavities and handlers thus is suitable for the representation of porous medium such as argillite. As mentioned before, a zero mean Gaussian Random Field can be defined by the variance and the correlation length. For the case of $\sigma^2 = 1$, correlation length can totally govern the probabilistic properties of Random Field, thus shows significant impact to the resulting excursion. Regarding the representation of porous space, correlation length assigns a certain characteristic length-scale and represents the average pore size in porous model. Hence, as illustrated in Figure 3.6, different kinds of morphology could be generated via the variation of these two parameters.

2.3 Geometrical and topological properties of morphology

In order to better understand the morphological model and accurately represent porous medium, the geometrical and topological properties have to be considered. According to the work of Adler[Adler, 2008], there exist various ways to quantify these properties, for instance, Quermassintegrals, Minkowski or Steiner functions, integral curvatures, intrinsic volumes and Lipschitz-Killing curvatures (LKC) [Federer, 1959]. Moreover, for N dimensional space, $N+1$ descriptors are supposed to be enough. Hence, in the three-dimensional Euclidean space, an excursion is fully characterized by a set of four descriptors: three geometrical and one topological. A specification of these descriptors could be made through the LKCs, denoted by $\mathcal{L}_j$, $j = 0,...,3$, where $\mathcal{L}_0$ represents the Euler characteristic, $\mathcal{L}_1$ is the mean diameter, $\mathcal{L}_2$ stands for the surface area and $\mathcal{L}_3$ the volume. In algebraic topology and polyhedral combinatorics, the Euler characteristic is a topological invariant which describes a topological space's shape or structure regardless of the way it is bent, commonly denoted by χ. The Euler characteristic is classically defined with polyhedron formula. For a convex polyhedron, Euler characteristic is the sum of the number of vertices (V), edges (E) and faces (F). Considering a solid which consists of P polyhedron glued together, the Euler characteristic is defined as:

$$\chi = V - E + F - P \tag{3.6}$$

It can be seen as a counter of dimensional objects and only determined by topological aspects. For three-dimensional excursions, the Euler characteristic can be linked with polyhedron formula and be given as:

$$\chi(E_s) = \#\{\text{connectedcomponent}\} - \#\{\text{handles}\} + \#\{\text{holes}\} \tag{3.7}$$

Considering that different types of media possess different topological features, the Euler characteristic is an useful property since it is directly related to the description of a material morphology. The investigation of geometrical properties is made by the other three LKCs.

For a Gaussian RF with zero mean, variance σ^2 and correlation length L_c defined in a cubic domain of size d, in order to link the probabilistic properties of Random Field and the threshold value t with the excursion properties, the expected fours LKCs of excursion with threshold t are computed as:

$$E\{\mathcal{L}_0(E_s)\} = [\frac{1}{\sqrt{2}\pi^2}\frac{d^3}{L_c^3}(\frac{t^2}{\sigma^2}-1)+\frac{3}{\sqrt{2}\pi^{3/2}}\frac{d^2}{L_c^2}\frac{t}{\sigma}+\frac{3}{\sqrt{2}\pi}\frac{d}{L_c}]e^{-t^2/2\sigma^2}+\Psi(t/\sigma) \tag{3.8a}$$

$$E\{\mathcal{L}_1(E_s)\} = [\frac{\sqrt{2}}{\pi^{3/2}}\frac{d^3}{L_c^2}\frac{t}{\sigma}+\frac{3}{2^{3/2}}\frac{d^2}{L_c}]e^{-t^2/2\sigma^2}+3d\Psi(t/\sigma) \tag{3.8b}$$

$$E\{\mathcal{L}_2(E_s)\} = \frac{\sqrt{2}}{\pi}\frac{d^3}{L_c}e^{-t^2/2\sigma^2}+3d^2\Psi(t/\sigma) \tag{3.8c}$$

$$E\{\mathcal{L}_3(E_s)\} = d^3\Psi(t/\sigma) \tag{3.8d}$$

2.4 Union theory

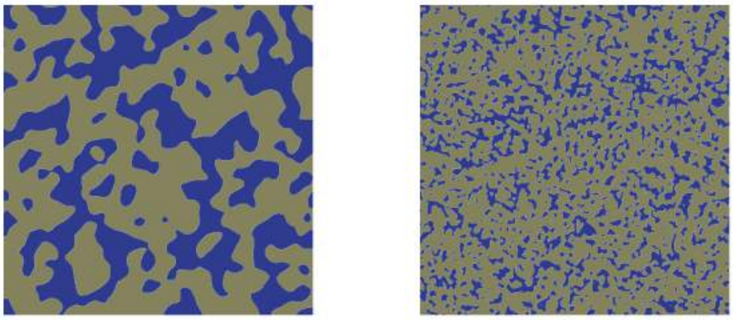

(a) Excursion 1 with large L_c. (b) Excursion 2 with small L_c.

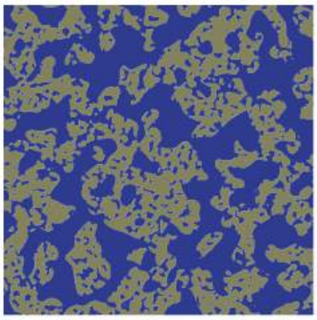

(c) Union of Excursion 1 and 2.

Figure 3.7: Illustration of union of two excursions with different L_c.

As introduced before, pore space geometry in COx argillite is anisotropic with characteristic sizes ranging between 1 - 500 nm. In order to generated an accurate model, the numerical pore size must distribute in a large interval and necessarily approaches to the experimental evolution. However, a single L_c morphological model shows a limited pore size distribution around L_c and an independent pore volume fraction determined by the

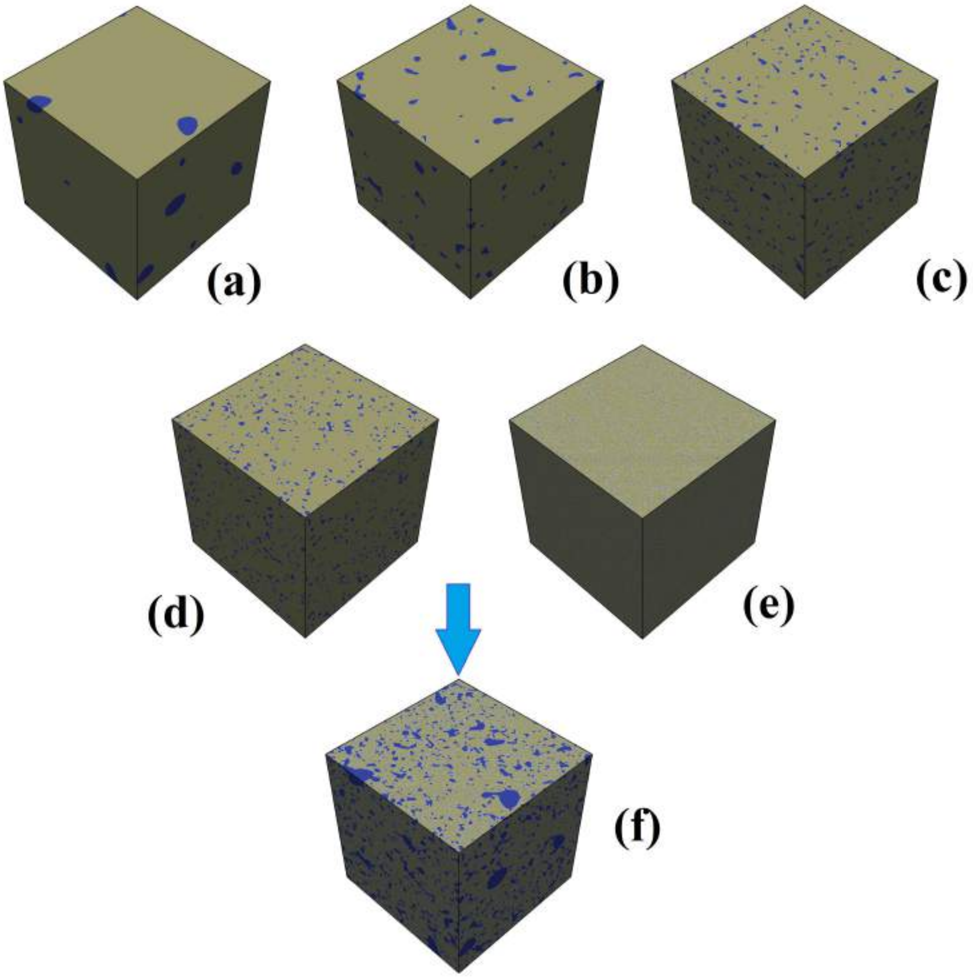

Figure 3.8: Illustration of union of five excursions with different correlation lengths; (a) to (e) are single excursions with decreasing correlation lengths and (f) is the resulting union.

chosen threshold t. Attention is now drawn to the feasibility of a single excursion with different correlation lengths and a good control of topological and geometrical properties. In [Roubin et al., 2015], this issue is treated by a new excursion defined through the union of several independent excursions which possesses multiple characteristic lengths and is given as:

$$E_s^{\cup} = \bigcup_{k=1}^{K} E_s^k \tag{3.9}$$

Figure 3.7 is an example for the two-dimensional case which illustrates the union Figure 3.7(c) of two single excursions (Figure 3.7(a) and Figure 3.7(b), $L_{c1} > L_{c2}$) defined in a same domain. The estimation of LKCs of the new excursion can be yield by:

$$\mathcal{L}_n(E_s^{\cup}) = \mathcal{L}_n(E_s^1 \cup E_s^2) = \mathcal{L}_n(E_s^1) + \mathcal{L}_n(E_s^2) - \mathcal{L}_n(E_s^1 \cap E_s^2) \tag{3.10}$$

Following this, a predictable approximation using the specific value which is referred as the specific surface area in two dimensions or the fraction volume in three dimensions is computed as:

$$\mathcal{L}_n(E_s^{\cup}) = \mathcal{L}_n(E_s^1 \cup E_s^2) \approx \mathcal{L}_n(E_s^1) + \mathcal{L}_n(E_s^2)\Big(1 - \mathit{\Phi}_N(E_s^1)\Big) \tag{3.11}$$

Assuming that $L_{c1} > ... > L_{ck} > ... > L_{cK}$, the LKCs of the union are determined by the LKCs of each single excursion and are defined by:

$$\mathcal{L}_n(E_s^{\cup}) \approx \mathcal{L}_n(E_s^1) + \sum_{k=2}^{K} \mathcal{L}_n(E_s^k)\left(1 - \bigcup_{m=1}^{k-1} \mathit{\Phi}_N(E_s^m)\right) \tag{3.12}$$

$\mathit{\Phi}_N$ can be expressed by Poincaré formula [Taylor et al., 2009]:

$$\bigcup_{k=1}^{K} \mathit{\Phi}_N(E_s^k) \approx \sum_{k=1}^{K}\left((-1)^{k-1} \sum_{1 \leqslant i_1 < ... < i_k \leqslant K} \mathit{\Phi}_N(E_s^{i_1}) ... \mathit{\Phi}_N(E_s^{i_k})\right) \tag{3.13}$$

In Figure 3.8, union operation is illustrated for 3D case. Five single excursions with different correlation lengths are ultimately combined in a same field thus enlarge the pore size range.

It is important to note that since the sizes of generated particles in a single excursion are spread around the correlation length, each excursions of the union represents a single class and its volume fraction is determined by the experimental pore size distribution. Following this, attention is now drawn to the overlap between two excursions since it leads to inaccurate estimation of pore volume fraction in the resulting union [Hosseini, 2015][Roubin et al., 2015]. In order to resolve this issue, the chosen threshold k of each excursion needs be target to get higher volume fraction than the wanted value to eliminate the overlap effect. For instance, considering a porous space with total porosity ϕ_t and with pore size principally located in three classes. Their volume fractions are assumed as $20\%\phi_t$, $30\%\phi_t$ and $50\%\phi_t$ respectively. After the generation of three Random Fields with each L_c equals to the average pore size of each class, the thresholding process should be performed with relatively lower t to increase the pore volume fractions. The input values are defined as:

$$\phi_1^{\text{new}} = \phi_1 = 20\%\phi_t \tag{3.14a}$$

$$\phi_2^{\text{new}} = \frac{\phi_2}{1 - \phi_1} = \frac{30\%\phi_t}{1 - 20\%\phi_t} \tag{3.14b}$$

$$\phi_3^{\text{new}} = \frac{\phi_3}{1 - \phi_1 - \phi_2} = \frac{50\%\phi_t}{1 - 50\%\phi_t} \tag{3.14c}$$

In order to make sure that the generated porous space precisely fit the experimental data, the numerical assessment based on morpho-mathematical operations is presented below.

3 Verification of model

3.1 Morphological operations

The mathematical morphology provides a set of processing methods related to Minkowski addition for the analysis of geometrical structure, originally applied for binary image. A detailed presentation and application of this theory is in [Matheron, 1975][Serra, 1982][Serra, 1988][Dougherty, 1992][Soille, 2013][Glasbey and Horgan, 1995]. Generally speaking, the morphological operations transform the initial image into a new one through the interaction with the other image of certain shape and size, which is known as the structure element. The shape of the structuring element has very significant influence on the result of any morphological operation, and therefore, the choice of the shape and size is often made according to some prior knowledge of the image geometry. In general, the shape of structuring element ranges from fully arbitrary to classes with limited shape, resulting in a reduced complexity such as lines, circles, diamonds, and rectangles. There are no theoretical bounds or limitations on the choice of structuring element shape. However, for a better comparison result, it is suggested to use a shape that resembles the shape that is searched for or that is to be distinguished. In this study, the investigation of porous space is performed using octahedron as the form of structuring element.

Morphological operations can extract the image information, detect their shape characteristics and eliminate irrelevancies. The theoretical foundation of binary mathematical morphology is set theory. In binary images, those points in the set are called the foreground and those in the complement set are called the background. The two fundamental morphological operations are erosion and dilation. The erosion operation uniformly reduces the size of objects in relation to their background. The dilation operation is the inverse of the erosion operation, can uniformly expands the size of the objects.

In regards with the spatial structure of two phases: matrix and pores in the generated model, focus is then driven to the numerical implementation of two operations: morphological opening for the assessment of pore size distribution and geodesic reconstruction for the extraction of boundary-connected pores.

3.1.1 Erosion and dilation

Erosion is the process of eliminating all the boundary points from an object, leaving the object smaller in area by half width of the structuring element all around its boundary. Narrow parts which are less than structuring element would be removed, thus the initial object will be divided into several small parts. Through variation of the size of structuring element, erosion can progressively remove segmented image objects that are too small to be of interest. This process is illustrated in Figure 3.9, Figure 3.9(b) and Figure 3.9(c) are the resulting eroded image considering different sizes of structuring element. Let M be an initial image, E a structuring element and z coordinate of pixels in transformed image, erosion can be computed as:

$$\text{Erosion} : M \ominus E = \{z \mid E_z \subseteq M\} \tag{3.15}$$

The origin of E is placed at z and is completely contained within M. The structuring element E may be regarded as a probe which slides across the image M, testing the spatial nature of M at each pixel.

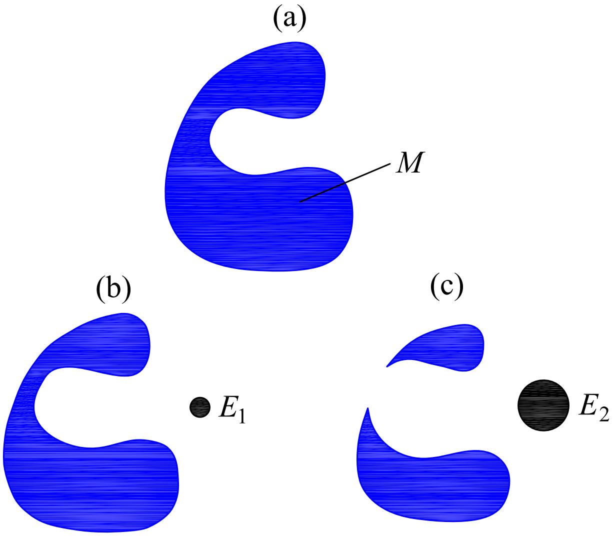

Figure 3.9: Illustration erosion with different structuring elements, (a), initial image, (b), erosion with small structuring element, (c), erosion with large structuring element (adapted from [Hosseini, 2015], Morpho-mathematical operations).

In contrast, dilation is the process of gradually enlarging the boundaries of regions of foreground pixels. If the object is circular, its diameter increases by half width of the structuring element with each dilation. Two separated objects may be connected through the dilation process. Through variation of the size of structuring element, dilation can progressively incorporate background pixels into it then provides larger object. This process is illustrated in Figure 3.10, Figure 3.10(b) and Figure 3.10(c) are the resulting dilated image considering different sizes of structuring element. Dilation can be given as:

$$\text{Dilation} : M \oplus E = \{z \mid E_z^s \cap M \neq \varnothing\} \tag{3.16}$$

E^s is equal to the geometric reflection of E around the origin. Dilation of M by E is a set that contains elements z such that the intersection between the M and E when translated by z is not an empty set.

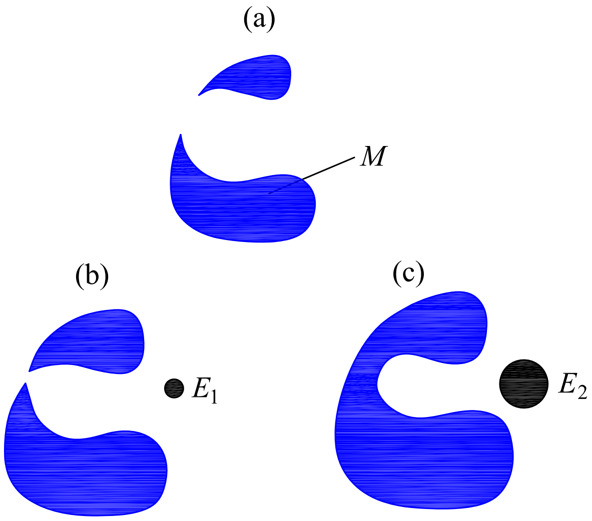

Figure 3.10: Illustration dilation with different structuring elements, (a), initial image, (b), dilation with small structuring element, (c), dilation with large structuring element (adapted from [Hosseini, 2015], Morpho-mathematical operations).

3.1.2 Morphological opening

When combining erosion and dilation, one followed by the other using the same structuring element, it is possible to form other important morphological operations such as opening and closing. Opening is an erosion followed by a dilation and closing is a dilation followed by an erosion. An opening of M by E is defined as:

$$\text{Morphologicalopening} : M \circ E = (M \ominus E) \oplus E \tag{3.17}$$

The opening operation is applied to search specific shapes and eliminate small and thin objects (smaller than structuring element), break objects at thin parts, and generally smooth the boundaries of larger objects without significantly changing their area. The

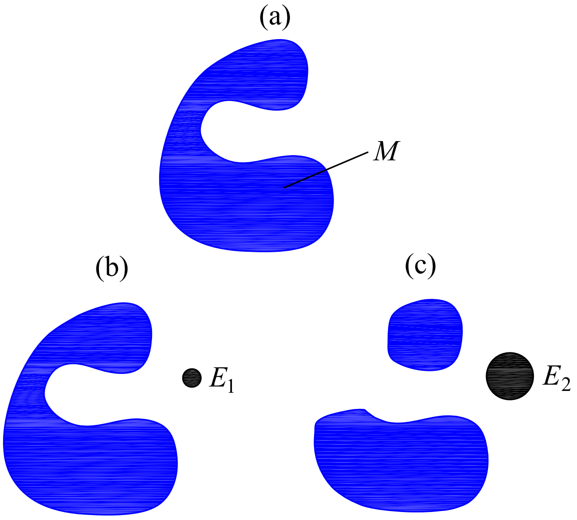

Figure 3.11: Illustration morphological opening with different structuring elements, (a), initial image, (b), opening with small structuring element, (c), opening with large structuring element (adapted from [Hosseini, 2015], Morpho-mathematical operations).

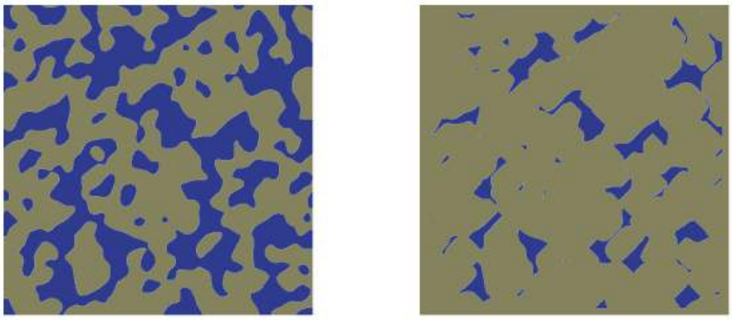

(a) Initial image. (b) Erosion on initial image.

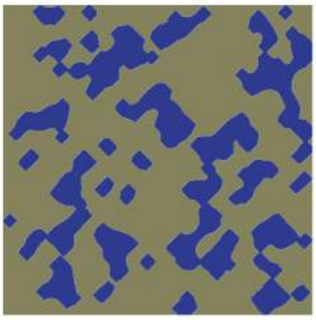

(c) Dilation on eroded image.

Figure 3.12: Illustration of the process of morphological opening.

essential idea for this operation is that erosion removes small features in the initial image that can not be recovered by the following dilation. At the mean time, big objects shrunk by the erosion are dilated back after the dilation process without changing their area. The effect is the elimination of small features and the conservation of the interested objects. This operation is shown in Figure 3.11 considering different structuring element sizes.

Thanks to this principle, a defined size of structuring element can be associated with pore size and then morphological opening can gradually remove small pores from the porous space. A 2D example of porous medium is illustrated in Figure 3.12, the initial pore space Figure 3.12(a) is firstly transformed by erosion (see Figure 3.12(b)) which shrinks the foreground pixel area, and then the dilation (see Figure 3.12(c)) will reconstruct the conserved parts. Just as the sieving process of granulometry performs through a series of sieves for a set of particles. Each sieve possesses a characteristic hole size which plays the same role as structuring element in morphological opening. Hence, measures of cumulative porosity are predictable and a more qualitative analysis of pore volume increments is then feasible.

3.1.3 Geodesic reconstruction

Another extremely useful image analysis operation called geodesic reconstruction is implemented here. Geodesic reconstruction is a morphological transformation involving two images and a structuring element. One image, the marker, is the starting part for the operation. The other image, the mask, constrains the transformation. The structuring element used defines connectivity. In the binary case, reconstruction simply extracts the connected components of the mask which are marked by a marker contained in the mask [Vincent, 1993][Ronse, 2008]. This process is illustrated in Figure 3.13.

The process of geodesic reconstruction consists iterations of geodesic dilation on marker in mask and then extracts the connected components in mask from marker. It is computed as:

$$R_X(Y) = \bigcup_{Y \cap X_k \neq 0} X_k = \bigcup_{n \geqslant 1} \delta_X^{(n)}(Y) \tag{3.18}$$

where $R_X(Y)$ represents the resulting geodesic reconstruction which consists of connected components $(X_1, X_2 ... X_k)$ of mask X that contains at least a pixel of marker Y and obtained by the geodesic dilation $\delta_X^{(n)}(Y)$ of a given size n. The elementary geodesic dilation can be defined as a dilation of marker with a given size (half width of the structuring

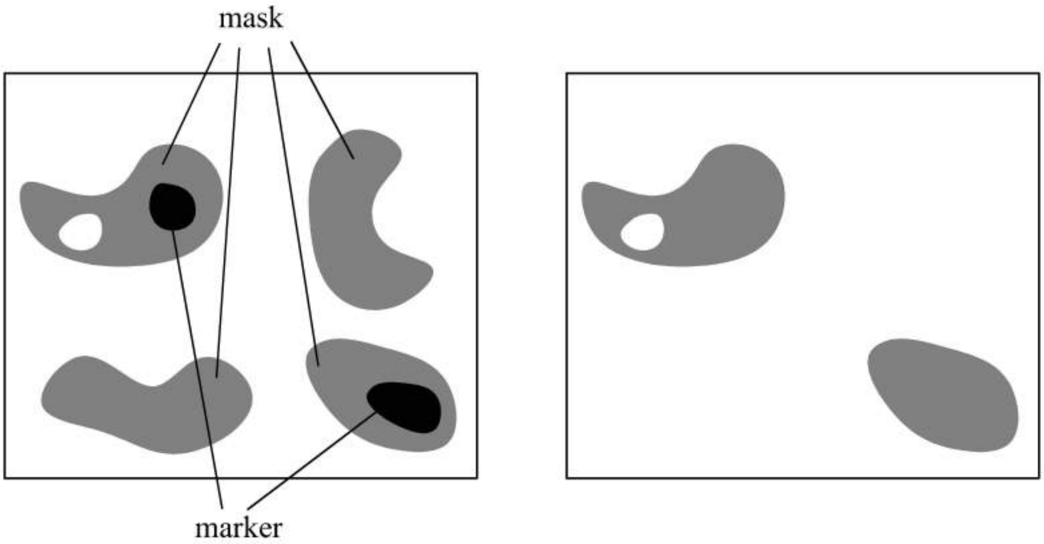

Figure 3.13: Binary reconstruction from markers.

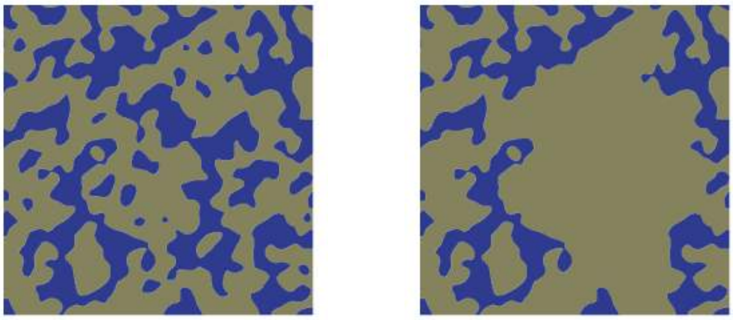

(a) Initial image.

(b) Geodesic reconstruction from edges.

Figure 3.14: Illustration of the application of geodesic reconstruction to find open porosity.

element) then followed by a boolean intersection with mask. It can be computed as:

$$\delta_X^{(1)}(Y) = (Y \oplus E) \cap X \tag{3.19}$$

Another important notion called geodesic distance is explained as: giving a set as the mask, the geodesic distance between two pixels A and B is the length of the shortest paths joining A and B which are included in mask. More importantly, the geodesic distance between two pixels within a mask is highly dependent on the type of connectivity between them. This notion will be repeated in the following chapter and applied for the characterization of gas migration pathways. In regards with the porous structure, the application is to consider the boundary-touched pores (open porosity) as the marker and the entire pore network as the mask, then the opening porosity will be finally conserved after geodesic reconstruction. This principle is depicted in Figure 3.14.

3.2 Construction of 3D model

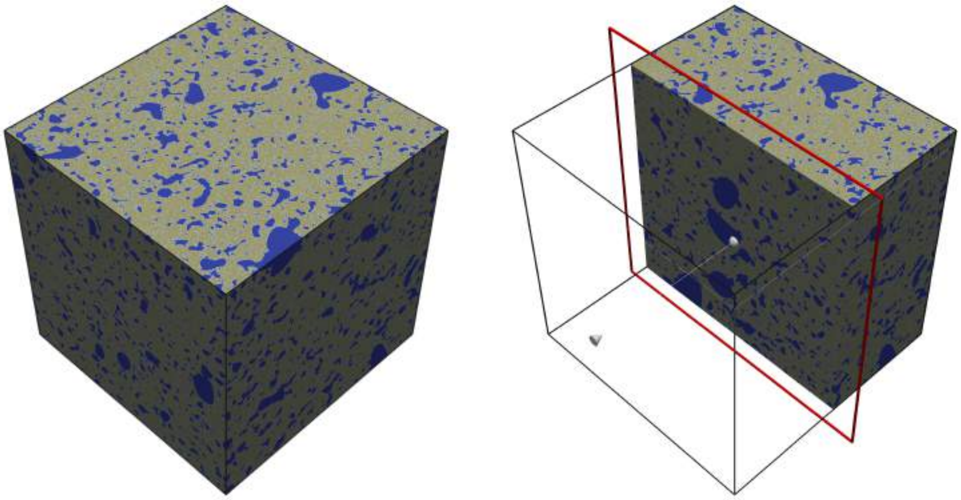

Figure 3.15: Realization of porous space using data from WA method (union of 10 independent excursions).

As explicated for Figure 2.3, since pore space characteristics are the key parameters for fluid movement, several COx argillite models are generated based on a same total porosity and pore volume evolutions from Figure 2.3 (Model 1 from WA, Model 2 from NMR, Model 3 from MIP) in order to investigate the possible divergences in the simulated gas migration properties. Excursions with same mesh of 800×800×800 points are computed in a cubic domain of 5 μm thus capable of involving the major proportion of pores (6.25 nm - 1 μm). It is plausible that pores larger than 1 μm and smaller than 6.25 nm are not taken into account since the former show a relatively low percentage and the latter hardly play roles in breakthrough process due to their high capillary resistances. Along this line of thought, the defined voxel size is sufficient for the following prediction of gas transport and meanwhile possesses relatively shorter calculation time and lower data storage. As mentioned before, the correlation length of excursion is taken to be the average diameter of pores distributed in a limited size range. The COx argillite model is generated through an union of 10 excursions with correlation lengths of: 0.9 μm, 0.7 μm, 0.5 μm, 0.3 μm, 0.1 μm, 0.08 μm, 0.05 μm, 0.03 μm, 0.015 μm and 0.008 μm. The volume fraction of each

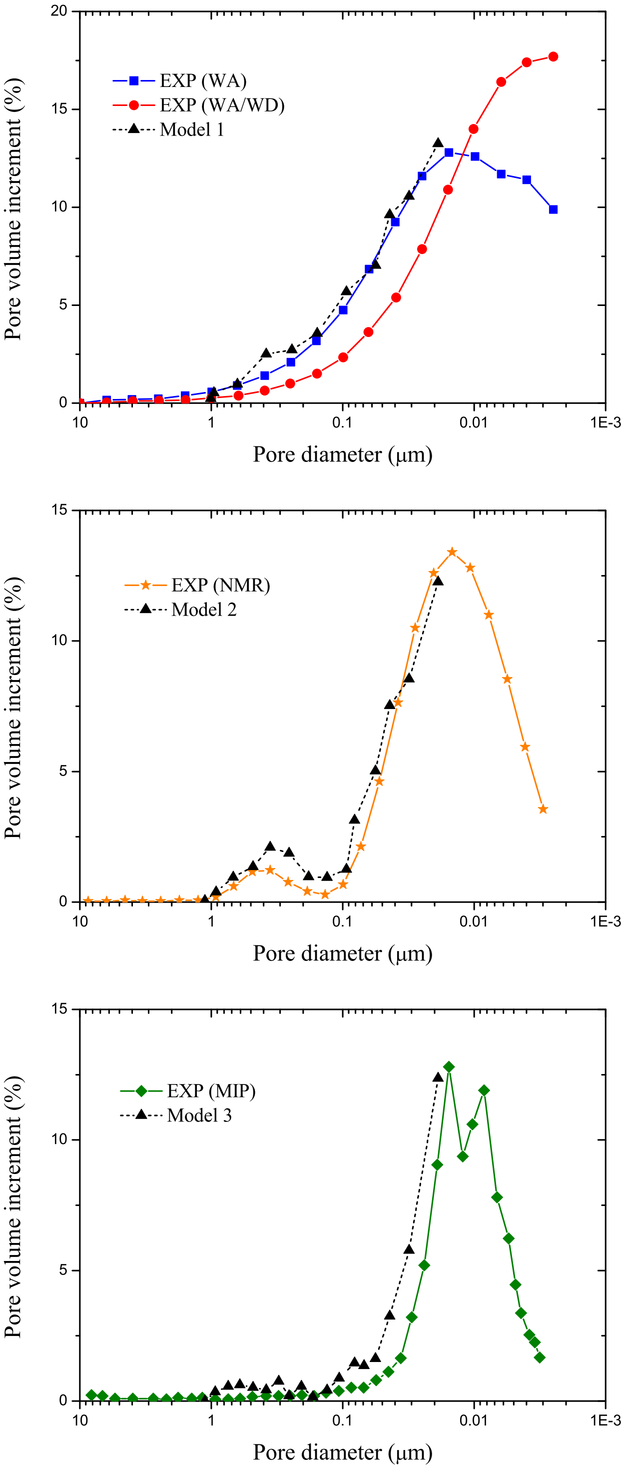

Figure 3.16: Numerical and experimental pore distribution in three generated argillite models.

excursion has been modified several times to show better accordance with the experimental trends. A realization from WA data is presented in Figure 3.15 with pores in blue and matrix in grey.

For a more qualitative analysis, geodesic reconstruction is firstly implemented for the purpose of 1. Verification of open porosity through comparison with the experimental value, 2. Extraction of open pores as initial image for later morphological opening analysis. The input total porosity for simulation is defined as 25%. The resulting morphologies show that the output porosities for these three models are 25.62%, 25.53%, 26.18%, respectively. The investigation of geodesic reconstruction provide open porosities as 21.21%, 20.84%, 20.53%, respectively. Values are located in the acceptable range of 14 - 22%. Following this, a sequence of morphological opening is realized with increasing size of the structuring element. It should be noted that the diameter of the smallest structuring element of octahedron is necessarily composed of three pixels. In other words, pores smaller than 18.75 nm could not be filtered and neither be represented on pore size distribution curve. Moreover, pore volume increment depends on the chosen diameter range. In order to perform an accurate and easy comparison with the same calibration, sizes of the using structuring element are set as closed as possible to the characteristic diameters presented in experimental curves. As shown in Figure 3.16(a)(c), pore size distributions in Model 1 and Model 3 span from 18.75 nm to 1 µm with similar increments to experimental curves and peak sizes at 18.75 nm. In Model 2 (Figure 3.16(b)), besides the terminal peak size, the bell-shaped evolution between 100 nm - 1 µm and another peak size centred around 500 nm are clearly produced. Even though union of excursions provides a pore space model well-fitted with the experimental pore size distribution, the lack of capacity for the representation of natural rock properties such as the bedding plane, may influence the accuracy of simulation results. Hence, a real model of sample comprising the major pore size range and derived from direct imaging techniques is always a privileged choice.

4 Conclusions

In this chapter, the generation of porous space morphology is performed through the excursion set of correlated Gaussian Random Field. This thresholding process transforms a continuous field to a binary one, thus is suitable to represent pores and matrix in a porous medium. Since the morphological aspects are totally determined by the threshold t and correlation length L_c, playing with all these parameters gives a wild range of morphologies. The geometrical and topological properties of excursion such as volume, surface, Euler characteristic are under statistical control and directly linked with the probabilistic properties and the threshold t. Considering the application of excursion set for the reconstruction of an accurate morphological model with numerical pore size distributions fit the experimental values, union theory is then implemented to yield a single excursion with several correlation lengths.

The investigation and verification of generated model is conducted by morpho-mathematical operations. Among them, morphological opening can gradually remove small objects (smaller than structuring element) from the initial image thus is applied to filter the porous space. Another method called geodesic reconstruction, is performed through an iteration of "geodesic dilation + intersection" and is to conserve connected components from marker in mask. This idea is implemented for the extraction of open porosity which plays the key role in fluid migrations.

Ultimately, thanks to these basic methods, argillite models are constructed with consideration of three experimental pore size distributions. Due to sample preparations and measuring techniques, differences among these distribution are supposed to be reasonable. Subsequently, the three models are produced by comparing the pore size distribution and open porosity.

In the next chapter, these morphological models would be used for the prediction of gas migration properties.

Chapter 4

Numerical estimation of gas breakthrough pressure

Contents

1 Introduction

Gas migration through low-permeable rock formation principally follow four mechanisms, concluded in [Marschall et al., 2005]. The first one is the advective and diffusive transport of dissolved gas in porewater. This transport mode starts from the application of gas pressure but the efficiency is restricted by the low hydraulic conductivity of the studied rock and by the low dissolution and diffusion efficiencies. The second transport mechanism is the two-phase flow which corresponds to porewater displacement under gas pressure and capillary force. Afterwards, if gas pressure exceeds the minor principal stress acting on the rock mass, additional pathways would develop across the porous medium then leads to micro-fractures. Finally, if the fracture threshold is exceeded, macro-fracture will initiate and gas phase will present in it. Additionally, a re-imbibition process after breakthrough which is due to reduction of gas pressure is also very interesting to be considered. In this part, focus is principally drawn to the capillary two-phase flow mechanism.

The capillary sealing efficiency is described as the capacity for the non-wetting phase (gas phase) invasion and the corresponding wetting phase (water phase) displacement in an initially completely saturated porous medium. In particular, several characteristic gas pressures have been observed and denoted during different experimental procedures. In [Thomas et al., 1968], a threshold pressure is defined which is referred as the applied gas pressure required to overcome capillary resistance to initial gas penetration and to the development of interconnected gas pathways that would allow outward gas flow. Porous space in natural materials is extremely complex with randomly shaped and positioned pores. In general, non-wetting phase invasion is supposed to firstly happen in large pores with small capillary resistances, then successively take place in small pores with increasing gas pressure. Threshold pressure has been defined following two assumptions. The first definition is associated with the earliest penetration of gas phase into the largest pores near the surface of the porous medium. In this case, threshold pressure is equal to the capillary pressure at a fully water saturated state. The second one corresponds to the formation of a continuous flow path across the pore network. In other words, water saturation is lower than 1.0 and can be called as the critical gas saturation. The relative permeability to the gas phase begins to rise from its zero value. The two definitions and their relationships between capillary pressure and relative permeability is illustrated in Figure 4.1. In [Schowalter, 1979], the minimum applied gas injection pressure which is related to the formation of a connected hydrocarbon filament through the largest interconnected water-saturated pore throats of the rock is defined as the displacement or breakthrough pressure. In [Pusch et al., 1985], the hypothesis of the critical pressure

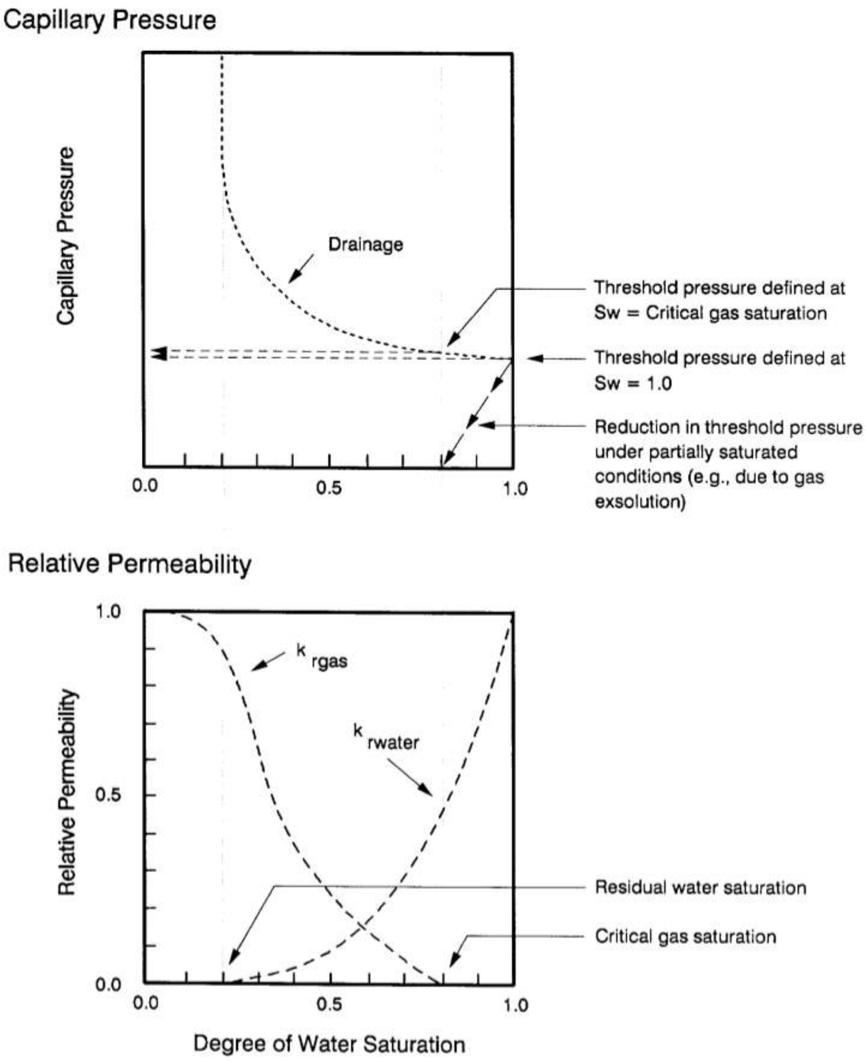

Figure 4.1: Definitions of threshold pressure and relationships with capillary pressure and relative permeability, from [Thomas et al., 1968].

concept is proposed by measuring the gas flow as a function of the applied, successively increased gas pressure. During the gas pressure increasing and maintaining cycle, critical pressures are manifested by a suddenly appearing gas bubble release through the outlet tubing. In [Gallé and Tanai, 1998] and [Gallé, 2000], two kinds of threshold pressures are reported during laboratory experiments, the first called “pore entry pressure” is defined over which a significant gas flow is measured at the downstream side of sample, the second which leads to sharply increasing gas flow rate is called “breakthrough pressure”. The second is normally higher than the first. For fully saturated samples, these two thresholds are very close. In [Horseman et al., 1999], breakthrough pressure is defined as the excess pressure at which leakage happens by a sudden gas outflow at the downstream side. In [Hildenbrand et al., 2002b][Hildenbrand et al., 2002a][Hildenbrand et al., 2004], gas breakthrough experiment is not following common protocol by stepwise pressure increase by gas, but by applying directly a high gas pressure gradient (higher than the expected breakthrough pressure). After the breakthrough and the water re-imbibition processes, a complete pressure equilibration between the two chambers is not reached, but a residual pressure difference persists which is a characteristic parameter for the rock sample, called as the minimum displacement pressure and can be used to evaluate the capillary sealing efficiency.

In this chapter, gas breakthrough is supposed to require that outward flowing gas penetrate and establish a gas-filled network of flow paths in the sample. Therefore, the gas breakthrough pressure is associated with the incipient formation of a continuous network of gas flow paths. Two-phase flow is governed by the difference between gas pressure and capillary pressure. According to Young-Laplace law, for an ideal cylindrical pore totally saturated by water, the minimum applied gas pressure $\triangle P$ for porewater displacement is determined by the surface tension γ, the wetting angle θ of fluids and the radius r of pore and is given as:

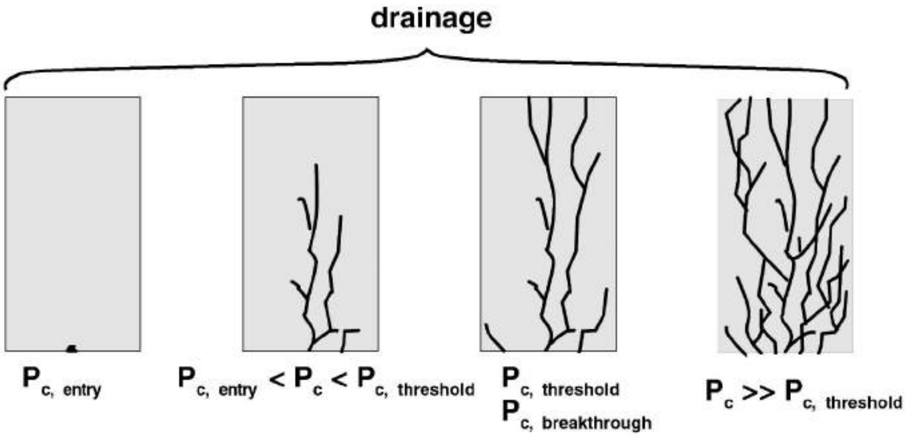

Figure 4.2: Stages of gas breakthrough process [Hildenbrand et al., 2002b].

$$\triangle P = \frac{2\gamma\cos\theta}{r} \tag{4.1}$$

As introduced in [Hildenbrand et al., 2002b], gas breakthrough process includes the creation and propagation of preferential pathways through porous network. These preferential pathways involve interconnected pores within the largest pore throat, characterized by effective pore radius (r_{eff})and the corresponding least capillary resistance to be overcome. The breakthrough pressure is then defined as the threshold pressure for the total drainage in preferential pathways between the upstream side and the downstream side of sample. When the breakthrough pressure is reached, a continuous gas flow will form into the porous space. Thus breakthrough pathways could be simply defined as:

$$\mathcal{P}_b = \max_x\{\min[r_i(x)]\} \tag{4.2a}$$

$$\min[r_i(x)] = r_{\text{eff}} \tag{4.2b}$$

where x stands for different interconnected pore, i represents the spatial position along the path, r is the radius of the circular cross-section of pore.

Before the breakthrough, gas entry pressure P_e must firstly be reached at which the gas phase actually invades the porous material and drainage process from complete saturation starts [Coussy, 2004]. After the breakthrough, with a continuously increasing gas pressure, additional connected pores would participate in the network of pathway and consequently increase the gas phase permeability. Ultimately, water saturation degree of sample is down to a value called Irreducible Water Saturation (IRWS) which means water in boundary-connected pores is totally drained. At this moment, gas permeability reaches its maximum value. These different stages are illustrated in Figure 4.2.

Based on this scenario, numerical approach is based on the generated model of the porous network. The extraction of gas breakthrough pathways and the following topological analysis are performed by using morpho-mathematical methods introduced in the previous chapters. The estimation of gas breakthrough pressure is associated with the size of structuring element used in the procedure of morphological opening and calculated by Young-Laplace equation. The feasibility study is accomplished by comparing the simulated and the experimental values. Ultimately, study is extended to another potential host rocks in the context of radioactive waste storage.

2 Numerical methods and application to COx argillite

2.1 Numerical point of view

Based on the interpretation of the physical procedure which takes place in the porous network during breakthrough process, a simulation work using morphological model is performed by applying morpho-mathematical operations.

The first step is to extract interconnected pores between the upstream and the downstream sides. As illustrated in Figure 4.3, initial pore space image (see Figure 4.3(a)) is firstly subjected to geodesic reconstructions starting from the upstream side (see Figure 4.3(b)) and the downstream side (see Figure 4.3(c)). Following this, an intersection between these two obtained images is able to conserve interconnected pores (see Figure 4.3(d)).

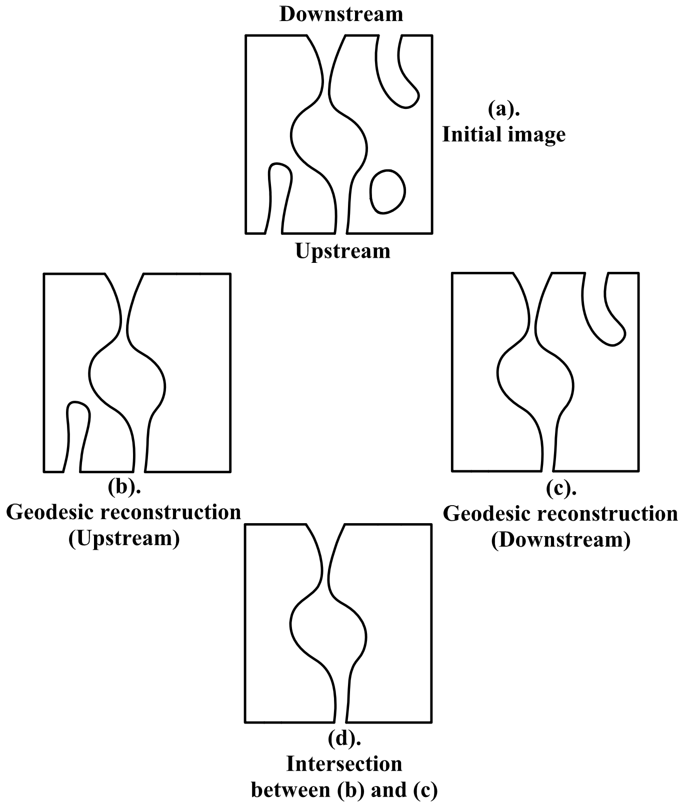

Figure 4.3: Proposed method to extract interconnected pores between the upstream and the downstream sides.

Let M be the initial image of porous space, M_0 be the interconnected pores between the two opposite sides, thus it can be defined as:

$$M_0 = R^{\oplus}(M) \cap R^{\ominus}(M) \neq 0 \tag{4.3}$$

When a gas pressure is applied, drainage can only occur in pores with sizes equal or exceed the Young-Laplace radius and necessarily connect to the upstream side. In view of this, two operations are implemented and shown in Figure 4.4. The first is a filtering process realized by morphological opening (see Figure 4.4(a)) to detect and conserve pores larger than a certain size that allow gas entry. Subsequently, the drained porosity is calculated by geodesic reconstruction beginning with the upstream side of the obtained model from morphological opening (see Figure 4.4(b)). The prediction of gas entry pressure is performed through this process by comparing the increments of drained porosity. If the geodesic reconstruction ends at the downstream side, it means that continuous gas flow forms across the pore system and gas breakthrough is realized. At the first appearance of breakthrough pathways, the size of structuring element used for morphological opening determines the breakthrough pressure.

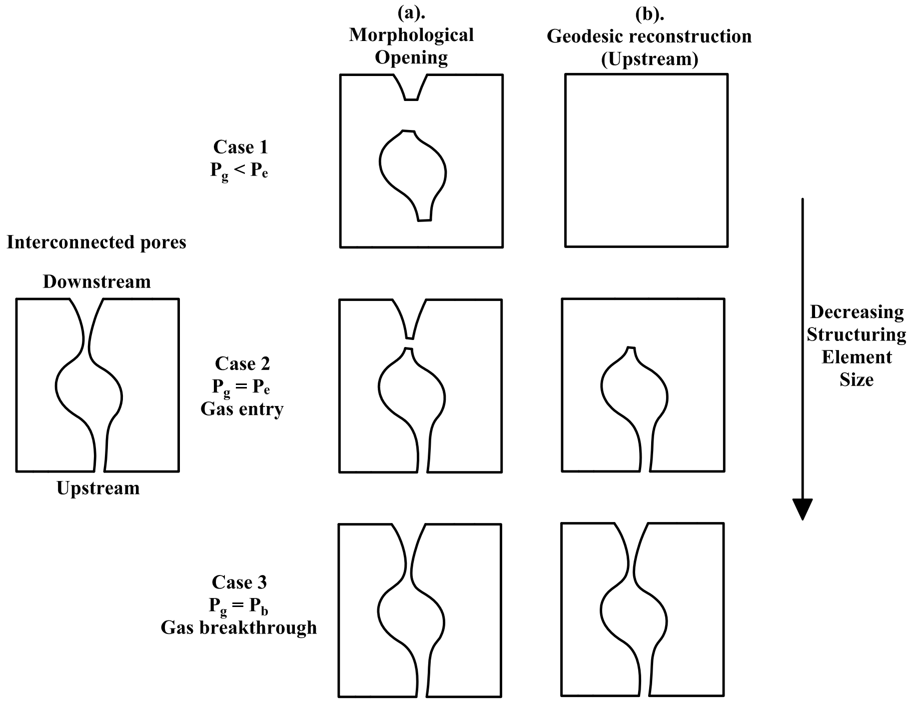

Figure 4.4: Proposed method to determine gas entry pressure, gas breakthrough pressure and to select gas migration pathways.

Let E_i be the structuring element with variable size, expectations of gas migration pathways $\mathcal{P}_i$ and corresponding gas pressure P_i could be computed as follows:

$$\mathcal{P}_i = R^{\oplus}(M_0 \circ E_i) \tag{4.4a}$$

$$P_i = \frac{4\gamma\cos\theta}{d(E_i)} \tag{4.4b}$$

2.2 Application to COx argillite

Pore space is assumed to be totally saturated at the onset. Temperature is fixed at 25 ℃, thus leads to surface tension γ of 0.072 N/m [Vargaftik et al., 1983]. Wetting angle θ equals to 0 for the hypothesis of complete wetting of media in presence of gas [Andra, 2009a][Yuan and Lee, 2013].

The numerical predictions of gas entry and gas breakthrough pressure are performed in the three models (generated in chapter 3) in order to draw conclusions about how the different measuring pore size distributions control gas migration and which model shows a better agreement with experimental values. As mentioned before, in Model 1, higher proportion of large pores (> 100 nm) is ensured with respect to data from WA test. Whereas Model 3 from MIP is more sensitive to small pores (< 30 nm). NMR method gives Model 2 a comparatively higher proportion in medium pores (30 nm - 100 nm).

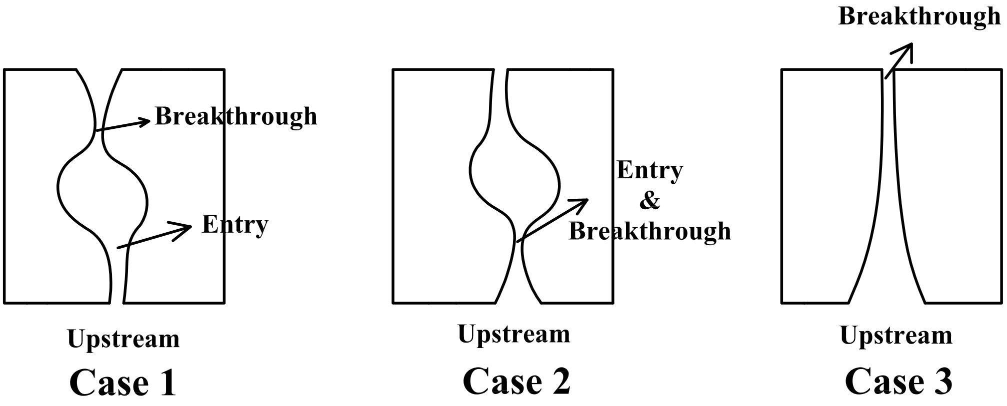

Figure 4.5: Proposed three cases of the spatial position of the entry pore throat.

Considering different boundary-touched pores on different faces of cube, for one model, investigations of gas entry pressure are performed respectively for the six positive and negative directions along x, y, z axis; estimations of gas breakthrough pressure are performed in three axial orientations. The drained porosity as a function of gas pressure is plotted in Figure 4.6 for Model 1, Figure 4.8 for Model 2 and Figure 4.9 for Model 3. Apparently, increasing gas pressure leads to progressive reduction of water saturation. The increment of drained porosity is essentially controlled by the so called "pore throat" which is referred to as the narrowest part along the connected pathways. In a randomly distributed porous space, the spatial position of pore throat predominantly influences the drained porosity. For the prediction of gas entry pressure, three cases are proposed (see Figure 4.5): Case 1, The gas invasion may firstly traverse a large pore throat (larger than breakthrough pore throat) defined as the entry pore throat and instantaneously increase the drained porosity. Thus a corresponding gas entry pressure lower than the gas breakthrough pressure can be obtained. This case seems to be more consistent with some phenomenological observations ([Hildenbrand et al., 2002b][Hildenbrand et al., 2004]). In the simulation results, it appears in Z(+) direction of Model 1 with 2.72 MPa $< P_e <$ 3.06 MPa and in X(-) and Y(-) directions with 2.18 MPa $< P_e <$ 2.72 MPa; Z(+) direction of Model 2 with 3.06 MPa $< P_e <$ 3.51 MPa; Y(+) and Z(-) directions of Model 3 with 5.14 MPa $< P_e <$

6.55 MPa; Case 2, The breakthrough pore throat locates close to the upstream side and the interconnected porosity between them is limited at a low value. Hence, the drainage process will be significantly restricted until the excess of breakthrough threshold. Thus, the gas entry pressure equals to the gas breakthrough pressure. This case appears in all the other directions; Case 3, The drained porosity smoothly increases thus no obvious gas entry threshold can be observed. This case is not observed in the obtained results. It is plausible to consider that the irregularity of simulated gas entry pressure is solely due to the size of defined cubic model. In a small domain with size down to micron, the influence of spatial position of entry pore throat will be enlarged. In other words, for a macroscopic sample, gas entry is no longer controlled by the connected pores to a small microscopic domain of the upstream face. Various sorts of cases may be involved at the same time.

In contrast with the irregular simulated gas entry pressure which is highly dependent on the random location of pore throat, gas breakthrough pressures are remarkably close in three axis orientations. For Model 1, gas breakthrough pressure ranges between 5.14 MPa and 6.55 MPa. For Model 2, it is 5.14 - 9 MPa. For Model 3, it is up to 9 - 16 MPa. In relation with the spatial structure, this variation is attributed to the various pore size distributions. Indeed, for models with higher proportion of small pores, the size of breakthrough pore throat is bound to be smaller thus leads to higher breakthrough pressure. An example with gas entry and gas breakthrough phenomenons is given in Figure 4.7.

More importantly, since the generation of Random Field is a stochastic process, its naturally spatially varying property influences the excursion set thus leads to randomly shaped porous network. In other words, excursion process with same parameters applied on different Random Fields with same probabilist properties can provide different morphological aspects. After the union of several excursions, difference will be significantly enlarged. In view of this, the 3D connectivity and the breakthrough pathway in random morphological models need be investigated and verified whether the corresponding breakthrough pressures could maintain at a relatively stable level. This step is considerably important for assessment of the proposed scenarios and methods. Figure 4.10 shows the results of numerical estimation of breakthrough pressure in one axis direction performed with 10 realizations for Model 1, Model 2 and Model 3. The black columns stand for the results of Model 1. The breakthrough pressure frequency indicates that six realizations provide results between 5.14 - 6.55 MPa, three in 4.24 - 5.14 MPa and one in 6.55 - 9 MPa. As depicted by the red columns for Model 2, five in 6.55 - 9 MPa, four in 5.14 - 6.55 MPa and one in 9 - 16 MPa. Results of Model 3 are presented by blue columns with

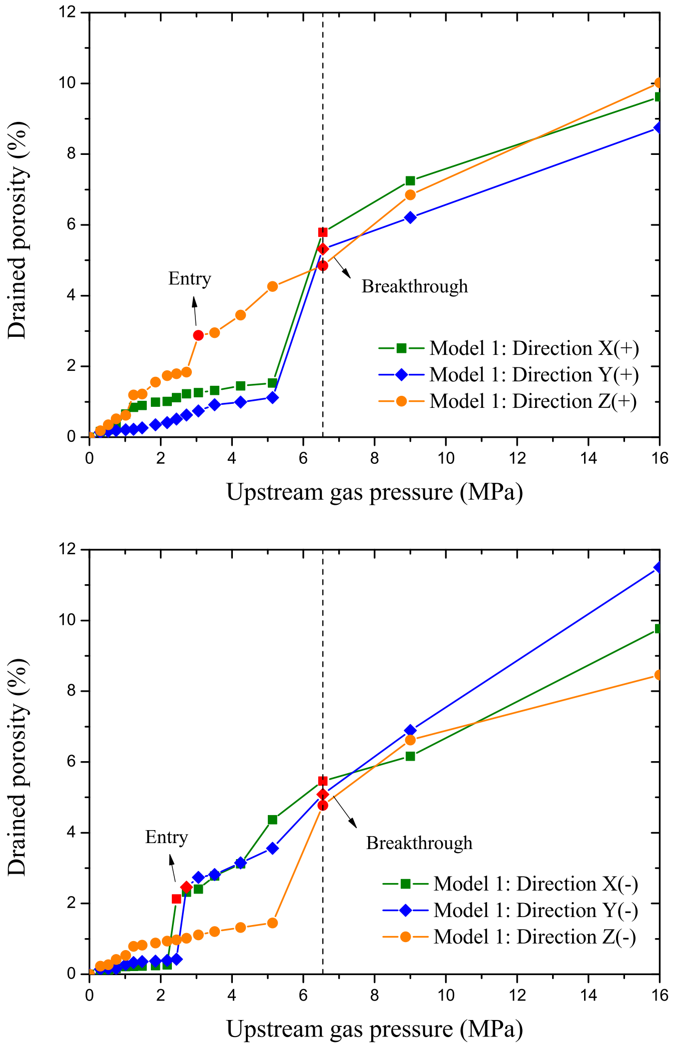

Figure 4.6: Simulation results of gas entry pressure and gas breakthrough pressure in positive and negative directions of three axis for Model 1.

a high frequency in 9 - 16 MPa (nine times) and only one time in 6.55 - 9 MPa. From these values, it can be concluded that 1. gas breakthrough pressures in porous networks with defined properties (porosity and pore size distribution) vary in a limited range, 2, by fixing the total porosity, porous space with larger average pore size provides higher gas breakthrough pressure. In regards with the gas entry pressure, since it highly depends on the morphological aspects, it can not always be estimated. As illustrated in Figure 4.11, from the obtained values, gas entry pressure increases in porous spaces with decreasing average pore size and show good accordance with expectations.

Various sorts of gas breakthrough experiments on COx argillite have been conducted

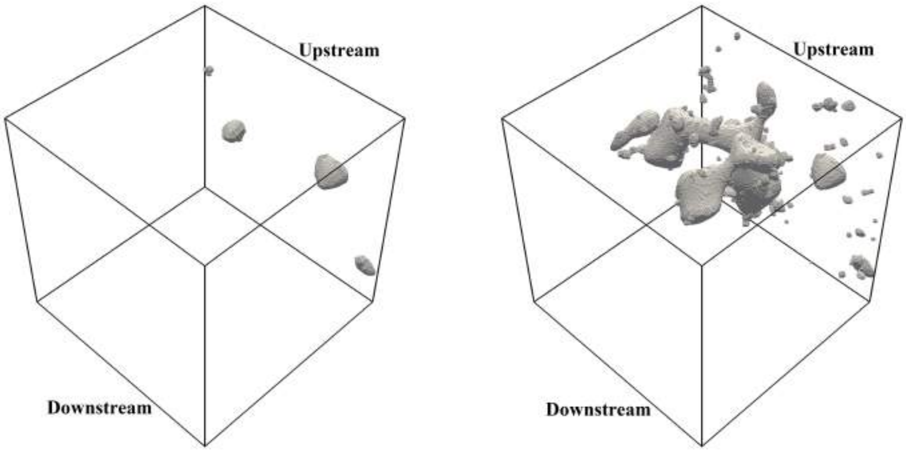

(a) $P_g = 0.75$ MPa. (b) $P_g = 2.44$ MPa, gas entry.

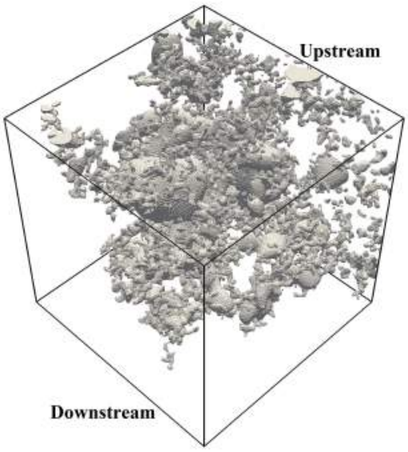

(c) $P_g = 6.55$ MPa, gas breakthrough.

Figure 4.7: Example of drainage process with increasing gas pressure (Model 1, negative direction of x axis).

with consideration of different feasibility. Different results have been discussed in chapter 2. For instance, gas entry pressure is estimated less than 3 MPa and gas breakthrough pressure is located between 4 - 5 MPa [Andra, 2009a]. Gas critical pressure is obtained as 3.4 - 5.3 MPa [Davy et al., 2009]. In regards with the numerical simulation results from Model 1 and Model 2, the gas entry pressure (Model 1: 2.18 - 3.06 MPa; Model 2: 2.72 - 4.24 MPa) and breakthrough pressure (Model 1: 4.24 - 6.55 MPa; Model 2: 5.14 - 9 MPa) show better accordance with experimental values. Thus enhances the idea: gas breakthrough is possible in low-permeable mudrocks at gas pressures much lower than confining pressure or fracture threshold [Hildenbrand et al., 2002b]. For Model 3, due to

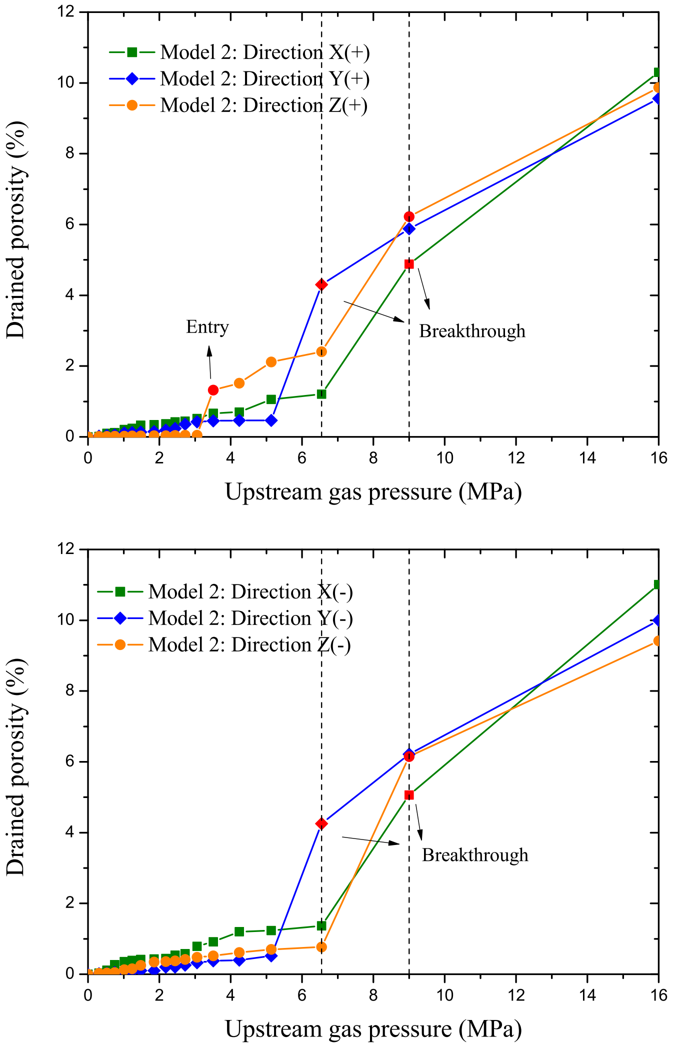

Figure 4.8: Simulation results of gas entry pressure and gas breakthrough pressure in positive and negative directions of three axis for Model 2.

the overestimation of the proportion of small pores, gas breakthrough pressure (9 - 16 MPa) is much higher and more likely exceeds the micro-crack threshold of 9 MPa and the fracture threshold about 12 MPa [Andra, 2005]. In this last case, stress - strain state analysis and damage model are necessarily involved to provide more accurate descriptions of gas movement.

3 Identification of gas pathways and estimation of tortuosity

Topological properties of breakthrough pathways such as geodesic distances and path tortuosities are also investigated. The morphological tortuosity of a pathway in porous

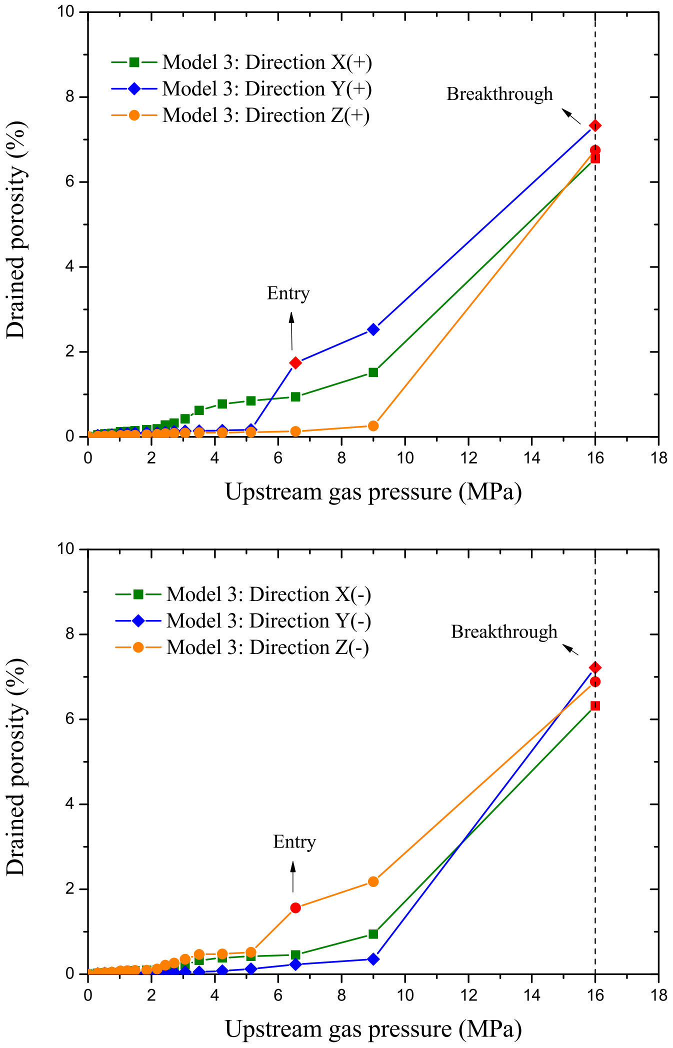

Figure 4.9: Simulation results of gas entry pressure and gas breakthrough pressure in positive and negative directions of three axis for Model 3.

space can be defined as the ratio between its geodesic length and the Euclidean distance between the upstream and downstream sides [Keller et al., 2011]. Simply speaking, geodesic distance counts the number of geodesic dilation steps that would be passed by carrying out geodesic reconstruction. The chosen size of the propagated structuring element is used to estimate the geodesic distance maps on a discrete grid. Moreover, each length of pathways is extracted from the downstream face. Table 4.1 lists the main results. The tortuosity of breakthrough pathways ranges between 1.5 - 4.13. An realization is presented in Figure 4.12. In particular, it is easy to find that some pathways with ends in lateral faces are also remained after geodesic reconstruction but they are not supposed to be able to play

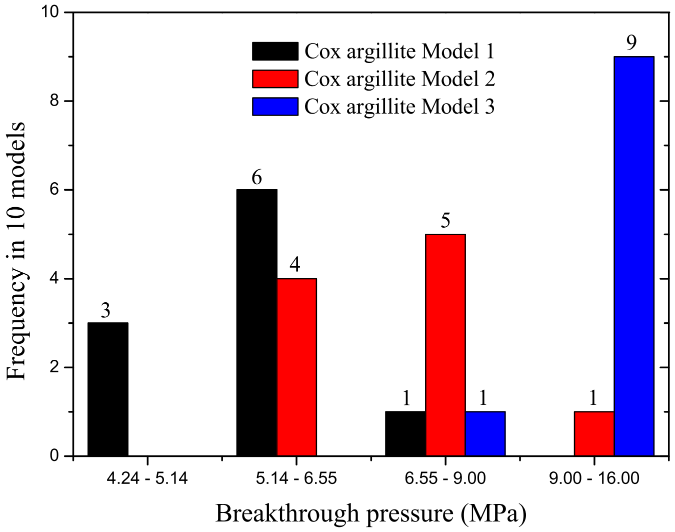

Figure 4.10: Numerical estimation of gas breakthrough pressure in COx argillite considering Model 1, Model 2 and Model 3 (results from 10 tests).

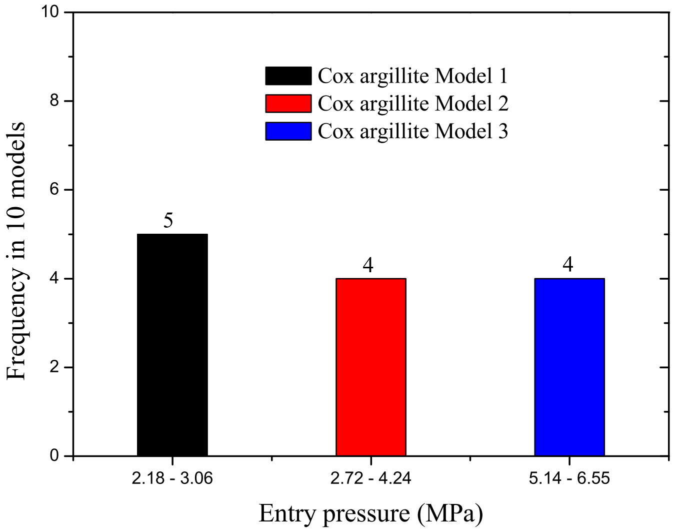

Figure 4.11: Numerical estimation of gas entry pressure in COx argillite considering Model 1, Model 2 and Model 3 (results from 10 tests).

roles in the gas breakthrough at the downstream side. This is solely due to the essential idea of intersection between two inverse reconstructions. Since geodesic reconstruction conserves connected components to the outset boundary but can not distinguish their propagation direction during the operation. If any branches of the opposite-sides connected pores connect to other sides, they could not vanish after the operation. In order to the represent the randomness and the complexity of gas migration pathways, another two

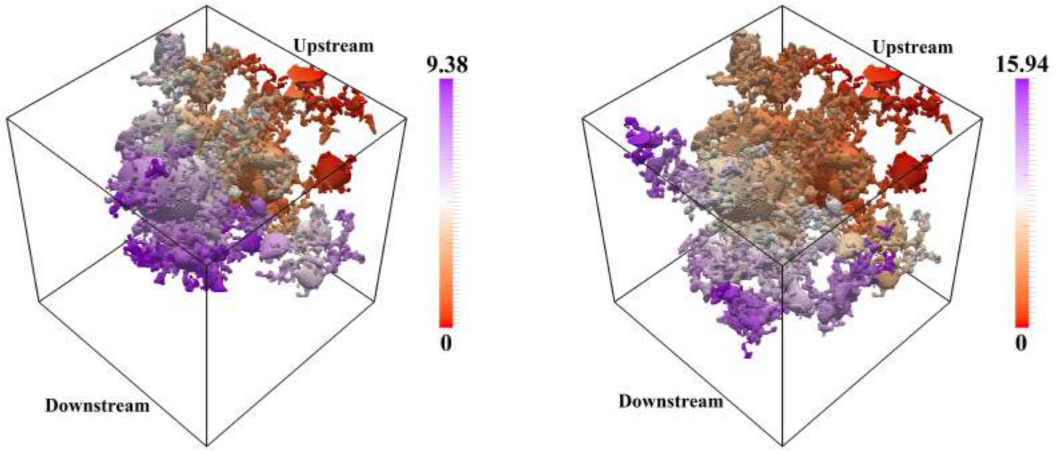

(a) The shortest length of 9.38 µm.

(b) The longest length of 15.94 µm.

Figure 4.12: Example of geodesic distances in breakthrough pathways (Model 1, $P_g =$ 6.55 MPa, negative direction of x axis).

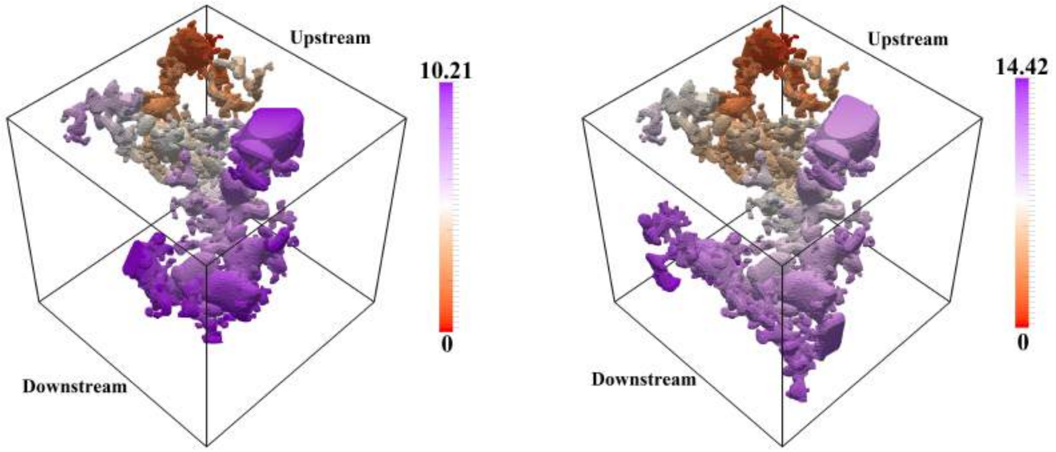

(a) The shortest length of 10.21 µm.

(b) The longest length of 14.42 µm.

Figure 4.13: Geodesic distances in breakthrough pathways for the second realization of porous space using the pore size distribution of Model 1.

realizations based on the pore size distribution of Model 1 are generated and their geodesic distances in breakthrough pathways are illustrated in Figure 4.13 and Figure 4.14.

Besides, in morphological model, even pore size distribution has been accurately represented but in comparison with a real sample, differences still exist. Indeed, argillite is a sedimentary indurated clay, composed of diagenetic bedding planes. In [Duveau et al., 2011], it has been proved that when gas injection is performed along the bedding planes,

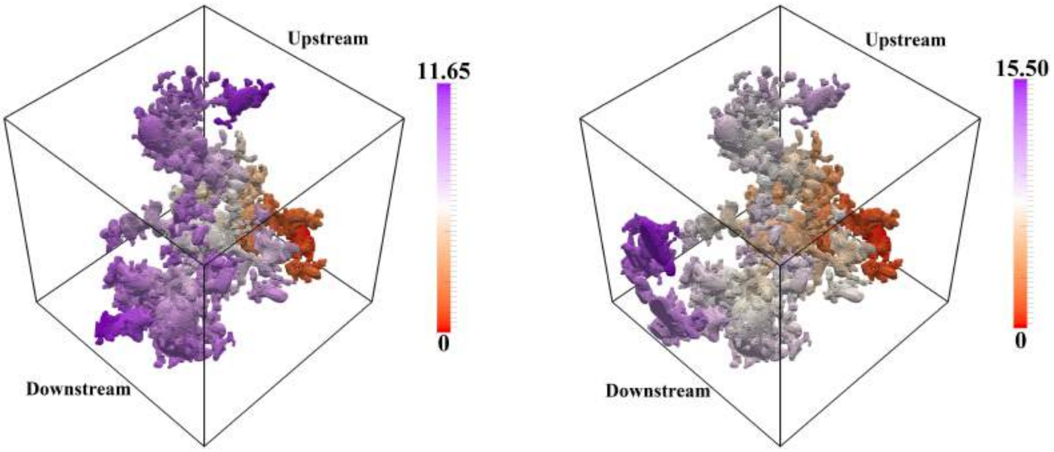

(a) The shortest length of 11.65 µm.

(b) The longest length of 15.50 µm.

Figure 4.14: Geodesic distances in breakthrough pathways for the third realization of porous space using the pore size distribution of Model 1.

Table 4.1: Prediction of gas entry pressure, gas breakthrough pressure and characteristics of breakthrough pathways.

Model	Entry pressure (MPa)	Breakthrough pressure (MPa)	Tortuosity of the shortest paths	Tortuosity of the longest paths
1	2.18 - 3.06	4.24 - 6.55	1.88	3.19
2	2.72 - 4.24	5.14 - 9	2.03	4.13
3	5.14 - 6.55	9 - 16	1.50	3.41

lower gas breakthrough pressure may be expected rather than when performing perpendicularly to the bedding planes. Tortuosity and path length are significantly smaller along the bedding plane direction when compared to all other possible directions [Song et al., 2015]. Due to the lack of capacity to represent the bedding plane using union of excursions, a real model of sample involving the major pore size range can be used for the future improvement of this study. Furthermore, the influences of temperature-depended surface tension and confining pressure could also been investigated.

4 Discussion about the influences of initial conditions

Furthermore, initial conditions such as the water surface tension and the confining pressure may influence the gas migration process. Gas phase movement depends on the difference between the applied gas pressure and the capillary force. According to Young-Laplace equation, for cylindrical pore, capillary force is determined by the surface tension, the wetting angle and the pore diameter. Based on a hypothesis of complete wetting, the wetting angle can be defined as 0. The surface tension is a temperature dependent parameter. For that reason, when a value is given for the surface tension of an interface, temperature must be explicitly stated. The general trend is that surface tension decreases with the increase of temperature, reaching a value of 0 at the critical temperature. In [Vargaftik et al., 1983], a recommended interpolating equation gives values of surface tension within the stated uncertainty:

$$\gamma = B\Big[\frac{T_c - T}{T}\Big]^{\mu}\Big[1 + b\Big(\frac{T_c - T}{T}\Big)\Big] \tag{4.5}$$

where γ stands for the surface tension, T denotes the absolute temperature, T_c is the reference temperature and is also defined as the critical point temperature with $T_c = 647.15$ K. B, b and μ are constants. $B = 235.8 \times 10^{-3}$ N/m, $b = -0.625$ and $\mu = 1.256$. This equation is valid between the triple point (0.01 ℃) and reference temperature T_c. Parts of values of surface tension (0.01 - 50 ℃) are presented in Table 4.2.

Table 4.2: Surface tension of water as a function of temperature [Vargaftik et al., 1983].

t (℃)	0.01	5	10	15	20	25	30	35	40	45	50
γ (10^{-3} N/m)	75.64	74.95	74.23	73.50	72.75	71.99	71.20	70.41	69.60	68.78	67.94

In the modelling work, same morphological information of porous space and same numerical methods are used to evaluate the relation between the breakthrough pressure and the temperature. When temperature is up to 50 ℃, surface tension decreases to 67.94×10^{-3} N/m thus leads to lower breakthrough pressures. On the contrary, if temperature drops to 5 ℃, surface tension increases to 74.95×10^{-3} N/m, then higher breakthrough pressures are obtained. Results are shown in Table 4.3.

In addition, the pore space volumetric strain which varies as a function of confining pressure and pore pressure according to an effective pressure law and its influence to the

Table 4.3: Simulated breakthrough pressure with different temperatures.

Model	P_b (T = 5 °C)	P_b (T = 25 °C)	P_b (T = 50 °C)
1	4.41 - 6.82	4.24 - 6.55	4 - 6.18
2	5.36 - 9.38	5.14 - 9	4.86 - 8.5
3	9.38 - 16.66	9 - 16	8.5 - 15.1

breakthrough process is an interesting issue. The earliest law which is based on scenario of identical variation in permeability due to confining pressure and pore pressure is know as Terzaghi's principle [Terzaghi, 1923]. It defined the effective stress P_{eff} as the difference between the confining pressure and the pore pressure. It is given as:

$$P_{\text{eff}} = P_{\text{conf}} - P_{\text{pore}} \tag{4.6}$$

where P_{conf} is the confining pressure and P_{pore} is the pore pressure. Some later experimental researches enhanced this law by adding another parameters [Kwon et al., 2001]. Porosity, pore space connectivity and pore size distribution are influential to the migration properties of rocks. A number of expressions have been evaluated for the effective pressure of a porous, fluid-saturated solid undergoing elastic deformation [Biot, 1941][Biot and Willis, 1957][Skempton, 1984][Nur and Byerlee, 1971]. Volumetric strain of porous rocks is controlled by effective pressures. The relation can be computed in macroscopic terms as:

$$P_{\text{eff}} = P_{\text{conf}} - (1 - K/K_s)P_{\text{pore}} \tag{4.7}$$

K is the bulk modulus of the rock without a pore fluid and K_s is the intrinsic bulk modulus without any pores. In consideration with the pore volume, the law can be expressed as:

$$P_{\text{eff}} = P_{\text{conf}} - [1 - \phi K/(K_s - K)]P_{\text{pore}} \tag{4.8}$$

where ϕ is the porosity [Robin, 1973]. In general, effective pressure law has a simple form as:

$$P_{\text{eff}} = P_{\text{conf}} - \chi P_{\text{pore}} \tag{4.9}$$

χ values which stand for the effective stress coefficient are determined for volumetric compaction, porosity, elasticity, and permeability and measured poroelastic response. χ

varies for different materials. As presented in [Gensterblum et al., 2015], for single-phase aggregates, such as clay-rich shales, mudstones, and calcite, χ generally takes values in $\chi \leqslant 1$. Transport properties are more sensitive to changes in pore pressure than to changes in confining pressure. If the pores of a porous medium with high compressive strength, such as pure quartz, sandstone, or carbonates, are lined with clay, χ values could be greater than 1 [Berryman, 1992][Biot, 1941][Zoback and Byerlee, 1975]. Due to various interacting effects, χ is more likely to be non-linear and be a function of pore pressure and confining pressure [Bernabe, 1987][Gangi, 1978][Li et al., 2009].

In this work, gas migration properties are obtained by morpho-mathematical operations. The estimation of breakthrough pressure is based on data from image analysis without consideration of porous stress-strain model. In view of this, the investigation of the influences due to pore pressure and confining pressure is relatively difficult. An initial idea has been proposed that by applying an erosion on pore space with a defined structuring element, the resulting shrinkage leads to a new porosity. Assuming that the volumetric strain is completely due to the pore space reduction and the volumetric strain can be expressed as a function of a linear combination of pore and confining pressures [Nur and Byerlee, 1971]. It is given as:

$$e = \frac{1}{K}P_{\text{conf}} - \frac{1}{H}P_{\text{pore}} = \frac{1}{K}(P_{\text{conf}} - \alpha P_{\text{pore}}) \tag{4.10}$$

where e stands for the volumetric strain and the effective modulus H is introduced by Biot [Biot, 1941]. K and H are themselves defined in accordance with laboratory test. The volumetric strain will increase with confining pressure and decrease with pore pressure. Hence, after the performance of a sequence of erosion with increasing size of the structuring element and a following extraction of gas transfer pathways, the relation between the gas breakthrough pressure and the pore / confining pressures can be obtained. However, as illustrated in Figure 4.15, since the porous network transformed by erosion is subsequently subjected to an identical shrinkage for the whole space, initial pore sizes no longer play roles in the resulting state. In fact, small pores trend to be more incompressible than large pores. Hence, simulation results could only indicate an increase of gas breakthrough pressure with the increase of confining pressure but could not provide accurate values. More specifically, limited by the mesh density of 800 × 800 × 800, the smallest structuring element is derived as 18.75 nm. This is due to that, after the smallest erosion, apart from the shrinkage of large pores (larger than 18.75 nm), small pores would disappear. Since the eliminated part represents about 50% of the total porosity, this transformation brings a extremely high volume reduction which is inaccurate to relate with a confining pressure. Even if the eroded pore throat provides a higher breakthrough pressure, the corresponding

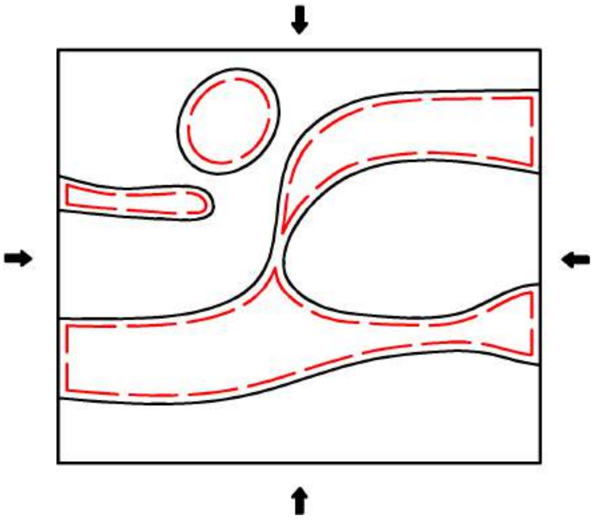

Figure 4.15: Proposed method to evaluate the volume strain using erosion.

stress state remains unknown.

In this regard, a reliable stress - strain model is necessarily involved to study the variation of breakthrough with changes in pore pressure and confining pressure. Due to the randomly shaped and located pores, this amelioration will be very challenging.

5 Application to another porous media

5.1 Opalinus clay

In Switzerland, the Mont Terri Rock Laboratory investigates the Opalinus Clay as a possible host rock for long-term geological disposal of radioactive waste [Bossart and Thury, 2007]. The Opalinus Clay formation is a fine-grained sedimentary rock, deposited 180 Ma ago in a shallow sea and compacted to a low porosity and low anisotropic permeability [Nagra, 2002]. On the regional scale the lateral variability of facies and lithology is low [Nagra, 2002]. The Opalinus clay can be subdivided into three main facies [Pearson et al., 2003]: Shaly facies: a dark grey silty calcareous shale and argillaceous marl in the lower half of the sequence, Sandy-Carbonate rich facies: a grey sandy and argillaceous limestone in the middle of the sequence which is almost absent in north-eastern Switzerland and Sandy facies: silty to sandy marls with sandstone lenses cemented with carbonate in the upper part [Houben et al., 2014]. In this study, the modelling work of porous morphological structure and the prediction of gas migration process are envisaged on samples taken from the shaly facies. In [Keller et al., 2011], the 3D geometric and topological

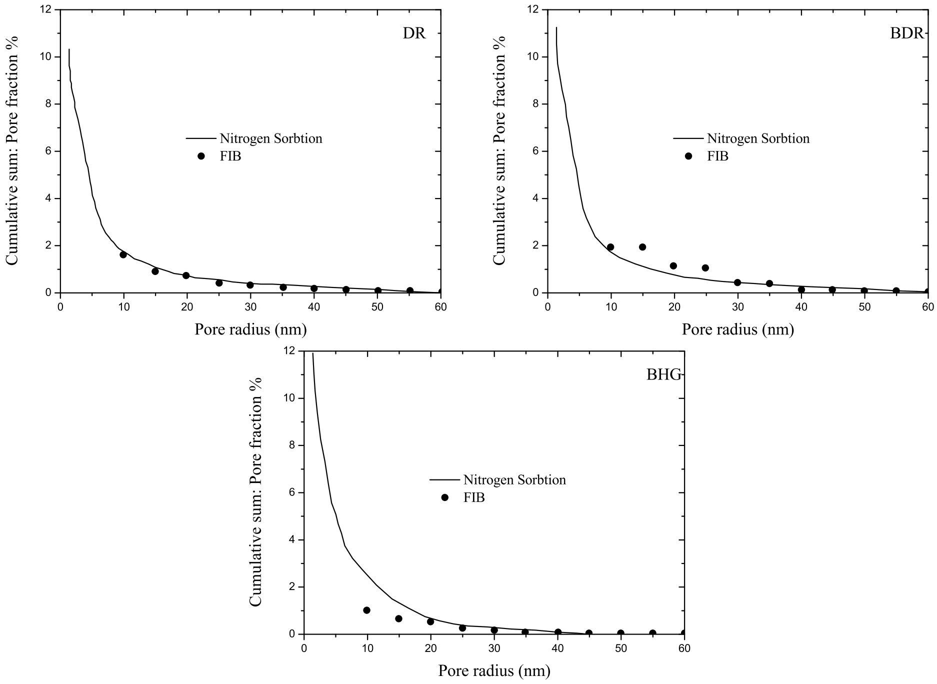

Figure 4.16: Pore size distribution in shaly facies Opalinus clay samples from FIB and N_2 adsorption methods [Keller et al., 2011].

information of shaly facies Opalinus clay are investigated through FIB technique on three samples which are labelled BHG, BDR and DR and are all taken from the shaly facies about 250 m below the surface. FIB provides data of the 3D pore space down to about 5 nm. The most frequent pore radii distributes between 10 nm and 50 nm and the corresponding physical porosity ranges between 1% and 2%. N_2 adsorption isotherms is also used for the determination of pore size distribution. Data shows that the physical porosity of pores with radii larger than 10 nm is between 1.7% and 2.2% which is in accordance with FIB results. Therefore, the majority of the pores with radii ranging between 1.5 nm and 10 nm present a porosity of about 10% which is immeasurable in FIB owing to the limited voxel size. The pore size distribution curves are illustrated in Figure 4.16. The 3D reconstruction of porous space is segmented from the SE images, shown in Figure 4.17 (red stands for the porous space and yellow represents the calcite grains).

In [Marschall et al., 2005], a comparison of the mesoscopic pore size distributions is realized among data from MIP test, from the adsorption/desorption of nitrogen isotherms and from the water isotherms. Measured distributions are highly dependent on the applied methods. Assuming a total physical porosity of 12%, the MIP data shows that the fraction of pores with radii larger than 25 nm is about 10%, between 3.7 nm and 25 nm is 51%

and below 3.7 nm is about 39%. It can be concluded that in Opalinus clay, the majority of pores are very small, with equivalent radii smaller than about 10 nm.

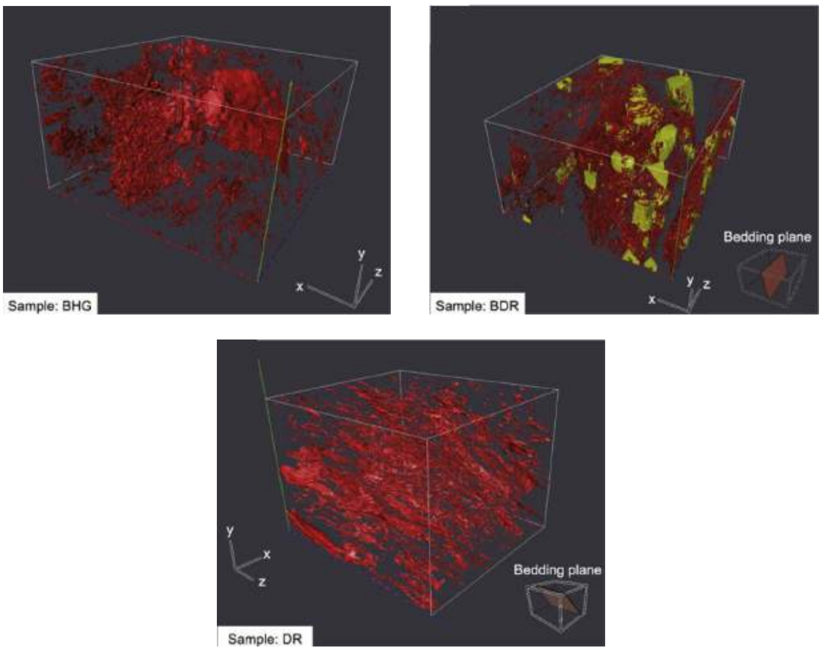

Figure 4.17: FIB results of shaly facies Opalinus clay samples (red: porous space, yellow: calcite grains) [Keller et al., 2011].

According to the procedure of generation of the porous morphological model using excursion set of Gaussian Random Field, the assuming correlation lengths are 0.002 µm, 0.01 µm, 0.025 µm and 0.04 µm. Union of excursions is performed in a cubic domain with 0.5 µm on each side. The mesh is chosen as 800^3 thus determines the voxel size down to 0.6 nm, which means the whole pore size range in Opalinus clay can be involved in the generated model. The total porosity is targeted slightly higher than 12% in order to counteract the influence of close porosity. In order to eliminate the inaccurate estimation of gas migration properties owing to the randomly distributed porous network, a number of models (10 models) are realized to determine the mean characteristics, then the corresponding gas breakthrough pressure will be chosen as the average. Two realizations are presented in Figure 4.18. Pores are shown with blue and gray parts of the cube represent the matrix. Subsequently, morpho-mathematical analysis including geodesic reconstruction and morphological opening are conducted to verify the numerical model. Pore size distribution in morphological model is compared with FIB and N_2 absorption results from [Keller et al., 2011] and shows good agreement with the latter, see Table 4.4. In the same way, pore size ranges are compared with results of MIP test from [Marschall et al., 2005], see Table 4.5. Since the Opalinus clay exhibits a extremely low porosity comparing with

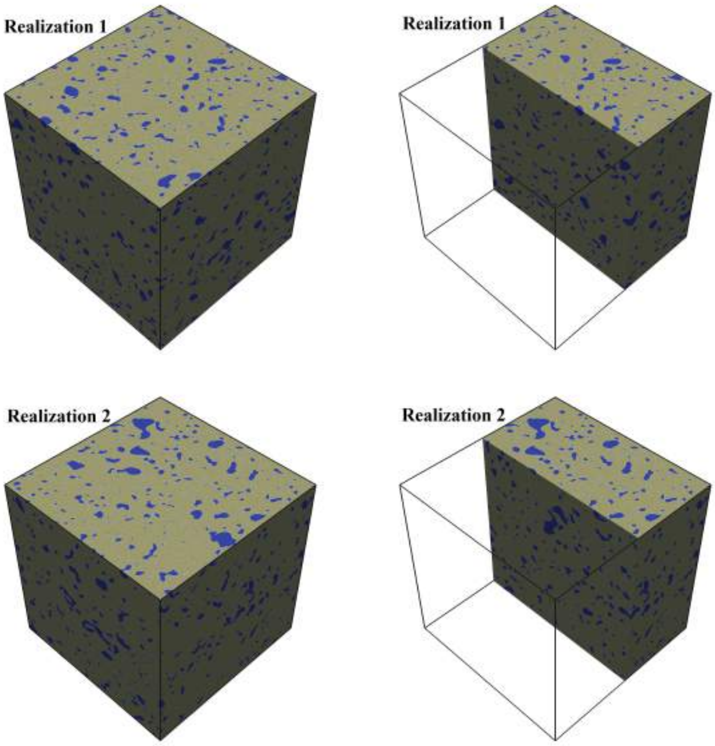

Figure 4.18: Two realizations of morphological porous space in Opalinus clay.

Table 4.4: Comparison of pore size distributions obtained from FIB, N_2 absorption and morphological model.

Porosity	FIB	N_2 absorption	Morphological model
radii $>$ 1.5 nm	Immeasurable	10.4 - 11.5	9.5 - 11.8
radii $>$ 10 nm	1 - 2	1.7 - 2.2	0.7 - 1.8

another porous mediums (e.g. COx argillite, Boom clay, cement paste) and a large proportion of narrow pores, the effective pore radius of breakthrough pathways in Opalinus clay is envisaged much narrower than in another mediums. Thus, the applied gas pressure for the creation of continuous gas flow only by the excess of capillary resistance is supposed to be much higher. However, after achieving the intersection of two geodesic reconstructions beginning with opposite faces in the initial porous models, results show that the porous

Table 4.5: Comparison of pore size distributions obtained from MIP and morphological model.

Fraction of pores (%)	Mercury injection	Morphological model
radii < 3.7 nm	39	50
3.7 nm < radii < 25 nm	51	46
radii > 25 nm	10	4

connectivity between two opposite faces can not be ensured. In other words, during the morphological analysis, for a initial saturated porous network which possesses a porosity about 12% and principal pore size smaller than 25 nm, gas phase is not able to traverse the medium without bringing any change to the porous structure. This observation has also been mentioned in experimental tests in [Hildenbrand et al., 2002b]. Evaluations of measurements on the Opalinus clay yielded effective permeability lower by several orders of magnitude than those observed for the other samples of Tertiary mudstone and Boom clay. The typical capillary induced breakthrough process did not exist. In regards with the numerical evaluation in morphological model of Opalinus clay, it can be concluded that no gas breakthrough pathway exists in the original porous network, gas can leak out neither by two-phase flow nor by dissolved state into the drained water. The possible gas expulsion hypothesis are through the pathway dilation or the macro-fracture within which porous space can be enlarged thus a connected flow path may finally form between the upstream and the downstream sides.

5.2 Boom clay

In Belgium, the investigation of disposal of high-level radioactive waste is ongoing with the Boom clay. In the same way, Boom clay is also been chosen for its favourable properties in repository performance, for instance, the low hydraulic conductivity [Wemaere et al., 2008], the high adsorption capacity for many radionuclides [Maes et al., 2004] and the self-sealing properties due to its elasto-plastic behaviour [Van Geet et al., 2008]. In [Le et al., 2008] and [Lima et al., 2012], gas injection tests show that the gas entry pressure (stands for the breakthrough pressure in this study) is estimated about 5 MPa. Since the lithostatic pressure which represents the pressure imposed by the weight of the overlying material is about 4.5 MPa, the creation of continuous two-phase flow will form across the

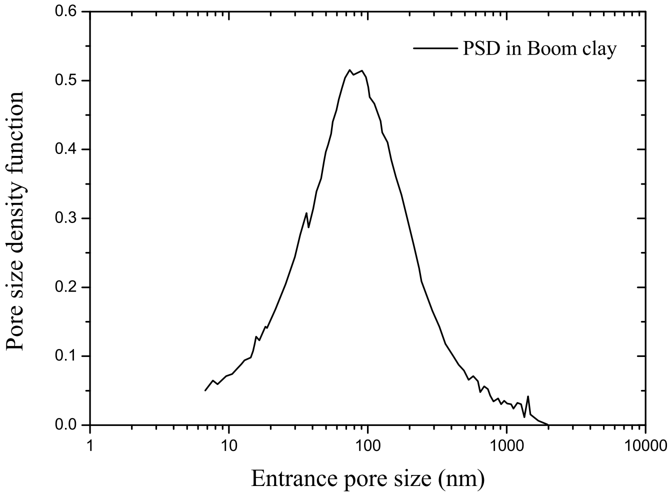

Figure 4.19: Pore size distribution curve of Boom clay [Lima et al., 2012].

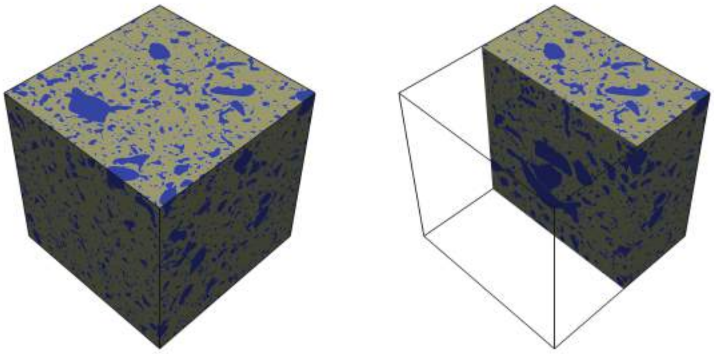

Figure 4.20: A realizations of morphological model of porous space in Boom clay.

porous space after the pathways dilation which corresponds to the increasing porosity.

In this work, focus is mainly drawn to the numerical point of view: using morphological model to determine the required gas pressure for the creation of drained pathways across the porous network. A detailed characterization of the pore space down to nanometre scale is required for a full microphysical understanding of the material's transport properties. In order to construct the pore space morphology and verify its connectivity in 3D, the total porosity needs be firstly defined. Standard bulk porosity measurements, using mercury injection porosimetry, on dried Boom Clay samples give interconnected porosity between 23 and 40%, accessible through pore throat diameter above 3.6 nm [Hemes et al., 2015][Hemes et al., 2013][Hildenbrand et al., 2002b][Hildenbrand et al., 2004]. Measured total porosity based on water content (by drying at 100 ℃) is in the range of 36 - 39%. The total interconnected porosity of Boom clay is then defined as 25% in this work. Mercury

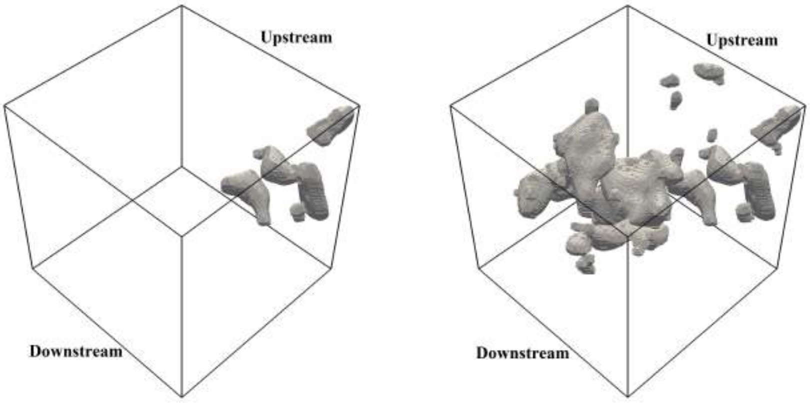

(a) $P_g = 0.51$ MPa. (b) $P_g = 1.71$ MPa, gas entry.

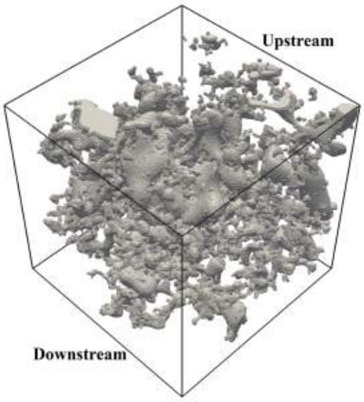

(c) $P_g = 4.24$ MPa, gas breakthrough.

Figure 4.21: Drainage process with increasing gas pressure in the Boom clay model.

intrusion porosimetry tests which are performed on freeze-dried samples show that the pore size distribution curve in Boom clay possesses one dominant pore mode at around 90 nm [Lima et al., 2012], see Figure 4.19. Pore size distributes in a large range between 6 nm - 2 µm. Regarding this, the morphological model of Boom clay is decided to include 10 single excursions with correlation lengths of 20 nm, 50 nm, 70 nm, 90 nm, 200 nm, 400 nm, 600 nm, 800 nm, 1 µm, 1.5 µm. Size of cubic domain is chosen as 5 µm. Thus, a mesh with 800 points on each side gives the voxel size of 6.25 nm. A realization of porous space morphology is shown in Figure 4.20. In comparison with the pore size distribution in COx argillite which shows a peak size around 20 nm and main pore size range between 3 nm - 1 µm, pores in Boom clay are slightly larger than in COx argillite. In addition, accessible porosity in COx argillite is lower than in Boom clay. Considering these, the pore throat in breakthrough pathways may be larger thus leads to a lower breakthrough

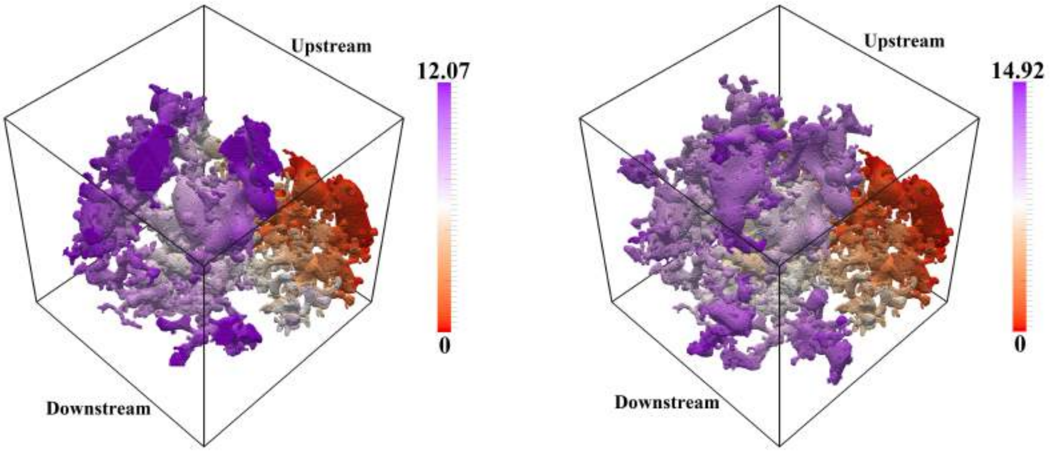

(a) The shortest length of 12.07 µm. (b) The longest length of 14.92 µm.

Figure 4.22: Geodesic distances in breakthrough pathways of the Boom clay model.

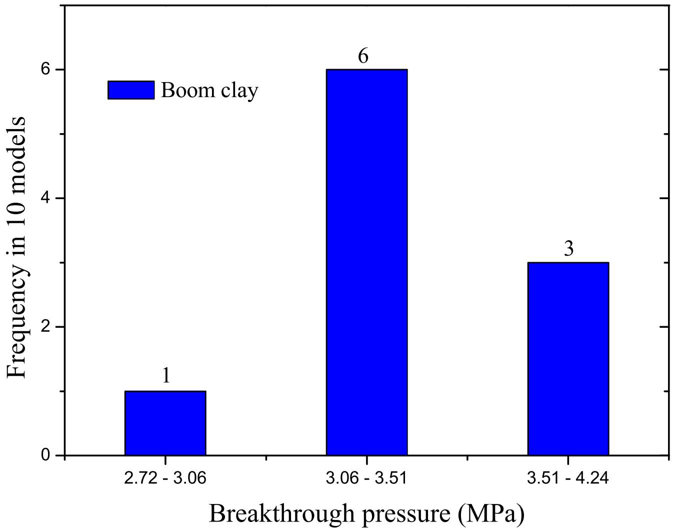

Figure 4.23: Numerical estimation of gas breakthrough pressure in Boom clay (results from 10 tests).

pressure. The drainage process with increasing gas pressure in the Boom clay realization is presented in Figure 4.21 and the corresponding geodesic distances in breakthrough pathways are illustrated in Figure 4.22. In this model, gas entry appears at 1.71 MPa and breakthrough at 4.24 MPa. Results of numerical estimation performed with 10 models which are generated through the same process but with different morphological aspects are shown in Figure 4.23.

From the results, simulated gas breakthrough pressure is predominantly located between 3.06 - 3.51 MPa, with another high possibility in 3.51 - 4.24 MPa. In view of the experimental gas breakthrough pressure of about 5 MPa and the lithostatic pressure of 4.5 MPa, morphological model shows that if the rate of gas generation is larger than the diffusive flux, gas leakage may happen through capillary two-phase flow without any change to the porous structure. This difference is supposed to be reasonable since the morphological model can take account of the pore geometrical and topological information but not be able to reflect the real morphological aspect in samples. Some aspect characteristics which are determined during its sedimentation history and diagenetic evolution are not capable to be represented through the union of excursions. In spite of this shortcoming, the morphological model gives a prediction of breakthrough pressure between 3.06 - 4.24 MPa which is close to the experimental value thus is thought to be acceptable.

5.3 Cement paste

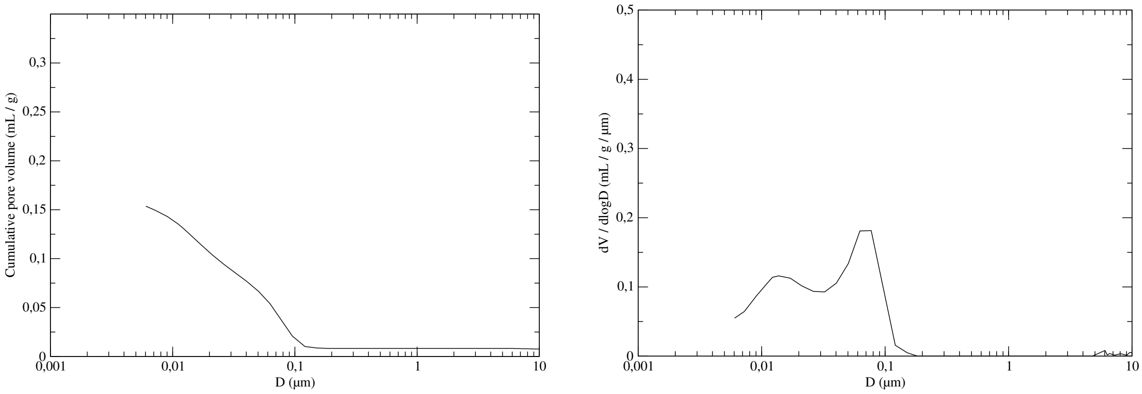

Figure 4.24: Pore size distribution curve of cement paste with W/C = 0.5 [Wu, 2014].

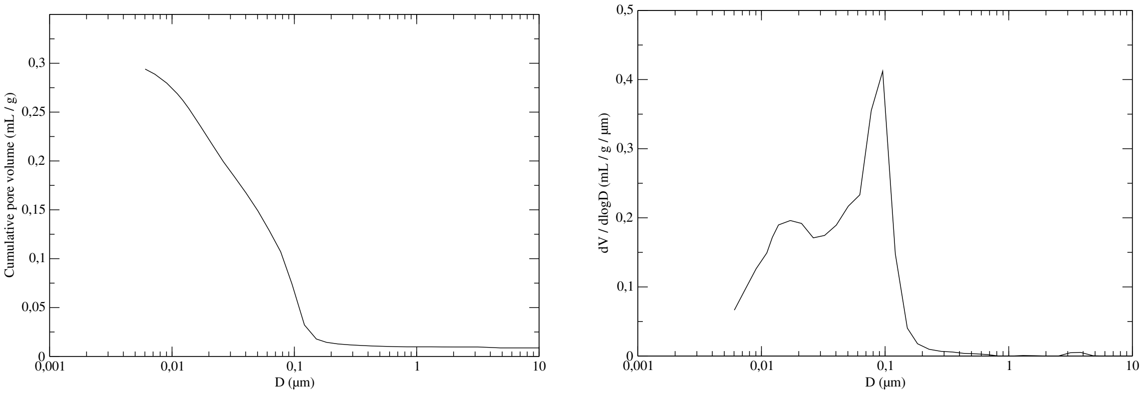

Figure 4.25: Pore size distribution curve of cement paste with W/C = 0.8 [Wu, 2014].

Besides the investigation of gas migration in low-permeable clay in the context of radioactive waste repository, idea can be applied to another domain such as the geologic carbon sequestration which is referred as the separation and capture of CO_2 followed by injection into the geosphere for long term storage. The sequestration of CO_2 requires a leakage rate less than 1% of stored CO_2 per 100 years. The preferential sites for CO_2 injection and storage have been chosen in areas that have a history of oil, natural gas, and coalbed methane production. Wells for previous exploration and production are used to penetrate formations for CO_2 sequestration. A cement slurry is placed in the annular space to prevent the flow of fluids along the annulus. Abandoned wells are sealed with cement plugs inside to block the vertical migration of fluids. The permeability and integrity of the cement in the annulus and in the wellbore seal will determine how effective the cement is in preventing fluid leakage. The cement must be capable to maintain a low permeability over long period under reservoir conditions in a CO_2 injection and storage scenario [Kutchko et al., 2007][Kutchko et al., 2008].

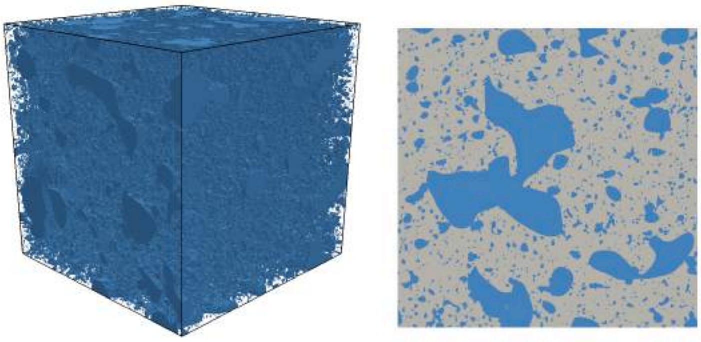

Figure 4.26: Morphological model of cement paste with W/C = 0.5 [Hosseini, 2015].

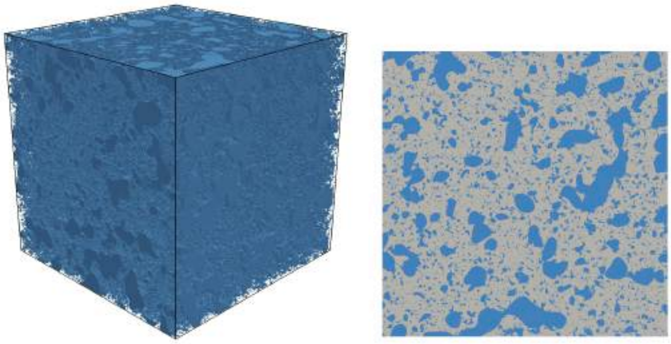

Figure 4.27: Morphological model of cement paste with W/C = 0.8 [Hosseini, 2015].

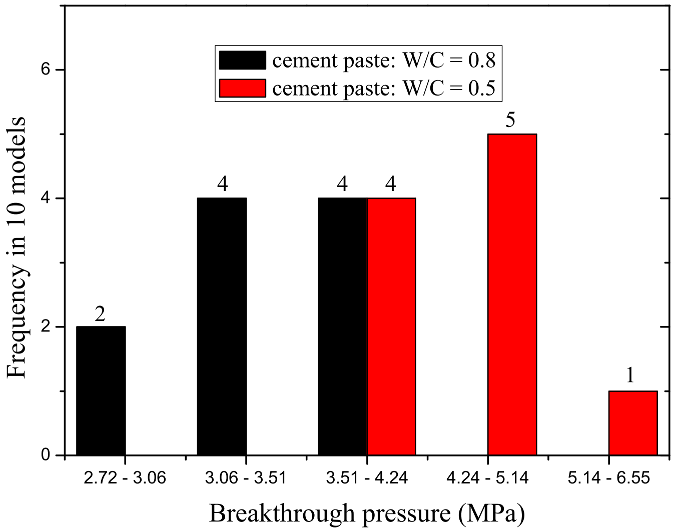

Figure 4.28: Numerical estimation of gas breakthrough pressure in cement paste with W/C = 0.5 and W/C = 0.8 (results from 10 tests).

Wells are typically completed with Portland cement. When the compounds of Portland cement are mixed with water, the hydration process begins. During this process, the generated porous network depends on the arrangement of various hydration products. Cement paste possesses two types of pores: capillary pores and pores of hydrates. The capillary pores which corresponds to the peak of large diameter are initially filled by the mixing water. An increasing W/C radio (ratio of the weight of water to the weight of cement) leads to the increase of the dimension and the volume of capillary pores. The pores of hydrates which are related to the peak of smaller diameter represent the interlayer space with sizes determined by conditions of hydration.

The simulation work are envisaged with two types of cement paste: W/C = 0.8 and W/C = 0.5. Mercury intrusion provides the pore size distribution curves, see Figure 4.24 and Figure 4.25.

Results indicate a porosity of 25% for cement paste with W/C = 0.5 and a porosity of 32% for cement paste with W/C = 0.8. Since mercury intrusion only takes place in boundary-connected pores, the total porosity which includes the open porosity and the close porosity will be targeted higher than these values. The morphological modelling is performed by using data from the work of Mahban Hosseini (colleague in LML who studies the morphological structure in cement paste). In her Ph.D. thesis [Hosseini, 2015], a final 30% porosity for W/C = 0.5 and 40% porosity for W/C = 0.8 have been chosen. Regarding the experimental curve of pore size distribution, the generation of numerical model for cement paste with W/C = 0.5 is realized through the union of eight excursions

(0.12, 0.07, 0.04, 0.025, 0.015, 0.011, 0.008, 0.005 µm). For cement paste with W/C = 0.8, they are defined as 0.15, 0.1, 0.065, 0.04, 0.02, 0.012, 0.009, 0.005 µm. Figure 4.26 and Figure 4.27 illustrate the generated models in cubic domain of 1 µm.

In a cubic domain of 5 µm, the estimated gas breakthrough pressures from ten models are illustrated in Figure 4.28. For cement paste with W/C = 0.5, gas breakthrough pressures are predominantly located between 3.51 - 5.14 MPa (9 times), with another low possibility in 5.14 - 6.55 MPa (1 times). For cement paste with W/C = 0.8, eight of the total models provide gas breakthrough pressure between 3.06 - 4.24 MPa and the rests are located between 2.72 - 3.06 MPa. In comparison with the COx argillite, although pore sizes in these two types of materials are principally located in a same range between 5 nm - 1 µm, cement pastes possess larger open porosity (COx argillite: about 20%, cement paste with W/C = 0.5: 25%, cement paste with W/C = 0.8: 32%) and higher peak pore size (COx argillite: about 20 nm, cement paste with W/C = 0.5: 75 nm, cement paste with W/C = 0.8: 100 nm), thus leads to relatively lower breakthrough pressures. Considering the Boom clay with peak pore size about 100 nm, the proportion of pores between 100 nm and 1 µm is more significant. As a result, the breakthrough pressure in Boom clay is estimated to be around a lower value than in cement paste of W/C = 0.5 and approximate with values in cement paste of W/C = 0.8. In view of these characteristics, simulated gas breakthrough pressures in cement pastes are supposed to be reasonable and acceptable and could be used for a better understanding of the sequestration capacity of CO_2.

6 Conclusions

The gas breakthrough process is investigated in this chapter using morpho-mathematical operations. According to Young - Laplace law, with defined water surface tension and wetting angle, gas phase preferentially invades large interconnected pores. Gas breakthrough refers to the excess pressure in gas phase at which the propagation of drained pathways reaches the downstream side and continuous flowpaths form across the pore network.

Based on this mechanism, the first step is to extract interconnected pores between the upstream and the downstream sides. It is realized by an intersection between two inverse geodesic reconstructions. Following this, in order to calculate the gas entry pressure, gas breakthrough pressure and drained porosity, the proposed numerical method includes: 1, a sequence of morphological opening with increasing size of the structuring element, 2, a geodesic reconstruction beginning with the upstream side. The sizes of the used structuring elements determine the entry and the percolation thresholds.

Results indicate that breakthrough pressure is determined by the size of pore throat of breakthrough pathways. Its spatial position brings no influence to the resulting value. But for entry pressure, the spatial position of entry pore throat is rather important. In consideration of the randomly formed pore space, gas entry pressure can not always be detected. In view of the spatial varying property of Random Field, the simulation work must be performed with several realizations. For Model 1, $2.18 < P_{\text{entry}} < 3.06$ MPa and $4.24 < P_b < 6.55$ MPa. For Model 2, $2.72 < P_{\text{entry}} < 4.24$ MPa and $5.14 < P_b < 9$ MPa. For Model 3, $5.14 < P_{\text{entry}} < 6.55$ MPa and $9 < P_b < 16$ MPa. These differences are related to the determination of the proportion of small pores using different methods. Model 1 and Model 2 are in good accordance with experimental values. For Model 3, the proportion of small pores is overestimated thus leads to overestimation of breakthrough pressure.

Breakthrough path tortuosity is characterized by geodesic distance. It ranges between 1.5 - 4.13. Surface tension is influenced by temperature. Under higher temperature condition, gas breakthrough becomes easier. However, the influence of pore pressure and confining pressure is difficult to be realized. A reliable stress - strain model needs be involved to provide accurate results.

Furthermore, the proposed method is applied for another potential host rocks for the storage of radioactive waste such as the Opalinus clay from Switzerland and the Boom clay from Belgium. For Opalinus clay, due to its low porosity and narrow principal pore sizes, no connected pathway exists in the generated model. Thus the breakthrough process is more likely through pathway dilation or fracture. For Boom clay, the obtained gas breakthrough pressure is mainly located between 3.06 - 4.24 MPa. Ultimately, an investigation is performed for cement paste in the context of sequestration of CO_2.

Based on these results, it can conclude that the proposed numerical methods are capable to predict gas entry and gas breakthrough pressures in low-permeable media and provide realistic geometrical and topological information. Some potential improvements are envisaged to consider poro-mechanical coupling to provide more accurate estimations.

Chapter 5

Re-imbibition process

Contents

1 Introduction

In long term repository, the gradually increasing gas pressure due to various origins will consequently induce a movement of the interstitial fluid until the leakage. After that, the discharge of gas pressure can lead to a re-imbibition process [Gerard et al., 2008][Hildenbrand et al., 2002b][Hildenbrand et al., 2002a][Hildenbrand et al., 2004]. Interconnected gas migration pathways would be progressively closed until the gas effective permeability drops to zero. In view of this point, another experimental scenario which aims at the investigation of gas sealing efficiency of low-permeable rocks after the re-imbibition process has been proposed. Tradition method which performs a drainage process until the breakthrough requires a long duration in order to avoid the overestimation of gas breakthrough pressure. The new scenario is accomplished by imposing a higher gas pressure than the expected gas breakthrough pressure on the upstream side of initially saturated sample, thus the gas breakthrough rapidly occurs. The pressure of the downstream side increases while the pressure of the upstream side decreases correspondingly. Finally, after the shut-off the last interconnected pathways, gas leakage stops and a residual pressure difference is obtained to evaluate the gas sealing capacity of the studied material.

Parameters recorded during the drainage process and the water imbibition process are summarized in Figure 5.1. In Figure 5.1(a), the effective gas permeability of sample which varies with time is determined from the pressure change at the downstream side using Darcy's law for compressible media. It firstly increases to a peak value then decreases to 0 when the pressure difference remains stable. In Figure 5.1(b), curve I represents the classical method by gradually increasing the upstream pressure. During this process, gas pressure firstly reaches the entry threshold then produces remarkable water desaturation. Subsequently, when the second threshold - breakthrough is passed, gas leakage happens. If the gas pressure continues increasing, water saturation can finally drop to the IRWS (Irreducible Water Saturation) which corresponds to the remained water phase in non-interconnected pores. Due to technical difficulties, the assessment of breakthrough pressure is performed through the spontaneous imbibition after breakthrough as illustrated by curve $\mathrm{I}_{\mathrm{exp}}$. Applied gas pressure is higher than the expected breakthrough pressure, thus the breakthrough rapidly occurs. When the curve reaches the IRWS, gas permeability arrives at the peak value. After that, imbibition begins and progressively closes drained pathways, then gas permeability starts to decrease as shown by curve II. Ultimately, when gas permeability drops to 0, the maintained pressure difference is used to evaluate the capillary sealing efficiency. If the pressure difference continues decreasing to 0 by forced imbibition, a final RGS (residual gas saturation) is obtained due to the isolated gas-filled pores during the imbibition process. The hatched area stands for the possible underestimation of the capillary sealing efficiency.

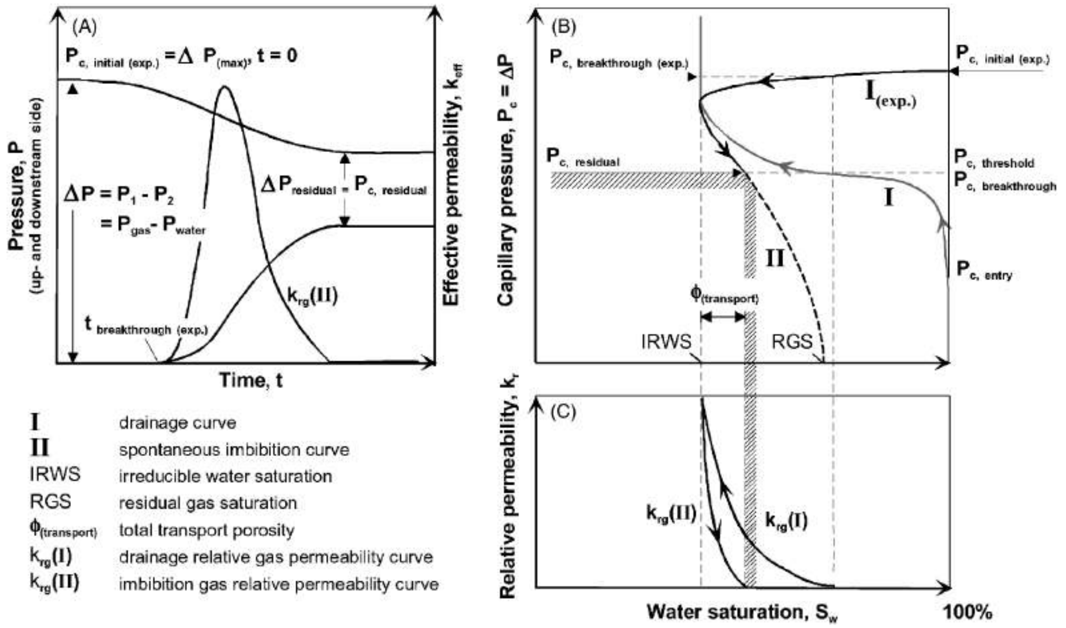

Figure 5.1: Parameters recorded during the drainage process and the water imbibition process [Hildenbrand et al., 2002b].

In this chapter, focus is mainly drawn to the simulation of the re-imbibition process after breakthrough using the generated 3D models from excursion set theory and the combination of several morpho-mathematical operations.

2 Re-imbibition process and residual saturation

2.1 Gas shut-off pressure

Gas breakthrough involves the creation and the propagation of preferential pathways. These flowpaths comprise the largest interconnected pores, which offer the least resistance to capillary movement. As an inverse process, water re-imbibition preferentially takes place in the smallest pores which directly connect with the downstream side, then successively occurs in large pores. In small pores, higher capillary forces could overcome the gas resistance thus push back the gas phase. Hence, due to the continuous loss of conducting gas pathways, gas permeability begins decrease and finally drops to zero. As mentioned before, under isothermal conditions, gas breakthrough pressure can be determined by two morphological properties: the 3D connectivity and the size of pore throat in breakthrough pathways. The spatial position of pore throat influences the gas entry pressure rather than the gas breakthrough pressure. In most cases, breakthrough pore throat locates in the porous network instead of touching the surface. In view of this, during the re-imbibition process, a lower gas pressure than the breakthrough pressure (hereafter called as the gas shut-off pressure, noted as P_s) is envisaged to shut off the last interconnected pathway and to make the effective gas permeability drops to zero. Medium then turns into a gas-impermeable state. In regards with the practical issue of long term storage of radioactive waste, when arriving at this state, gas accumulation reappears until the next breakthrough.

A simple example is presented in Figure 5.2. Gas breakthrough pressure is calculated by Young-Laplace equation using the pore throat size d and gas shut-off pressure is determined by the pore size at the downstream side D, the relation is yield as:

$$P_b = \frac{4\gamma\cos\theta}{d} > P_s = \frac{4\gamma\cos\theta}{D} \tag{5.1}$$

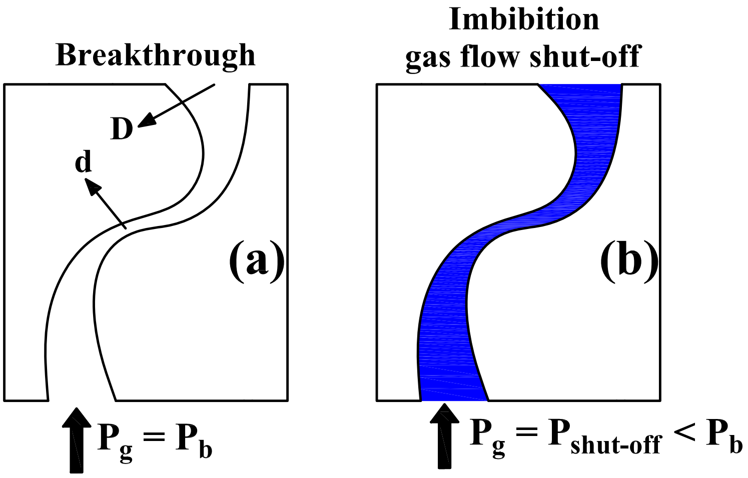

Figure 5.2: Illustration of the re-imbibition process and gas pathway shut-off, (a), breakthrough, (b), imbibition and path shut-off.

2.2 Residual saturation

More interestingly, considering the same gas pressure during the drainage process and the re-imbibition process, water saturation degrees of sample in these two states are not identical. This difference is mainly due to two mechanisms:

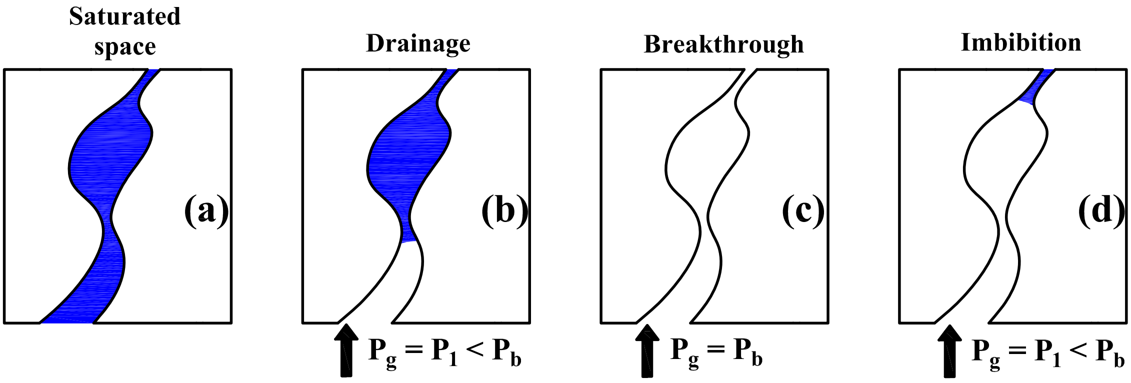

Figure 5.3: Illustration of the 1st mechanism of the water saturation difference, (a), initial saturated porous space, (b), drainage with P_1, (c), breakthrough with P_b, (d), imbibition with P_1.

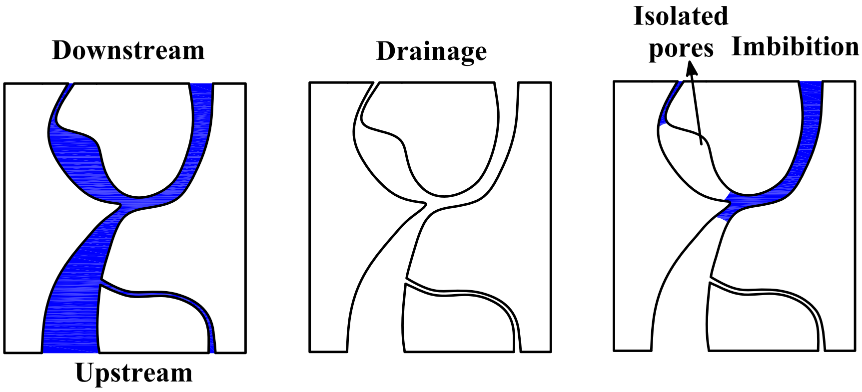

Figure 5.4: Illustration of the 2nd mechanism of the water saturation difference (isolated pores).

1, water drainage and water imbibition are inverse processes starting with opposite faces. More specifically, the size of the water-gas interface is controlled by the applied gas pressure but its spatial position highly depends on the chosen plan where the fluid injection begins. As illustrated in Figure 5.3, in a randomly shaped breakthrough pathways, the water-gas interfaces of these two processes commonly appear at different spatial positions which is determined by the starting plan and the morphological aspect of porous space. It should be noted that this type of water saturation difference temporarily exists. During the successive discharge of gas pressure, water can finally fill again the drained space.

2, assuming that the gas phase stays incompressible for the purpose of simplification, during the re-imbibition process, certain gas-filled pores may become isolated and would stay in desaturated state when the flow pathways are interrupted, resulting in a residual saturation. As depicted in Figure 5.4, isolated pores are suitable to be described as "close pores" with two extremities of imbibing water. More importantly, unlike the former mechanism, a continuous decrease of gas pressure is not able to re-saturate the isolated pores. Ultimately, sample will be partially saturated and a new total saturation state needs be accomplished by a complementary water pressure.

3 Numerical point of view

The simulation work in this part involves the extraction of water imbibition pathways, the estimation of gas shut-off pressure and the calculation of imbibing water saturation and the corresponding gas residual saturation. In consideration of the complexity of the spatial structure of the randomly generated pore space, the difficult point is to establish a reliable numerical method which is suitable for different morphologies and is still be able to provide accurate result estimations. The proposed method combines several morpho-mathematical operations including morphological opening, geodesic reconstruction, subtraction and union of excursions. Different steps of proposed scenario are shown schematically in Figure 5.5.

At the outset of proceedings, a totally or partially drained porous space after breakthrough is implemented as the initial image, denoted as M_0 (Figure 5.5(a)). The resulting imbibition pathways is assumed as Figure 5.5(b).

In the first place, M_0 is subjected to a filtering process by morphological opening in order to eliminate possible imbibition pores in which gas pressure is lower than capillary resistance (Figure 5.5(c)). Denoting the corresponding structuring element as E_1 and the remaining porous space as V_1, Thus yielding to:

$$V_1 = M_0 \circ E_1 \tag{5.2}$$

Afterwards, the eliminated parts V_2 are obtained through binary subtraction between initial image M_0 and image (c) (see Figure 5.5(d)):

$$V_2 = M_0 - V_1 = M_0 - M_0 \circ E_1 \tag{5.3}$$

Following this, a geodesic reconstruction from the downstream side provides the accessible imbibition pathways V_3 and the corresponding imbibing water saturation (Figure 5.5(e)), it is defined by:

$$V_3 = R_{(-)}(V_2) = R_{(-)}(M_0 - M_0 \circ E_1) \tag{5.4}$$

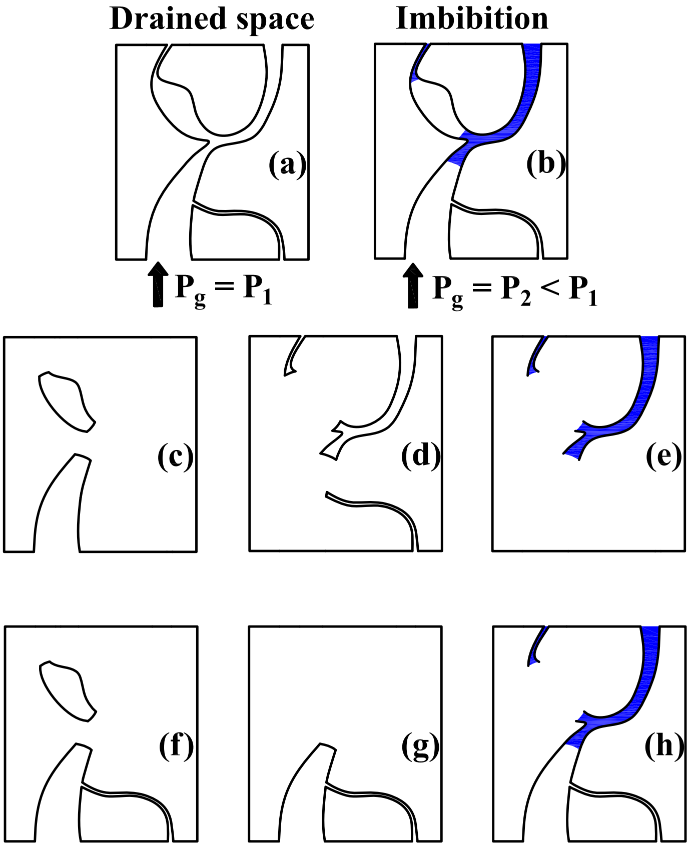

Figure 5.5: Proposed method to estimate gas shut-off pressure, imbibing porosity and residual saturation. (a), Drained porous space as initial image M_0, (b), resulting imbibing porosity, (c), step 1: morphological opening with a defined size, (d), step 2: subtraction between (a) and (c) to find possible pores for imbibition, (e), geodesic reconstruction from downstream side of (d) to determine accessible pores for imbibition, (f), subtraction between (a) and (e) to eliminate accessible pores for imbibition, (g), geodesic reconstruction from upstream side to eliminate pores isolated by imbibition. If geodesic reconstruction can not end at the downstream side, gas pathway then shut-off. The size of the used structuring element determines the shut-off pressure, (h), union (e) and (g) to build a new image M_1 for following calculations.

Subsequently, another binary subtraction is performed between initial image M_0 and image (e) to erase imbibition part (Figure 5.5(f)), the new built space V_4 is givens as:

$$V_4 = M_0 - V_3 = M_0 - R_{(-)}(M_0 - M_0 \circ E_1) \tag{5.5}$$

After this step, by applying another geodesic reconstruction from the upstream side of image (f), pores isolated by imbibing water could not be conserved since their boundary connectivity no longer exists (Figure 5.5(g)). In addition, if geodesic reconstruction stops before reaching the downstream side, that means the last interconnected pathway has been shut off. Then the applied gas pressure can be defined as the gas shut-off pressure. The new constructed image is given as:

$$V_5 = R_{(+)}(V_4) = R_{(+)}(M_0 - R_{(-)}(M_0 - M_0 \circ E_1)) \tag{5.6}$$

At the last step, accessible imbibition pathways are combined with result in image (g) thus leads to a new image M_1. Through this process, isolated pores which no longer play roles in imbibition process are removed from the new build image. Henceforth, if gas pressure continues decreasing, the new results could be obtained by repeating this process with the new initial image M_1,

$$M_1 = V_3 + V_5 = R_{(-)}(M_0 - M_0 \circ E_1) + R_{(+)}(M_0 - R_{(-)}(M_0 - M_0 \circ E_1)) \tag{5.7}$$

When applied gas pressure drops to zero, the residual gas saturation can be defined as the proportion of total eliminated isolated pores. Following this scenario, for a gas pressure P_n, the corresponding water imbibition pathways $\mathcal{P}_n$ and new build initial image M_n could be yield by:

$$\mathcal{P}_n = R^{\ominus}(M_{n-1} - M_{n-1} \circ E_n) \tag{5.8a}$$
$$M_n = R^{\oplus}(M_{n-1} - R^{\ominus}(M_{n-1} - M_{n-1} \circ E_n)) + R^{\ominus}(M_{n-1} - M_{n-1} \circ E_n)$$

where n$\geqslant$1, M_0 stands for the totally or partially drained porous space after breakthrough, E_n is derived from Young-Laplace equation.

4 Results of imbibtion and discussion

As introduced before, in most cases, breakthrough pore throat locates in the porous network instead of touching the surface thus leads to gas shut-off pressure lower than breakthrough pressure. The porous structure and the initial state of drained porous network after breakthrough predominantly control the following imbibition process and final water saturation. Realizations of imbibing water morphology with decreasing gas pressure for total drained model is shown in Figure 5.6 (blue parts stand for the imbibing water). Apparently, the water inlet pores are the smallest at the beginning with another larger pores successively participate until the unloading of gas pressure.

Curves of water saturation as a function of gas pressure in Model 1 of COx argillite with drainage in X- direction and imbibition in X+ direction are plotted in Figure 5.7.

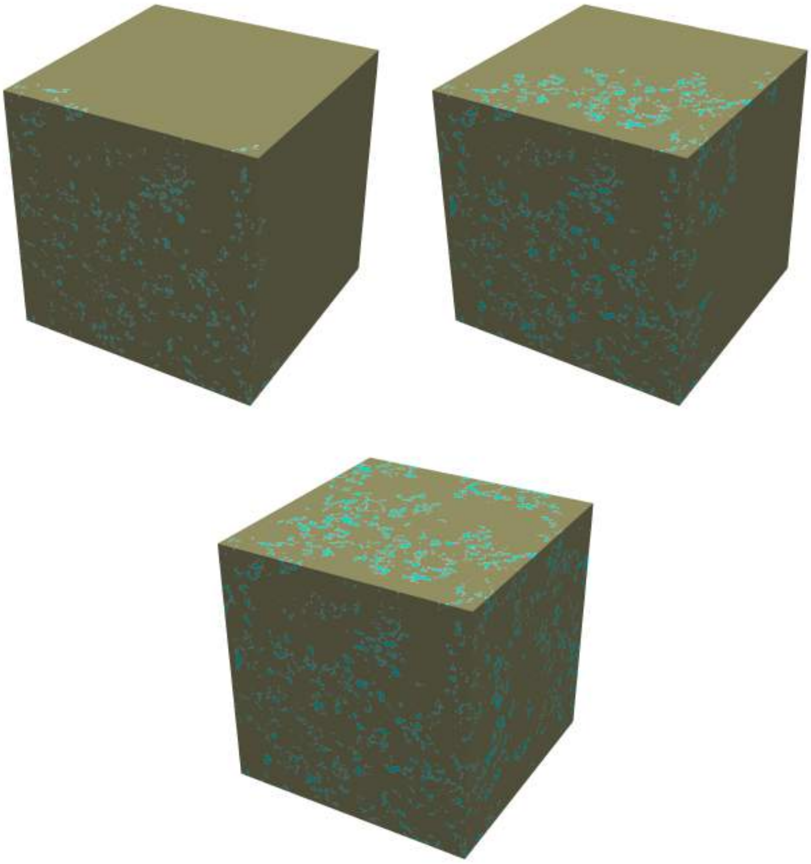

Figure 5.6: Realizations of water imbibition process with decreasing gas pressure in a total drained model, gas pressure decreases from (a) to (c).

Results for the Boom clay are shown in Figure 5.8. For the two cases, the remarkable imbibing water saturation (IWS) lower than 100% confirms the existence of isolated pores which will remain desaturated state without complementary water pressure. It should be noted that limited by the mesh density in generated model and the corresponding smallest structuring element, the requiring pressure for total drainage at X- direction is considered higher than 16 MPa and is incapable to be precisely defined. In fact, considering the repository formation, this pressure level is hardly be reached since gas leakage has already happened at much lower pressures through continuous flow path and gas accumulation efficiency sharply decreases. Moreover, the generation of fracture leads to a higher equivalent porosity, thus the content of imbibing water will be higher than the simulation value. In view of this, imbibition follows the breakthrough is supposed be more reliable. Influenced by the spatial position of breakthrough pore throat, it has been mentioned before that the gas shut-off pressure may be lower than breakthrough pressure. The simulation work

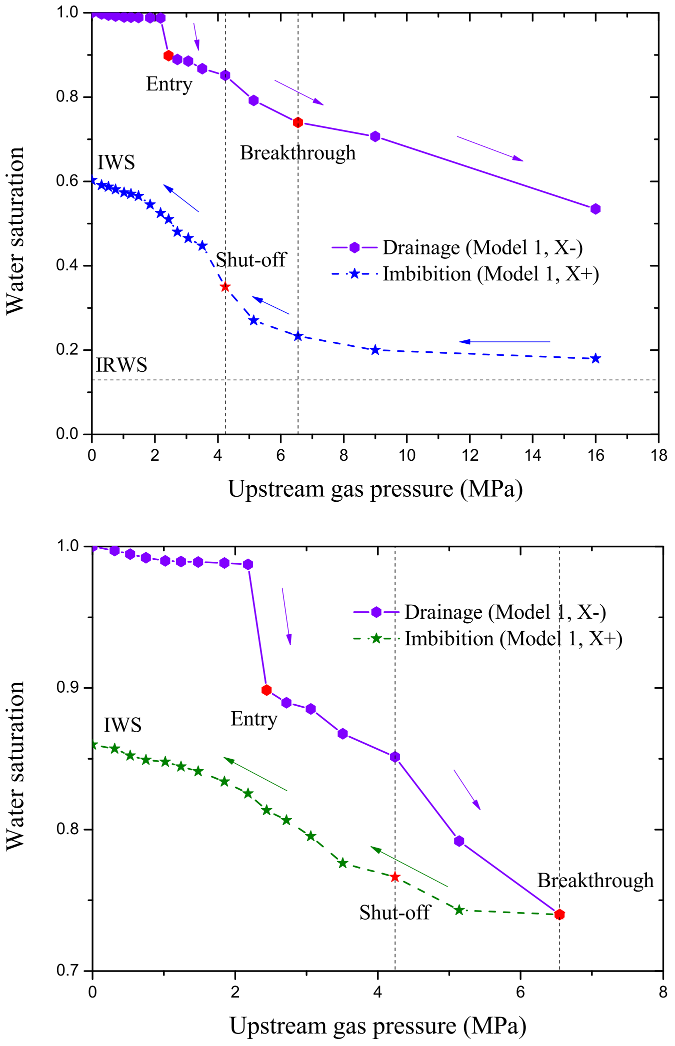

Figure 5.7: Water saturation variation during the drainage and the imbibition as a function of gas pressure for COx argillite considering two case: total drainage and partial drainage after breakthrough (Example: Model 1, drainage: x-, imbibition: x+), (a), Case 1: total drainage, (b), Case 2: partial drainage.

matches exactly this idea. For Model 1 of COx argillite, the P_s is about 4.23 - 5.14 MPa (estimated breakthrough pressure: 5.14 - 6.55 MPa). For Boom clay model, P_s is about 2.44 - 3.06 MPa (estimated breakthrough pressure: 3.06 - 4.24 MPa). It is easy to find that the different initial states of imbibition (totally drained or partially drained) bring no influence to the gas shut-off pressure. It is only determined by the pore space morphology. However, the final imbibing water saturation lower than 100% highly depends on the initial state.

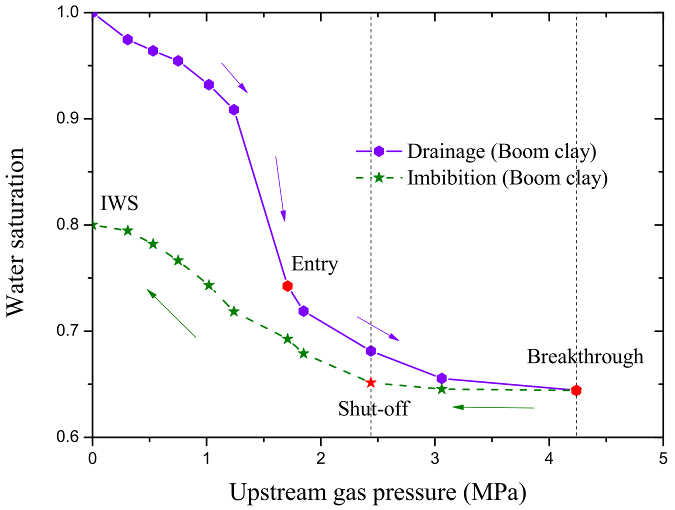

Figure 5.8: Water saturation variation during the drainage and the imbibition as a function of gas pressure for Boom clay considering the case of partial drainage after breakthrough.

5 Conclusions

In this chapter, the numerical investigation mainly focuses on the water-imbibition process after the gas breakthrough. It has been taken into consideration not only because it exists during the long-term repository when the discharge of gas pressure happens, but also because it is an interesting point of view to evaluate the gas sealing efficiency in several gas breakthrough experiments.

Water imbibition can be seen as an inverse process of water drainage. It happens in the smallest pores which directly connect with the downstream side then successively occurs in large pores. Interconnected gas migration pathways would be progressively lost until the gas effective permeability drops to zero. During this process, several interesting phenomenons are noticed. For example, the gas shut-off pressure stands for the applied gas pressure with which the last interconnected pathway is closed. In general, since the breakthrough pore throat locates in the porous network instead of touching the surface thus gas shut-off pressure is often lower than gas breakthrough pressure. Moreover, isolated pores may produce during the imbibition process and remain in desaturation state. If gas pressure is finally removed, sample will stay in partially saturated state.

The numerical method includes several basic morpho-mathematical operations such as the morphological opening, the geodesic reconstruction, the union of excursions and the binary subtraction. It is then capable to extract water imbibition pathways, to estimate the gas shut-off pressure and to calculate the imbibing water saturation and the corresponding gas residual saturation.

Results prove that water inlet pores are the smallest at the beginning with another large pores successively participate. The final imbibing water saturation lower than 100% confirms the existence of isolated pores. The obtained gas shut-off pressures lower than breakthrough pressures show good accordance with initial expectations.

Chapter 6

Gas migration scenario with low gas pressure

Contents

1 Introduction

In the previous chapters, gas migration scenarios are assumed only following capillary two-phase flow. The only factor which has to be taken into account is the difference between the applied gas pressure and the capillary forces. In fact, gas dissolution begins when gas phase under complementary pressure directly contacts with water phase. The dissolved gas molecules transfer principally through two modes: the molecule diffusion and the convection with interstitial water phase drainage. At low gas pressure (lower than entry pressure), water saturation degree is maintained nearly at 100%, thus the second mechanism is significantly restricted by capillary resistance. Molecular diffusion becomes a prominent transport process. In [Pusch et al., 1985], as to the gas migration at pressures lower than the critical pressure, diffusion of dissolved gas is probably of major importance. In [Duveau et al., 2011], even gas pressure is conserved at a low level, after a sufficient long duration, gas presence can still be detected at the downstream side and was supposed to be the dissolved species. More interestingly, dissolved gas is limited in water phase thus its breakthrough needs to be accomplished by water leakage. That means after the impediment of gas phase movement, a drainage process is always in progress. The dissolved gas can probably accumulate in saturated pores and porewater will be squeezed out from the sample. An hypothesis is proposed in this chapter to simulate this process.

2 Basic theories

Before the detailed study, several basic theories are indispensable to be introduced, such as the Henry's law, Fick's law and their applications.

Henry's law is used to quantitatively study the relation between the amount of dissolved gas and its partial pressure in the gas phase [Henry, 1803]. It is given as:

$$X_g = P_g \cdot K_{Hg} \tag{6.1}$$

where X_g is the mole concentration of dissolved gas in water, P_g is the gas pressure and K_{Hg} is the Henry's law constant. In other words, at a constant temperature, the amount of a given gas that dissolves in a given type and volume of liquid is directly proportional to the partial pressure of that gas in equilibrium with that liquid.

A large compilation of Henry's law constants has been published in [Sander, 2015][Sander, 1999]. Moreover, when the temperature of a system changes, the Henry's law constant will also change. There are multiple equations assessing the effect of temperature on the constant. The form of the Van't Hoff equation is expressed as:

$$K_{Hg} = K_{Hg}^{\ominus} \times \exp\Big(\frac{\Delta_{\text{soln}}H}{R}\Big(\frac{1}{T} - \frac{1}{T^{\ominus}}\Big)\Big) \tag{6.2}$$

where $\Delta_{\text{soln}}H$ is the enthalpy of solution, R is the ideal gas constant, $T^{\ominus}$ stands for the reference temperature of 298.15 K and $K_{Hg}^{\ominus}$ is the corresponding Henry's law constant. Thus the temperature dependence is given as:

$$C = \frac{-\mathrm{d}\ \ln K_{Hg}}{\mathrm{d}\ (1/T)} = \frac{\Delta_{\text{soln}}H}{R} \tag{6.3}$$

These equations are approximations only and should be used when no better experimentally derived formula for a given gas exists. For instance, at the reference temperature, Henry's law constant of argon is 1.4 $\times 10^{-3}$ mol/L·atm (714.28 L·atm/mol) with constant C of 1300. When the temperature increases to 50 ℃, Henry's law constant is down to 0.99 $\times 10^{-3}$ mol/L·atm (1010.1 L·atm/mol). For hydrogen, its C equals to 500, so the Henry's law constant value is down from 7.8 $\times 10^{-4}$ mol/L·atm (1282.05 L·atm/mol) to 6.9 $\times 10^{-4}$ mol/L·atm (1449.26 L·atm/mol). Thus, solubility of permanent gases usually decreases with increasing temperature.

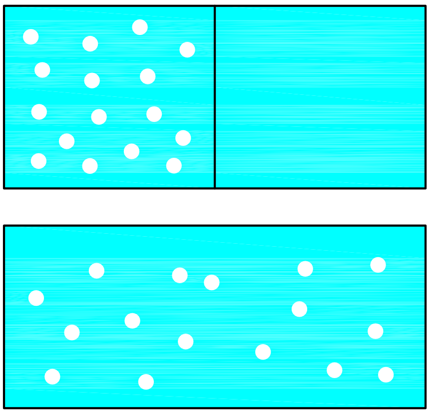

Figure 6.1: Illustration of molecule diffusion.

As illustrated in Figure 6.1, when a concentration gradient is produced, a transport of molecules of a certain dissolved species begins. It is based on the Brownian motion [Brown, 1828]. For steady-state, Fick's first law [Fick, 1855] describes the free diffusion in terms of concentration gradients as:

$$J = -D\frac{\partial C}{\partial x} \tag{6.4}$$

Here C is the volume concentration of the diffusing species (mol/m^3), x stands for the position (m), J is the diffusive flux (mol/m^2·s) and D (m^2/s) is the diffusion coefficient.

The negative sign ensures that the flux goes from the high to the low concentration regions. This concentration gradient can be the driving force for this reaction. The diffusion coefficient describes the velocity with which molecules of gas could diffuse into water phase.

Unsteady-state diffusion describes processes where the diffusion flux and the concentrations change with time t(s). Based on Fick's first law and the continuity equation for mass, Fick's second law [Fick, 1855] is derived as:

$$\frac{\partial C}{\partial t} = D\frac{\partial^2 C}{\partial^2 x} \tag{6.5}$$

When considering the diffusion of molecules in solutions, it is generally important to be able to estimate the time required for diffusion over a given distance. This knowledge can help us better understand how long it takes molecules to spread into the interstitial pore water. The evaluation of the characteristic time scales has been proposed following several mathematical descriptions. Since the diffusion coefficient predominantly controls the velocity of molecules and the mean time between collisions, in one-dimensional case, a basic expression which is also referred to as the Einstein's approximation equation indicates that the time scale t for a particle to move a distance x is given on the average by:

$$t \approx x^2/2D. \tag{6.6}$$

This rule shows that the diffusion time increases quadratically with the distance. Moreover, this equation can be improved by adding a numerical constant which depends on dimensionality.

D is a function of a number factors including molecular weight of the diffusing species, temperature, and viscosity of the medium in which diffusion occurs. Its value in liquids are lower by about four orders of magnitude than in dilute gases. They are mostly in the order of 10^{-9} m^2/s and depend only weakly on solute size [Gensterblum et al., 2015]. The well-known Stokes–Einstein equation is used to estimate the diffusion coefficient. Its value of a spherical particle of radius r in a fluid of dynamic viscosity η at absolute temperature T is given as:

$$D = \frac{RT}{6\pi N_a \eta r} \tag{6.7}$$

where R is the gas constant of 8.31 J$\cdot$ mol$^{-1}\cdot$K^{-1}. N_a is the Avogadro's number of 6.02×10^{23} mol^{-1}. Water dynamic viscosity is about 8.9×10^{-4} Pa·s at 25 °C and decreases to 5.4 $\times10^{-4}$ Pa·s at 50 °C [Kestin et al., 1978]. For argon, its atomic radii is 71 pm and for hydrogen, its value is 53 pm [Cotton et al., 1988]. Hence, argon gas diffusion coefficient in water is 3.46×10^{-9} m^2/s at 25 °C and increases to $6.17\ \times10^{-9}$ m^2/s at 50 °C. Hydrogen gas diffusion coefficient in water is 4.62×10^{-9} m^2/s at 25 °C and increases to $8.27\ \times10^{-9}$ m^2/s at 50 °C.

Ultimately, the ideal gas law $PV = nRT$ is an useful tool to approximate the behaviour of many gases under many conditions, although it has several limitations. This equation links the number of moles of gas n and its volume V under defined pressure and temperature conditions.

3 Scenario and numerical methods

3.1 Proposition of scenario "dissolution + diffusion + fillng"

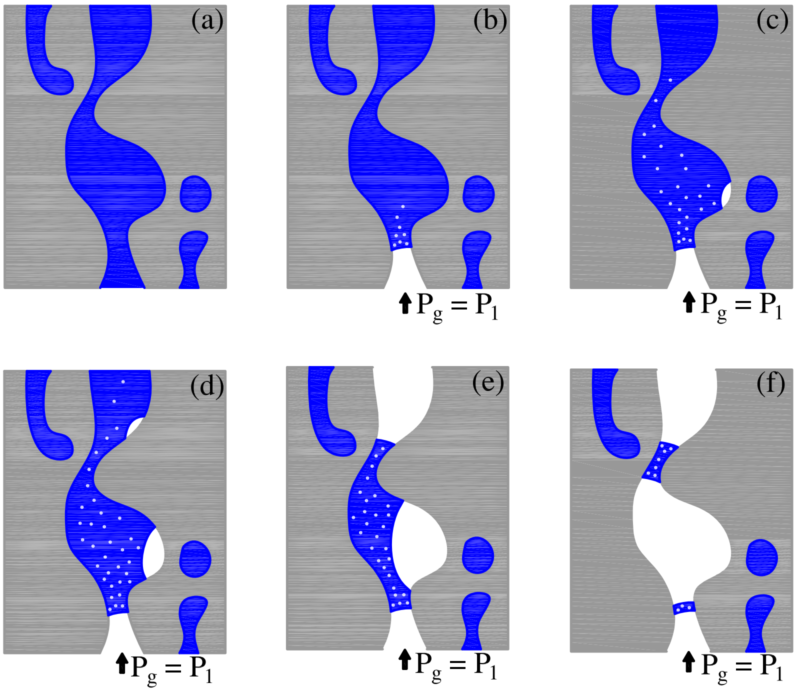

Figure 6.2: Illustration of the proposed scenario of "diffusion + filling".

This section mainly discusses the gas migration scenario with low gas pressure and long duration of experiment. In [Duveau et al., 2011], the breakthrough experiment performed in LML shows that after the impediment of gas phase movement, a drainage process is always in progress. Dissolved gas may probably accumulate in saturated pores and porewater will be squeezed out from the sample. This process is hereafter called as the dissolved gas filling effect. Due to the low efficiency of the flux of dissolved gas, gas filling may remain at an extremely low increase rate and require long periods to transport dissolved gas over distances. From this point of view, a low gas pressure can also ultimately lead to the gas leakage, not by the gas phase, but by the dissolved species.

It should be emphasized that this scenario is proposed based on phenomenological observations. Several assumptions are indispensably made for following researches. For instance, pores which could be filled by dissolved gas flux are defined as the large ones with lower capillary resistances than the applied gas pressure but they are isolated by the pore throat thus gas phase can not invade. As illustrated in Figure 6.2, image (a) is the initial saturated pore space. When a low gas pressure is applied and maintained for long period, dissolved gas molecules progressively diffuse in porewater, see image (b) and squeeze water in large pores separated by the pore throat then accumulate, see image (c). This process will subsequently take place in another large pores situated behind, see image (d). Dissolved gas breakthrough may happen during filling process along with the drained water. Finally, large pores will be totally filled and a partial saturated state of porous medium is obtained, see image (e) and (f).

3.2 Numerical point of view

According to the proposed scenario, the numerical method needs to be targeted at the extraction of drained pores, the calculation of diffusion distance and the measurement of filling volume. The defined morpho-mathematical operations such as opening and geodesic reconstruction are also used in this calculation. Considering the principles of these operations, the size of the smallest structuring element which can be applied in opening and geodesic reconstruction operations is equal to three voxels. Thus the real size of structuring element depends on the size of domain and the mesh resolution then determines the accuracy of results.

The calculation process is illustrated in Figure 6.3. At the onset, the geodesic reconstruction is applied on initial pore space (Figure 6.3(a)) considering the smallest structuring element, to detect connected pores outwards. Subsequently, the intersection between two inverse reconstructions provides interconnected pores as shown in Figure 6.3(b). The morphological opening is then performed by increasing the structuring element size while the gas pressure decreases. The filtered image is named as image 1 (Figure 6.3(c)) and the removed part is named as image 2 (Figure 6.3(d)). After these basic definitions, the geodesic reconstruction towards the downstream side is applied on image 1 to extract drained pores. Since pores with higher capillary forces than gas pressure have been effaced, geodesic reconstruction will stop at the pore throat where only dissolved species

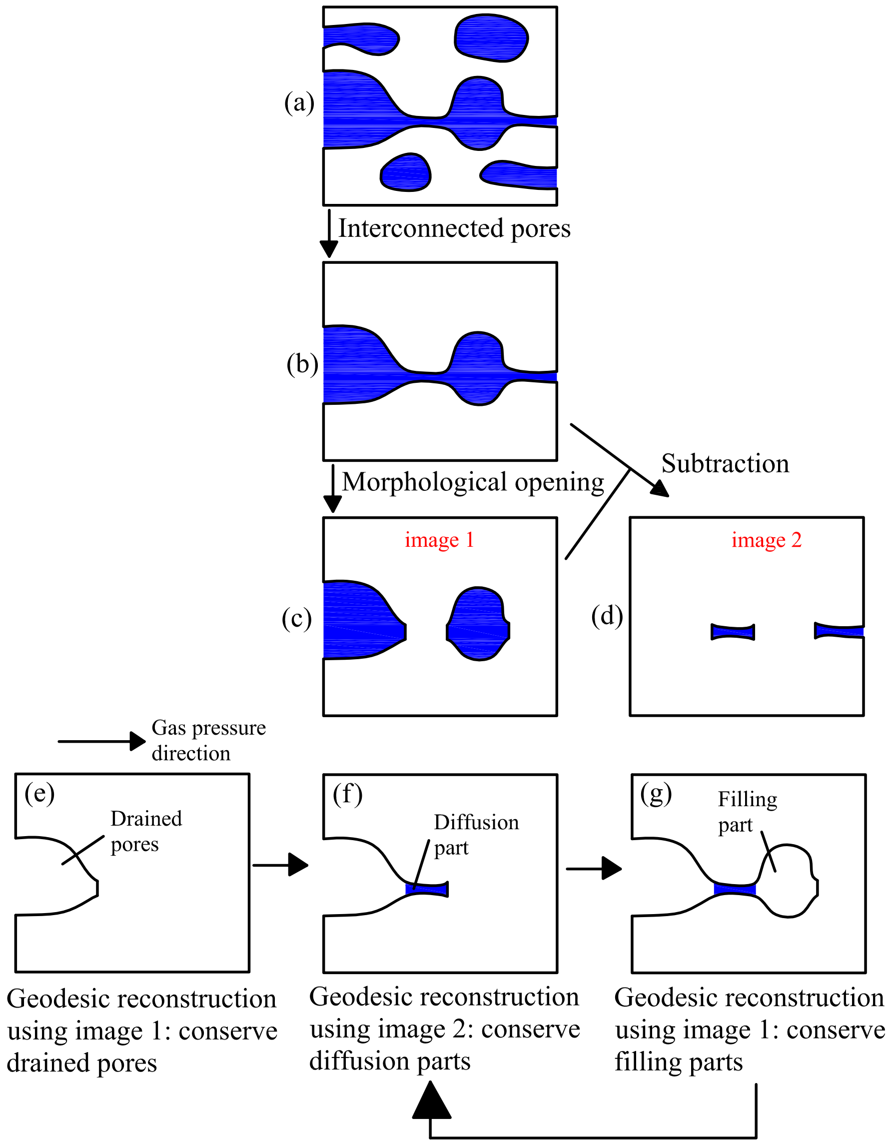

Figure 6.3: Proposed numerical method to calculate diffusion distance and filling volume.

could continue move forward (Figure 6.3(e)). Following this, by defining the obtained result as the marker image, a new geodesic reconstruction is then realized using image 2 as the mask image. In the same way, operation will end at the entrance of filling pore. The recorded step of geodesic dilation is referred to as the geodesic distance of the diffusion path between drained pore and the filling pore (Figure 6.3(f)). The next step is a same process only the mask image changes back to image 1. Hence, the geodesic distance and volume of filling part are provided respectively. In a complex pore space, steps in image (f) and image (g) are repeated alternatively until no additional parts could been conserved. Ultimately, the total diffusion distance, the diffusion distance between drained pore and filling part, the distances between two filling parts and the filling volumes are obtained and could be used for later researches. These different stages are computed by the following equations:

$$\text{Initial image} : M_0 \tag{6.8a}$$

$$\text{Interconnected pores} : M = R^{\oplus}(M_0) \cap R^{\ominus}(M_0) \neq 0 \tag{6.8b}$$

$$\text{Image1} : M_1 = M \circ E_i \tag{6.8c}$$

$$\text{Image2} : M_2 = M - M \circ E_i \tag{6.8d}$$

$$\text{Drained pores} : V_{\text{dr}} = R^{\oplus}(M_1) \tag{6.8e}$$

$$\text{Diffusion part} : V_{\text{dif}} = R^{\oplus}(V_{\text{dr}} + M_2) - V_{\text{dr}} \tag{6.8f}$$

$$\text{Filling part} : V_{\text{fil}} = R^{\oplus}(V_{\text{dif}} + M_1) - V_{\text{dr}} - V_{\text{dif}} \tag{6.8g}$$

4 Principle of calculation

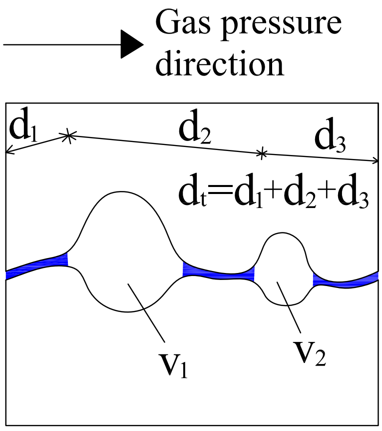

Figure 6.4: Principle of calculation for one cell.

It was introduced before that, from phenomenological observations, even under low gas pressure condition, gas leakage is possible through diffusion of dissolved species. In Table 6.1, downstream gas pressure was detected within an extremely low increasing rate before the breakthrough of gas phase by overcoming the capillary resistance of pore throat. The observed pressure changes at the upstream side were due to diffusive transport across the water-saturated pore space of the samples. Moreover, the corresponding time for the record of dissolved gas presence reduces during the pressure loading process (at a rate of 1 to 10 days between two ΔP gas =0.5 MPa steps). In order to verify the feasibility of

Table 6.1: Results of gas breakthrough experiment on COx argillite samples in [Duveau et al., 2011]. The values in bold represent the corresponding gas breakthrough pressures and duration at the moment of measuring gas presence on the downstream side.

Sample n.	h (mm)	P_c (MPa)	P_{gas} (MPa) Up-stream	Duration (h)	P_{gas} (MPa) Down-stream	Gas?
1	10	5	0.2	48	0.0015	No
			0.7		0.007	
			0.98		0.009	
			1.35	24	0.0065	Doubt
			1.4	48	0.0144	
			1.65	**1**	**0.01**	**Yes**
		12	1.5	48	0.005	No
			1.8	**1**	**>0.01**	**Yes**
2	20	5	1.45	72	0.0011	No
			2	72	0.002	Doubt
			2.5	96	0.003	
			3	**1**	**0.004**	**Yes**
		12	2	96	0.0042	No
			2.5		**0.0038**	Yes
			3		0.0033	
			3.5	72	0.0071	
			4		0.0145	
3	10	5	0.5	72	0.0032	No
			0.88		0.0045	
			1.26		**0.012**	**Yes**

proposed scenario, the estimation of duration for dissolved gas reaches the downstream side is indispensable. Results should show a rapid increasing trend of time with the decrease of applied pressure. In addition, it should be noted that, the following principle of calculation is defined based on several assumptions for the purpose of simplification. The most important one is that: the real sample is composed of same cells of 5 µm which is simulated through union of excursions. The proposed principle for one cell is shown in Figure 6.4.

V_1 and V_2 are two pores for filling. The beginning of this process is assumed when the first dissolved gas molecule travels to the entrance of the filling part. Based on the diffusion time rule and the hypothesis of one-dimensional diffusion, the starting time of filling for V_1 and V_2 are t_{0,V_1} and t_{0,V_2} respectively. They are determined by the diffusion distance of d_1 and $d_1 + d_2$ respectively and could be computed as:

$$t_{0,V_1} = \frac{d_1^2}{2 \cdot D} \tag{6.9a}$$

$$t_{0,V_2} = \frac{(d_1 + d_2)^2}{2 \cdot D} \tag{6.9b}$$

For the purpose of simplification, diffusion is supposed to be stead type. Time brings no influence to the diffusion flux. In reality, due to concentration gradient decrease, diffusion flux will become weaker then increase the corresponding required filling time. For V_1 and V_2, filling time are denoted as t_{f,V_1} and t_{f,V_2} respectively. The injection diffusion flux is a function of concentration gradient which are denoted as J_{V_1} for V_1 and J_{V_2} for V_2. Subsequently, following the ideal gas law, t_{f,V_1} and t_{f,V_2} are given as:

$$t_{f,V_1} = \frac{P_g \cdot V_1}{RTS_i J_{V_1}} \tag{6.10a}$$

$$t_{f,V_2} = \frac{P_g \cdot V_2}{RTS_i J_{V_2}} \tag{6.10b}$$

where S_i stands for the surface of the entrance of filling part. Since the pathway connectivity is ended by morphological opening, the value of S_i can be seen as the size of used structuring element. Moreover, in a small cell of 5 µm, geodesic distance between two filling parts is extremely short. Variables of distance could be considered as constants in this case. As a result, all of the filling processes in the considering cell are supposed to be simultaneous, thus leads to $t_{0,V_1} \approx t_{0,V_2}$. For the same reason, the difference between injection diffusion fluxes is not evident thus $J_{V_1} \approx J_{V_2}$. Ultimately, the required filling time is determined by its volume. For $V_1 > V_2$, t_{f,V_1} will be longer than t_{f,V_2}. The starting time of filling $t_{0,1}$ of this cell then equals to t_{o,V_1}. The total filling time $t_{f,1}$ is then defined as the corresponding duration for filling the largest pore and the total filling volume $V_{f,1}$ is the sum. They are given as:

$$t_{0,1} = t_{0,V_1} = \frac{d_1^2}{2 \cdot D} \tag{6.11a}$$

$$t_{f,1} = \frac{P_g \cdot V_1}{RTS_i J_1} = \frac{P_g \cdot V_1}{RTS_i J_{V_1}} \tag{6.11b}$$

$$V_{f,1} = V_1 + V_2 \tag{6.11c}$$

Considering that two cells with identical morphological pore space are connected, morphological opening then provides same diffusion pathways and filling parts. A simple illustration is presented in Figure 6.5 with interconnected diffusion path between the two cells. Hence, the starting time of filling in cell 2 is denoted as $t_{0,2}$ and the corresponding

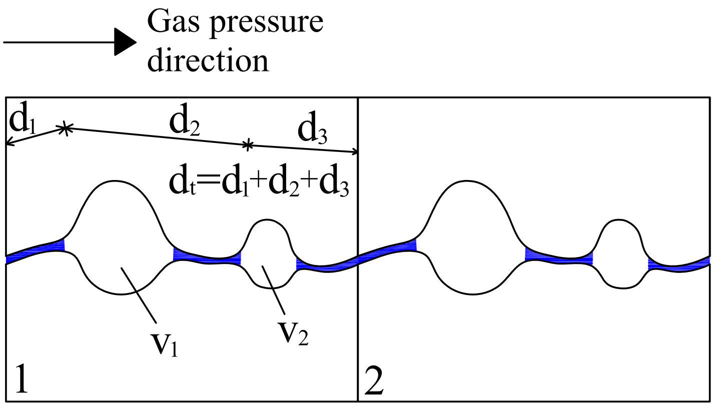

Figure 6.5: Principle of calculation for two cells.

filling time is $t_{f,2}$. They could be computed as:

$$t_{0,2} = \frac{(d_1 + d_t)^2}{2 \cdot D} \tag{6.12a}$$

$$t_{f,2} = \frac{P_g \cdot V_1}{RTS_i J_2} \tag{6.12b}$$

Subsequently, the difference between the required filling time for the two cells Δt and the total filling volume of this system $V_{f,2}$ could be obtained as:

$$\Delta t = t_{f,2} - t_{f,1} = \frac{P_g \cdot V_1}{RTS_i J_2} - \frac{P_g \cdot V_1}{RTS_i J_1} \tag{6.13a}$$

$$V_{f,2} = 2(V_1 + V_2) \tag{6.13b}$$

The total filling time $t_{t,2}$ for this system of two cells can be defined as the sum of the filling time for cell 1, the differences between the starting time of filling and between the required filling time for each cell. Thus it can be written as:

$$t_{t,2} = t_{f,1} + \Delta t + (t_{0,2} - t_{0,1}) \approx t_{f,1} + \Delta t + \frac{d_t^2}{2 \cdot D} \tag{6.14}$$

In the case of n cells connected as shown in Figure 6.6. For the nth cell, its starting time of filling $t_{0,n}$ and required filling time $t_{f,n}$ could be derived following the same method as:

$$t_{0,n} \approx \frac{(n \cdot d_t)^2}{2 \cdot D} \tag{6.15a}$$

$$t_{f,n} = \frac{P_g \cdot V_1}{RTS_i J_n} = t_{f,1} + n \cdot \Delta t \tag{6.15b}$$

Hence, for the system, the total filling time $t_{t,n}$ and the total filling volume $V_{f,n}$ are

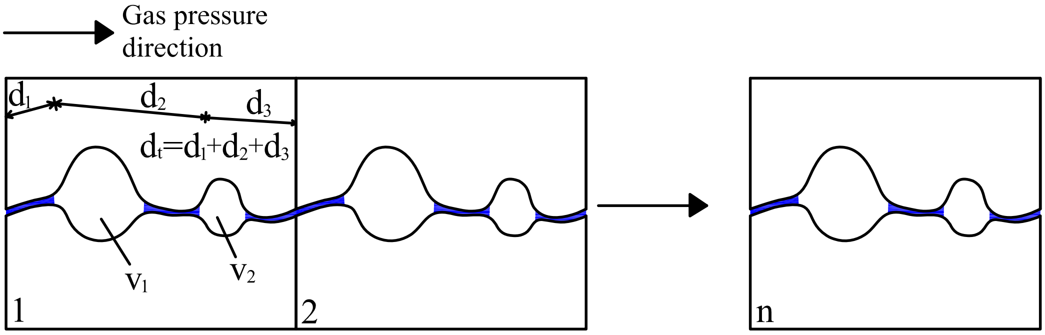

Figure 6.6: Principle of calculation for n cells.

obtained as:

$$t_{t,n} = t_{f,1} + n \cdot \Delta t + \frac{(n \cdot d_t)^2}{2 \cdot D} \tag{6.16a}$$

$$V_{f,n} = n(V_1 + V_2) \tag{6.16b}$$

Following this scenario, filling process can be considered as a potential drainage process. In addition to the diffusion, dissolved gas molecules are also driven by the drainage water flow thus the migration speed towards the downstream side is accelerated. Finally, the breakthrough is accomplished when the first dissolved molecule leaks out of sample. In view of the different volumes of filling parts and the starting time lags of filling for pores located behind, at the instant of breakthrough, pore space is partially drained and illustrated in Figure 6.7. Furthermore, the total distance travelled for a gas molecule until breakthrough is the sum of diffusion distance and drainage water transport distance (approximately equals to V_f/S_i). Based on this idea and the obtained equations, an equations set is then provided to determine the dissolved gas breakthrough time for a real sample:

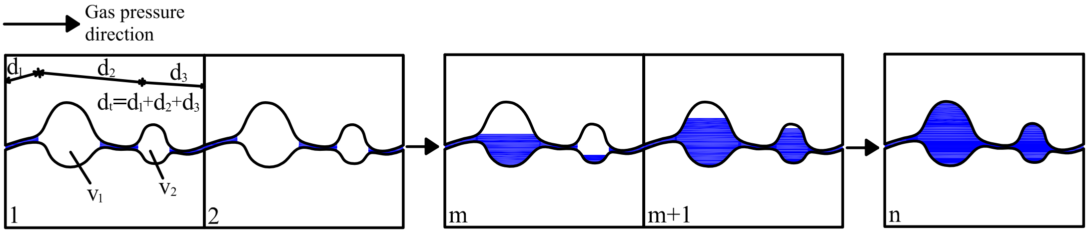

Figure 6.7: Illustration of pore space saturation at the instant of dissolved gas breakthrough.

$$V_{f,n}/S_i + \sqrt{2 \cdot D \cdot t_{t,n}} = L \tag{6.17a}$$

$$t_{t,n} = t_{f,1} + n \cdot \Delta t + \frac{(n \cdot d_t)^2}{2 \cdot D} \tag{6.17b}$$

where L represents the total gas molecule migration distance which is influenced by the real sample size. $V_{f,n}$ is defined as the filling volume in totally drained cell. For the purpose of simplification, the partially drained cells are negligible. In this way, the required time for dissolved gas molecule breakthrough in this proposed scenario can be obtained by knowing the morphological information of the basic cell of 5 µm. Although this calculation principle is built based on several assumptions and simplifications, it can still be used to roughly estimate the variation of molecule breakthrough time with decreasing gas pressure lower than gas entry pressure. The application on COx argillite model will be introduced in the next section.

5 Results and discussion

In chapter 3 and 4, several morphological models of the pore network in COx argillite are generated considering different experimental pore size distributions (Model 1 for WA, Model 2 for NMR, Model 3 for MIP). Particularly, Model 1 and Model 2 show better accordance with the experimental breakthrough pressure following the capillary two-phase flow mechanism. The application of the proposed "diffusion + filling" scenario is performed on Model 1 to investigate the duration for dissolved gas breakthrough at low gas pressure condition.

At the onset, morphological information of Model 1 needs to be totally obtained. After the selection of interconnected gas flow pathways, a sequence of morphological opening with increasing size of the structuring element is applied to break the connectivity thus the tradition capillary two-phase flow scenario is no longer suitable. Subsequently, using the mentioned technique in section 4, the total diffusion distance, the diffusion distance between drained pore and filling part, the distances between two filling parts and the filling volumes are obtained. The real sample size is then defined as closed as the experimental level (10 mm, 20 mm, 50 mm). The used gas is defined as argon. When temperature is fixed at 25 °C, Henry's law constant of argon is 1.4×10^{-3} mol/L·atm (714.28 L·atm/mol) and diffusion coefficient is 3.46×10^{-9} m^2/s. Results are presented in Figure 6.8. It is obvious that sample size is a predominant factor to control dissolved gas breakthrough time. For sample of 10 mm, breakthrough time sharply increases when gas pressure is down to about 1 MPa and reaches about 35 h with $P_g = 0.5$ MPa. For sample of 20 mm, the quickly increasing instant appears at about 1.5 MPa and time finally attains about 150 h. For sample of 50 mm, breakthrough time smoothly increases during the pressure decreasing process from 6.5 MPa down to 2 MPa, then sharply increases to about 525 h. In [Duveau et al., 2011], sample height has been proved influential to the breakthrough pressure: the value ranges from 1.26 up to 1.8 MPa for sample of 10 mm, whereas it is of 2.5 - 3 MPa for sample of 20 mm. The simulated pressures which lead to sharply increasing breakthrough time in this section are about 1 MPa, 1.5 MPa, 2 MPa, respectively for sample of 10 mm, 20 mm and 50 mm. These values are more likely to reflect the breakthrough threshold of dissolved gas when gas pressure remains at low level. When these thresholds are passed, the quick drops of time make it easier for gas molecules to reach the downstream side. Thus, the detection of gas presence at the downstream side can be more affirmative.

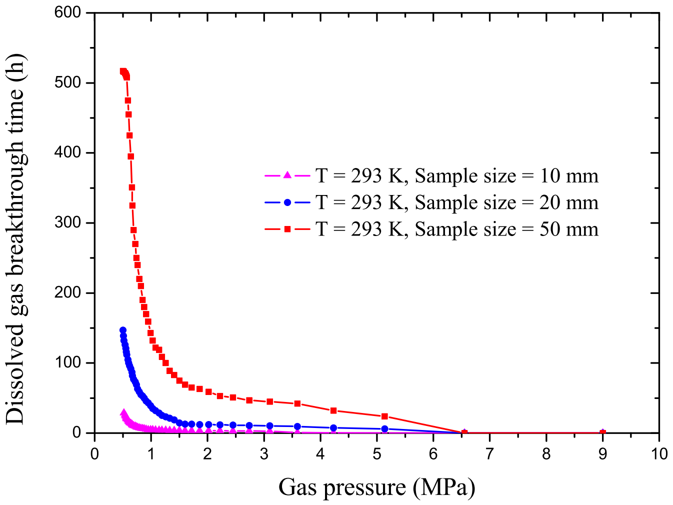

Figure 6.8: Simulated dissolved argon gas breakthrough time considering different sample sizes (COx argillite, Model 1, X+ direction).

In addition, temperature variation is an important issue since it may change several parameters. Assuming that temperature increases to 50 ℃, Henry's law constant will be down to 0.99 $\times 10^{-3}$ mol/L·atm (1010.1 L·atm/mol) and diffusion coefficient will increase to 6.17 $\times 10^{-9}$ m^2/s. It means that the amount of dissolved gas reduces, thus the concentration gradient decreases and consequently weakens the diffusion flux. At the mean time, the thermal motion of particles are enhanced thus the diffusion velocity becomes more significant. Moreover, surface tension drops from $71.99 \times 10^{-3} N/m$ to $67.94 \times 10^{-3} N/m$ thus the gas phase breakthrough pressure is down to 4 - 6.18 MPa. Considering these effect, a comparison of dissolved argon gas breakthrough time in COx argillite model between T = 25 ℃ and 50 ℃ is made in Figure 6.9. Results show that even the sharply increasing point of about 2 MPa does not change, the corresponding dissolved gas breakthrough time decreases. In other words, temperature increase can reduce the required duration for gas presence at the downstream side.

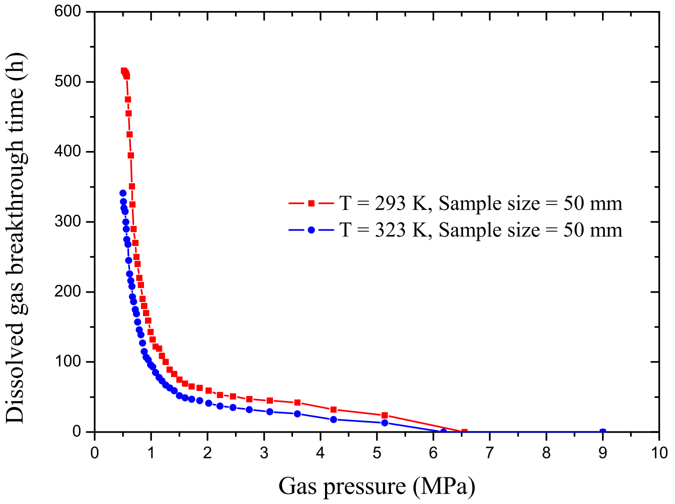

Figure 6.9: Simulated dissolved argon gas breakthrough time considering different temperatures (COx argillite, Model 1, X+ direction).

Once again, the proposed scenario is based on phenomenological observations. The mentioned mechanism consists several uncertainties and perhaps does not really exist. The simulated dissolved gas breakthrough time may differ from the true value because of the simplifications made in the calculation principle. However, both of numerical and experimental results show the same changing behaviour with low gas pressure. More detailed theoretical analysis and experimental evaluations are indispensable to enhance this proposed scenario.

6 Conclusions

In this chapter, gas migration scenario is no longer limited by the capillary effect. The dissolved gas may also lead to leakage at low gas pressures. The two principal migration modes of dissolved molecules are the diffusion and the convection with interstitial water drainage. Since at low gas pressure, the second mechanism is restricted, thus diffusion becomes a prominent transport process. Moreover, dissolved gas is limited in water phase that means the breakthrough must be performed during a water leakage process. Based on this idea, the "diffusion + filling" scenario is proposed.

Following this, several basic theories such as the Henry's law, the Fick's law, the diffusion time rule and the ideal gas law are presented. Temperature-dependent parameters such as the Henry's constant and the diffusion coefficient are interpreted.

The numerical method is proposed using morpho-mathematical operations such as the morphological opening and the geodesic reconstruction. Morphological information of model such as the total diffusion distance, the diffusion distance between drained pore and filling part, the distances between two filling parts and the filling volumes could be obtained for further research.

The calculation principle is defined based on several assumptions for the purpose of simplification. The proposed equations set can be used to determine the dissolved gas breakthrough time for a real sample. The required parameters could be obtained from the basic cell of 5 µm using the numerical technique.

According to the application on COx argillite model, sample size is the key parameter to determine the dissolved gas breakthrough time. For the three samples of 10 mm, 20 mm and 50 mm, the points of sharply increasing time are located at 1 MPa, 1.5 MPa and 2 MPa respectively. They are more likely to reflect the breakthrough threshold of dissolved molecules at low gas pressure. In addition, temperature increase may not be able to change the breakthrough threshold but can influence the corresponding time. It can accelerate the leakage speed.

Since this scenario is based on phenomenological observation and the proposed technique includes several assumptions and simplifications, more detailed theoretical analysis and experimental evaluations are required to provides more accurate description of gas transport mechanism at low gas pressure.

Chapter 7

Conclusions and perspectives

This thesis has been mainly dedicated to: 1. the morphological modelling of porous space in COx argillite considering different experimental pore size distributions. The basic method used is the excursion set theory on Gaussian Random Field; 2. the simulation of gas (produced by humid corrosion of metallic parts) breakthrough and imbibition processes in order to numerically evaluate its repository performance; 3, the applications on another potential host rocks in the context of radioactive waste repository such as the Opalinus clay and the Boom clay; 4, the proposition and simulation of gas migration scenario at low gas pressure (“diffusion + filling).

During the long-term repository, gas phase may probably generate and contact with the host formation, according to various conditions. The main sources involve the corrosion of metallic parts, the degassing process, the radioactive waste decay and the water radiolysis. Gas migration mechanisms in low-permeable formation include the advective and diffusive transport of dissolved gas in water phase, the capillary two phase flow, through the pathway dilation and through the fractures. During the gas generation process, gas pressure may increase notably. Whenever the capillary threshold for gas passage is reached, hydrogen gas leakage may occur through the whole structure. If this process can not be ensured, the increasing gas pressure may damage the repository formation. The aim of this modelling work is to investigate the gas migration properties for performance and safety assessment purposes. In chapter 2, a detailed introduction of this context has been given. In addition, interconnected pores are the key factor to control the fluid permeability. In order to simulate the pore space, the pore size distribution is an indispensable characteristic. Several experimental methods provide data about it such as WA/WD method, NMR method, MIP method or FIB method.

Essentially, the complexity of gas migration properties in low permeable rock is derived from the complex aspect of pore space. In chapter 3, regarding the construction of pore space morphological model without using assumed objects, excursion set on Gaussian random field transforms a continuous field to a binary one, thus is capable to represent the two phases (pores and matrix). Moreover, union of independent excursions enlarges the pore size range and then is capable to provide a realistic model in good accordance with the experimental pore size distribution. However, the lack of capacity to involve the natural properties of rock may influence the accuracy of simulation. Hence, a complete real model of sample derived from imagining methods is always a good alternative.

In chapter 4, The proposed scenario for the description of gas movement is no longer limited by fluid mechanics or macroscopic approaches. It is more original and is based on purely geometric analysis on the porous network using morpho-mathematical operations. Considering the initial divergences among experimental pore size distributions due to different measuring techniques, three models (Model 1: WA; Model 2: NMR; Model 3: MIP) within a same total porosity are generated. Model 1 provides the gas entry pressure between 2.18 - 3.06 MPa and the breakthrough pressure between 4.24 - 6.55 MPa which are similar to measured values. This model enhances the idea that the capillary-induced gas breakthrough is possible in COx argillite formation at gas pressure lower than the fracture threshold. In Model 2, the proportion of medium pores is relatively higher thus the obtained results are slightly higher. In Model 3, the proportion of small pores is overestimated due to the ink-bottle effect. As a result, the breakthrough pressure is sharply increasing. These observations match our initial expectations: under a same total porosity, the size of entry and breakthrough pore throats in models with high proportion of small pores are bound to be small thus lead to high entry and breakthrough pressures. Moreover, unlike the breakthrough pressure, the gas entry pressure highly depends on the spatial position of the entry pore throat. Different upstream sides or orientations may bring different cases. Besides, results of the extension on the Opalinus clay and the Boom clay are also in consistence with experimental observations. Thus, it can be concluded that the proposed scenario seems quite general for different types of porous media and can be used to predict the gas transport properties.

In addition, after breakthrough, gas leaks through the repository formation and consequently reduces the gas pressure at the generation source. Water imbibition then starts. Chapter 5 mainly concerns about the simulation of this process. As an inverse process of drainage, water imbibition can gradually close the interconnected gas pathways. The gas shut-off pressure which corresponds to the gas impermeable state is targeted lower than the gas breakthrough pressure. More interestingly, isolated pores may produce during this process then result in a residual gas saturation when the applied gas pressure is finally removed. The numerical investigation of imbibition process is performed through a combination of several morphological operations such as morphological opening, geodesic reconstruction, union of excursion and binary subtraction. Results prove the existence of isolated pores. The obtained gas shut-off pressures are in good accordance with experimental values and are always lower than gas breakthrough pressures. The final gas residual saturation is estimated.

Chapter 6 focuses on the gas migration mechanism with low gas pressure. Some phenomenological observations show that dissolved gas migration plays an important role in the gas transport process when gas pressure remains at a low level. Since the dissolved gas is limited in porewater, the breakthrough of dissolved gas is essentially based on the porewater transport. That means after the impediment of the gas phase movement, a drainage process is always in progress. The dissolved gas may probably accumulate in the saturated pores and porewater will be squeezed out from the sample. Based on this idea, the scenario of "diffusion + filling" has been proposed. The numerical investigation is also accomplished by using a combination of morphological operations. The calculation principle is built based on several assumptions and simplifications. Even the numerical results show good changing behaviours, more detailed theoretical analysis and experimental investigations are indispensable to accurately describe the gas transport properties at low gas pressures.

An improvement of this work can be made by adding stress - strain state analysis and damage or fracture models when considering materials with relatively higher proportion of small pores. In this case, the generation of fractures may increase the equivalent porosity and then bring influences to the breakthrough and imbibition processes. Furthermore, a reliable stress - strain model provides information about the influence to the breakthrough process with changes in pore pressure and confining pressure. Due to the randomly shaped and positioned pore space, this amelioration will be very challenging.

Bibliography

[Adler, 2008] Adler, R. J. (2008). Some new random field tools for spatial analysis. *Stochastic Environmental Research and Risk Assessment*, 22(6):809–822.

[Andra, 2005] Andra (2005). Tome évolution phénoménologue du stockage géologique. Technical Report 2005a, Andra (Agence Nationale pour la Gestion des Déchets Nucléaires).

[Andra, 2009a] Andra (2009a). Référentiel du site meuse/ haute marne. Technical Report C-RP-ADSM-09-0002, Andra (Agence Nationale pour la Gestion des Déchets Nucléaires).

[Andra, 2009b] Andra (2009b). Référentiel du site meuse/ haute marne. Technical Report C-RP-ADS-09-0007, Andra (Agence Nationale pour la Gestion des Déchets Nucléaires).

[Bear, 2013] Bear, J. (2013). *Dynamics of fluids in porous media.* Courier Corporation.

[Bernabe, 1987] Bernabe, Y. (1987). The effective pressure law for permeability during pore pressure and confining pressure cycling of several crystalline rocks. *Journal of Geophysical Research: Solid Earth*, 92(B1):649–657.

[Berryman, 1992] Berryman, J. G. (1992). Effective stress for transport properties of inhomogeneous porous rock. *Journal of Geophysical Research: Solid Earth*, 97(B12):17409–17424.

[Bezrukov et al., 2002] Bezrukov, A., Bargieł, M., and Stoyan, D. (2002). Statistical analysis of simulated random packings of spheres. *Particle & Particle Systems Characterization*, 19(2):111–118.

[Bezrukov and Stoyan, 2006] Bezrukov, A. and Stoyan, D. (2006). Simulation and statistical analysis of random packings of ellipsoids. *Particle & Particle Systems Characterization*, 23(5):388–398.

[Biot and Willis, 1957] Biot, M. and Willis, D. (1957). The theory of consolidation. *J. Appl Elastic Coefficients of the Mech*, 24:594–601.

[Biot, 1941] Biot, M. A. (1941). General theory of three-dimensional consolidation. *Journal of applied physics*, 12(2):155–164.

[Bossart and Thury, 2007] Bossart, P. and Thury, M. (2007). Research in the mont terri rock laboratory: quo vadis? *Physics and Chemistry of the Earth, Parts A/B/C*, 32(1):19–31.

[Boulin, 2008] Boulin, P. (2008). *Expérimentation et modélisation du transfert d'hydrogène à travers des argiles de centre de stockage de déchets radioactifs*. PhD thesis, Institut National Polytechnique de Grenoble-INPG.

[Brown, 1828] Brown, R. (1828). Xxvii. a brief account of microscopical observations made in the months of june, july and august 1827, on the particles contained in the pollen of plants; and on the general existence of active molecules in organic and inorganic bodies. *Philosophical Magazine Series 2*, 4(21):161–173.

[Carle and Patarin, 2003] Carle, R. and Patarin, L. (2003). Les déchets radioactifs: un problème résolu? *Revue générale nucléaire*, (1):74–74.

[Chen et al., 1999] Chen, J., Hopmans, J., and Grismer, M. (1999). Parameter estimation of two-fluid capillary pressure–saturation and permeability functions. *Advances in Water Resources*, 22(5):479–493.

[Coll, 2005] Coll, C. (2005). *Endommagement des roches argileuses et perméabilité induite au voisinage d'ouvrages souterrains*. PhD thesis, Université Joseph-Fourier-Grenoble I.

[Cotton et al., 1988] Cotton, F. A., Wilkinson, G., et al. (1988). *Advanced inorganic chemistry*, volume 594. Wiley New York.

[Coussy, 2004] Coussy, O. (2004). *Poromechanics*. John Wiley & Sons.

[Davy et al., 2009] Davy, C. A., Skoczylas, F., Lebon, P., and Dubois, T. (2009). Gas migration properties through a bentonite/argillite interface. *Applied Clay Science*, 42(3):639–648.

[Dougherty, 1992] Dougherty, E. R. (1992). An introduction to morphological image processing. *Tutorial texts in optical engineering*.

[Duveau et al., 2011] Duveau, G., M'Jahad, S., Davy, C., Skoczylas, F., Shao, J., Talandier, J., and Granet, S. (2011). Gas entry through water-saturated argillite: experimental and numerical approaches. In *45th US Rock Mechanics/Geomechanics Symposium*. American Rock Mechanics Association.

[Federer, 1959] Federer, H. (1959). Curvature measures. *Transactions of the American Mathematical Society*, 93(3):418–491.

[Fick, 1855] Fick, A. (1855). Ueber diffusion. *Annalen der Physik*, 170(1):59–86.

[Fouché et al., 2004] Fouché, O., Wright, H., Le Cléac'h, J.-M., and Pellenard, P. (2004). Fabric control on strain and rupture of heterogeneous shale samples by using a non-conventional mechanical test. *Applied Clay Science*, 26(1):367–387.

[Gallé, 2000] Gallé, C. (2000). Gas breakthrough pressure in compacted fo–ca clay and interfacial gas overpressure in waste disposal context. *Applied clay science*, 17(1):85–97.

[Gallé and Tanai, 1998] Gallé, C. and Tanai, K. (1998). Evaluation of gas transport properties of backfill materials for waste disposal: H2 migration experiments in compacted fo-ca clay. *Clays and Clay Minerals*, 46(5):498–508.

[Gangi, 1978] Gangi, A. F. (1978). Variation of whole and fractured porous rock permeability with confining pressure. In *International Journal of Rock Mechanics and Mining Sciences & Geomechanics Abstracts*, volume 15, pages 249–257. Elsevier.

[Gensterblum et al., 2015] Gensterblum, Y., Ghanizadeh, A., Cuss, R. J., Amann-Hildenbrand, A., Krooss, B. M., Clarkson, C. R., Harrington, J. F., and Zoback, M. D. (2015). Gas transport and storage capacity in shale gas reservoirs–a review. part a: Transport processes. *Journal of Unconventional Oil and Gas Resources*, 12:87–122.

[Gerard et al., 2008] Gerard, P., Charlier, R., Barnichon, J.-D., Su, K., Shao, J.-F., Duveau, G., Giot, R., Chavant, C., and Collin, F. (2008). Numerical modelling of coupled mechanics and gas transfer around radioactive waste in long-term storage. *Journal of theoretical and applied mechanics*, 38(1-2):25–44.

[Gerard et al., 2014] Gerard, P., Harrington, J., Charlier, R., and Collin, F. (2014). Modelling of localised gas preferential pathways in claystone. *International journal of rock mechanics and mining sciences*, 67:104–114.

[Glasbey and Horgan, 1995] Glasbey, C. A. and Horgan, G. W. (1995). *Image analysis for the biological sciences*, volume 1. Wiley Chichester.

[Hemes et al., 2013] Hemes, S., Desbois, G., Urai, J., De Craen, M., and Honty, M. (2013). Variations in the morphology of porosity in the boom clay formation: insights from 2d high resolution bib-sem imaging and mercury injection porosimetry. *Netherlands Journal of geosciences*, 92(04):275–300.

[Hemes et al., 2015] Hemes, S., Desbois, G., Urai, J. L., Schröppel, B., and Schwarz, J.-O. (2015). Multi-scale characterization of porosity in boom clay (hades-level, mol, belgium) using a combination of x-ray μ-ct, 2d bib-sem and fib-sem tomography. *Microporous and Mesoporous Materials*, 208:1–20.

[Henry, 1803] Henry, W. (1803). Experiments on the quantity of gases absorbed by water, at different temperatures, and under different pressures. *Philosophical Transactions of the Royal Society of London*, 93:29–276.

[Hildenbrand et al., 2002a] Hildenbrand, A., Schloemer, S., and Krooss, B. (2002a). N2 and co2 gas breakthrough experiments on fine-grained sediments. *Poromechanics (eds Auriault JL, Geindereau C, Royer P, Bloch JF, Boutin C, Lewandourska J)*, pages 445–50.

[Hildenbrand et al., 2002b] Hildenbrand, A., Schlömer, S., and Krooss, B. (2002b). Gas breakthrough experiments on fine-grained sedimentary rocks. *Geofluids*, 2(1):3–23.

[Hildenbrand et al., 2004] Hildenbrand, A., Schlömer, S., Krooss, B., and Littke, R. (2004). Gas breakthrough experiments on pelitic rocks: comparative study with n2, co2 and ch4. *Geofluids*, 4(1):61–80.

[Horseman et al., 1999] Horseman, S., Harrington, J., and Sellin, P. (1999). Gas migration in clay barriers. *Engineering geology*, 54(1):139–149.

[Horseman et al., 1996] Horseman, S., Higgo, J., Alexander, J., and Harrington, J. (1996). Water, gas and solute movement through argillaceous media. *Nuclear Energy Agency Rep. CC-96/1. OECD, Paris.*

[Horseman and Volckaert, 1996] Horseman, S. and Volckaert, G. (1996). Disposal of radioactive wastes in argillaceous formations. *Geological Society, London, Engineering Geology Special Publications*, 11(1):179–191.

[Hosseini, 2015] Hosseini, M. (2015). *Numerical simulation of hydro-mechanical behaviour of nano porous materials: Application to cement paste.* PhD thesis, Université de Lille.

[Houben et al., 2014] Houben, M., Desbois, G., and Urai, J. (2014). A comparative study of representative 2d microstructures in shaly and sandy facies of opalinus clay (mont terri, switzerland) inferred form bib-sem and mip methods. *Marine and Petroleum Geology*, 49:143–161.

[Ibrahim et al., 1970] Ibrahim, M. A., Tek, M. R., and Katz, D. L. V. (1970). *Threshold pressure in gas storage.* American Gas Association.

[Ito et al., 2011] Ito, D., Akaku, K., Okabe, T., Takahashi, T., and Tsuji, T. (2011). Measurement of threshold capillary pressure for seal rocks using the step-by-step approach and the residual pressure approach. *Energy Procedia*, 4:5211–5218.

[Jacops et al., 2013] Jacops, E., Volckaert, G., Maes, N., Weetjens, E., and Govaerts, J. (2013). Determination of gas diffusion coefficients in saturated porous media: He and ch 4 diffusion in boom clay. *Applied Clay Science*, 83:217–223.

[Jacops et al., 2015] Jacops, E., Wouters, K., Volckaert, G., Moors, H., Maes, N., Bruggeman, C., Swennen, R., and Littke, R. (2015). Measuring the effective diffusion coefficient of dissolved hydrogen in saturated boom clay. *Applied Geochemistry*, 61:175–184.

[Keller et al., 2011] Keller, L. M., Holzer, L., Wepf, R., and Gasser, P. (2011). 3d geometry and topology of pore pathways in opalinus clay: Implications for mass transport. *Applied Clay Science*, 52(1):85–95.

[Kestin et al., 1978] Kestin, J., Sokolov, M., and Wakeham, W. A. (1978). Viscosity of liquid water in the range- 8 c to 150 c. *Journal of Physical and Chemical Reference Data*, 7(3):941–948.

[Kutchko et al., 2007] Kutchko, B. G., Strazisar, B. R., Dzombak, D. A., Lowry, G. V., and Thaulow, N. (2007). Degradation of well cement by co2 under geologic sequestration conditions. *Environmental science & technology*, 41(13):4787–4792.

[Kutchko et al., 2008] Kutchko, B. G., Strazisar, B. R., Lowry, G. V., Dzombak, D. A., and Thaulow, N. (2008). Rate of co2 attack on hydrated class h well cement under geologic sequestration conditions. *Environmental science & technology*, 42(16):6237–6242.

[Kwon et al., 2001] Kwon, O., Kronenberg, A. K., Gangi, A. F., and Johnson, B. (2001). Permeability of wilcox shale and its effective pressure law. *Journal of Geophysical Research: Solid Earth*, 106(B9):19339–19353.

[Le et al., 2008] Le, T., Delage, P., Cui, Y., Tang, A., Lima, A., Romero, E., Gens, A., and Li, X. L. (2008). Water retention properties of boom clay: A comparison between different experimental techniques. In *Proc. 1st Eur. Conf. on Unsaturated Soils*, pages 229–234.

[Li et al., 2009] Li, M., Bernabé, Y., Xiao, W.-I., Chen, Z.-Y., and Liu, Z.-Q. (2009). Effective pressure law for permeability of e-bei sandstones. *Journal of Geophysical Research: Solid Earth*, 114(B7).

[Lima et al., 2012] Lima, A., Romero, E., Piña, Y., Gens, A., and Li, X. (2012). Water retention properties of two deep belgian clay formations. In *Unsaturated Soils: Research and Applications*, pages 179–184. Springer.

[Lowden et al., 1998] Lowden, B. D., Porter, M. J., Powrie, L. S., et al. (1998). T2 relaxation time versus mercury injection capillary pressure: Implications for nmr logging and reservoir characterisation. In *European Petroleum Conference*. Society of Petroleum Engineers.

[Maes et al., 2004] Maes, N., Wang, L., Delécaut, G., Beauwens, T., Van Geet, M., Put, M., Weetjens, E., Marivoet, J., Van der Lee, J., Warwick, P., et al. (2004). *Migration case study: Transport of radionuclides in a reducing clay sediment (TRANCOM-II)*. Office for Official Publications of the European Communities.

[Marschall et al., 2005] Marschall, P., Horseman, S., and Gimmi, T. (2005). Characterisation of gas transport properties of the opalinus clay, a potential host rock formation for radioactive waste disposal. *Oil & gas science and technology*, 60(1):121–139.

[Matheron, 1975] Matheron, G. (1975). *Random sets and integral geometry*. John Wiley & Sons.

[Nagra, 2002] Nagra (2002). Projekt opalinuston: Synthese der geowissenschaftlichen untersuchungsergebnisse. Technical Report NTB 02-03, Nagra, Wettingen, Switzerland.

[Nur and Byerlee, 1971] Nur, A. and Byerlee, J. (1971). An exact effective stress law for elastic deformation of rock with fluids. *Journal of Geophysical Research*, 76(26):6414–6419.

[Pearson et al., 2003] Pearson, F., Arcos, D., Bath, A., Boisson, J., Fernández, A. M., Gäbler, H., Gaucher, E., Gautschi, A., Griffault, L., Hernán, P., et al. (2003). *Mont Terri project: Geochemistry of water in the Opalinus clay formation at the Mont Terri Rock Laboratory*, volume 5. Office fédéral des eaux et de la géologie OFEG.

[Pusch and Forsberg, 1983] Pusch, R. and Forsberg, T. (1983). *Gas migration through bentonite clay*. Svensk Kärnbränsleförsörjning AB.

[Pusch et al., 1985] Pusch, R., Ranhagen, L., Nilsson, K., and Geological, S. (1985). Gas migration through mx-80 bentonite. final report. Technical report, NAGRA Technical Report 85-36.

[Ranaivomanana et al., 2011] Ranaivomanana, H., Verdier, J., Sellier, A., and Bourbon, X. (2011). Toward a better comprehension and modeling of hysteresis cycles in the water sorption–desorption process for cement based materials. *Cement and Concrete Research*, 41(8):817–827.

[Robin, 1973] Robin, P.-Y. F. (1973). Note on effective pressure. *Journal of Geophysical Research*, 78(14):2434–2437.

[Robinet, 2008] Robinet, J.-C. (2008). *Minéralogie, porosité et diffusion des solutés dans l'argilite du Callovo-Oxfordien de Bure (Meuse, Haute-Marne, France) de l'échelle centimétrique à micrométrique*. PhD thesis, Université de Poitiers.

[Robinet et al., 2012a] Robinet, J.-C., Sardini, P., Coelho, D., Parneix, J.-C., Prêt, D., Sammartino, S., Boller, E., and Altmann, S. (2012a). Effects of mineral distribution at mesoscopic scale on solute diffusion in a clay-rich rock: Example of the callovo-oxfordian mudstone (bure, france). *Water Resources Research*, 48(5).

[Robinet et al., 2012b] Robinet, J.-C., Yven, B., Coelho, D., and Talandier, J. (2012b). Les distributions de tailles de pores dans les argilites du callovo-oxfordien de lest de la france. In *Transfert 2012 French Conference on the Transport Properties of Geomaterials (In French)*, pages 263–272. Ecole Centrale de Lille, France.

[Ronse, 2008] Ronse, C. (2008). Reconstructing masks from markers in non-distributive lattices. *Applicable Algebra in Engineering, Communication and Computing*, 19(1):51–85.

[Roubin, 2013] Roubin, E. (2013). *Meso-scale FE and morphological modeling of heterogeneous media: applications to cementitious materials*. PhD thesis, École normale supérieure de Cachan-ENS Cachan.

[Roubin et al., 2015] Roubin, E., Colliat, J.-B., and Benkemoun, N. (2015). Meso-scale modeling of concrete: A morphological description based on excursion sets of random fields. *Computational Materials Science*, 102:183–195.

[Sander, 1999] Sander, R. (1999). Compilation of henry's law constants for inorganic and organic species of potential importance in environmental chemistry.

[Sander, 2015] Sander, R. (2015). Compilation of henry's law constants (version 4.0) for water as solvent. *Atmospheric Chemistry & Physics*, 15(8).

[Schowalter, 1979] Schowalter, T. T. (1979). Mechanics of secondary hydrocarbon migration and entrapment. *AAPG bulletin*, 63(5):723–760.

[Serra, 1982] Serra, J. (1982). *Image analysis and mathematical morphology, v. 1.* Academic press.

[Serra, 1988] Serra, J. (1988). *Image analysis and mathematical morphology, v. 2: Theoretical Advances.* Academic press.

[Skempton, 1984] Skempton, A. (1984). Effective stress in soils, concrete and rocks. *Selected papers on soil mechanics*, pages 106–118.

[Soille, 2013] Soille, P. (2013). *Morphological image analysis: principles and applications.* Springer Science & Business Media.

[Song et al., 2015] Song, Y., Davy, C. A., Troadec, D., Blanchenet, A.-M., Skoczylas, F., Talandier, J., and Robinet, J.-C. (2015). Multi-scale pore structure of cox claystone: Towards the prediction of fluid transport. *Marine and Petroleum Geology*, 65:63–82.

[Su, 2005] Su, K. (2005). *Contribution à l'étude du comportement mécanique et thermo-hydro-mécanique des argilites du Callovo-Oxfordien: application au stockage des déchets radioactifs.* PhD thesis, Université de Lille.

[Taylor et al., 2009] Taylor, J. E., Adler, R. J., et al. (2009). Gaussian processes, kinematic formulae and poincaré's limit. *The Annals of Probability*, 37(4):1459–1482.

[Terzaghi, 1923] Terzaghi, K. v. (1923). Die berechnung der durchlassigkeitsziffer des tones aus dem verlauf der hydrodynamischen spannungserscheinungen. *Sitzungsberichte der Akademie der Wissenschaften in Wien, Mathematisch-Naturwissenschaftliche Klasse, Abteilung IIa*, 132:125–138.

[Thomas et al., 1968] Thomas, L., Katz, D., Tek, M., et al. (1968). Threshold pressure phenomena in porous media. *Society of Petroleum Engineers Journal*, 8(02):174–184.

[Van Geet et al., 2008] Van Geet, M., Bastiaens, W., and Ortiz, L. (2008). Self-sealing capacity of argillaceous rocks: Review of laboratory results obtained from the selfrac project. *Physics and Chemistry of the Earth, Parts A/B/C*, 33:S396–S406.

[Vargaftik et al., 1983] Vargaftik, N., Volkov, B., and Voljak, L. (1983). International tables of the surface tension of water. *Journal of Physical and Chemical Reference Data*, 12(3):817–820.

[Varloteaux et al., 2013] Varloteaux, C., Békri, S., and Adler, P. M. (2013). Pore network modelling to determine the transport properties in presence of a reactive fluid: From pore to reservoir scale. *Advances in Water Resources*, 53:87–100.

[Vincent, 1993] Vincent, L. (1993). Morphological grayscale reconstruction in image analysis: applications and efficient algorithms. *Image Processing, IEEE Transactions on*, 2(2):176–201.

[Wemaere et al., 2008] Wemaere, I., Marivoet, J., and Labat, S. (2008). Hydraulic conductivity variability of the boom clay in north-east belgium based on four core drilled boreholes. *Physics and Chemistry of the Earth, Parts A/B/C*, 33:S24–S36.

[Wu, 2014] Wu, Q. (2014). *Isothermes de désorption de matériaux cimentaires: étude d'un protocole accéléré et estimation du VER*. PhD thesis, Lille 1.

[Xu et al., 1997] Xu, K., Daian, J.-f., and Quenard, D. (1997). Multiscale structures to describe porous media part i: theoretical background and invasion by fluids. *Transport in porous media*, 26(1):51–73.

[Yang, 2008] Yang, D. (2008). *Caractérisation par la mesure de perméabilité au gaz de l'endommagement mécanique et hydrique dans l'EDZ des argilites du Callovo-Oxfordien*. PhD thesis, École Nationale Supérieure des Mines de Paris.

[Yang and Aplin, 1998] Yang, Y. and Aplin, A. C. (1998). Influence of lithology and compaction on the pore size distribution and modelled permeability of some mudstones from the norwegian margin. *Marine and Petroleum Geology*, 15(2):163–175.

[Yuan and Lee, 2013] Yuan, Y. and Lee, T. R. (2013). Contact angle and wetting properties. In *Surface science techniques*, pages 3–34. Springer.

[Yven et al., 2007] Yven, B., Sammartino, S., Géraud, Y., Homand, F., and Villiéras, F. (2007). Mineralogy, texture and porosity of callovo-oxfordian argillites of the meuse/haute-marne region (eastern paris basin). *Mémoires de la Société géologique de France*, 178:73–90.

[Zoback and Byerlee, 1975] Zoback, M. D. and Byerlee, J. (1975). Permeability and effective stress: geologic notes. *AAPG Bulletin*, 59(1):154–158.